공학박사 학위논문

Multi-scale finite element modeling with mean-field homogenization for predicting mechanical and fracture behavior of cast aluminum alloy

평균장 균질화법 및 다중스케일 유한요소 모델을 활용한 알루미늄 주조합금의 기계적 물성 및 파괴거동 예측

2021 년 8 월

서울대학교 대학원

재료공학부

정 우 진

Multi-scale finite element modeling with mean-field homogenization for predicting mechanical and fracture behavior of cast aluminum alloy

평균장 균질화법 및 다중스케일 유한요소 모델을 활용한 알루미늄 주조합금의 기계적 물성 및 파괴거동 예측

지도 교수 이 명 규

이 논문을 공학박사 학위논문으로 제출함
2021 년 7 월

서울대학교 대학원
재료공학부
정 우 진

정우진의 공학박사 학위논문을 인준함
2021 년 7 월

위 원 장 한 흥 남

부위원장 이 명 규

위 원 유 웅 열

위 원 홍 승 현

위 원 봉 혁 종

Abstract

Cast Al alloys are commonly used in the aerospace and automobile industries because of their excellent properties such as weldability, corrosion resistance, wear-resistance, and lightweight. Herein, Si, Mg, and Mn were added to the A365.0-T6 alloy, and the resulting material was characterized. Si was added to increase castability, and magnesium and manganese are the main added elements. The microstructure and mechanical properties of the material are determined via the T6 heat treatment process, which undergoes artificial aging after the solution heat treatment. Cast Al alloys comprise the Al matrix, silicon particles, intermetallic compounds, and Mg_2Si precipitates. Besides, void defects are observed because of the entrained air during casting.

Cast Al alloys exhibit a large spread of fracture strain because of the large pores in the material. In the absence of pores, voids are formed due to the cracking of Si particles, which are inclusions, and the strain is concentrated between the cracked Si particles, causing material damage. In addition, in ductile metallic materials, failure is explained by the nucleation, growth, and coalescence of voids; thus, microvoids also affect the material's mechanical properties. Therefore, the Al matrix, Si particles, and voids among the microstructure of the cast Al alloy are the main factors affecting the mechanical and fracture behavior of the material. Herein, the mechanical behavior and fracture scatter of cast Al alloys were described by multiscale modeling based on the material properties of microstructures. Performing the finite element analysis by dispersing the microstructures, similar to the

distribution of real substances, was inefficient; therefore, the Mori–Tanaka (MT) mean-field method was introduced as an alternate. The MT mean-field approach can derive the homogenized mechanical behavior of a material comprising two phases based on several assumptions and Eshelby's equation. Compared with calculating the average behavior of multiple phases using the representative volume element, the calculation is more efficient and can easily apply microstructures of various distributions. Assuming that the microvoids belong to the Al matrix, the cast Al alloy can be considered as a material comprising two phases of an Al matrix and Si particles, so that MT can be applied. The stress and strain of the Al matrix and Si particles were also calculated while calculating the homogenized mechanical response using MT. Because the Al matrix was assumed to contain microvoids, the mechanical behavior was computed by applying the Gurson–Tvergaard–Needleman (GTN) model, which is a damage-coupled model that describes the damage caused by the growth and coalescence of voids. Because the Si particles deform only elastically, the stress was calculated using the generalized Hooke's law. The Weibull distribution function was used to determine whether the Si particles were cracked, and the nucleated voids by the cracks in the Si particles were added to the Al matrix and modeled to be applied while calculating the material damage using the GTN model.

Tensile tests were performed using different shapes of specimens to measure the mechanical and fracture behavior of the cast Al alloys under different stress triaxialities. The material's microstructure before deformation was observed to obtain the microstructural distribution information of the material required for

the microstructure-based model. The distribution of microstructures was statistically analyzed using X-ray tomography, optical microscopy, and scanning electron microscopy, and based on these analyses, it was applied to computational simulations according to probability. The feasibility of the method proposed in this paper was verified by observing the microstructural changes after deformation.

The results predicted using the proposed microstructure-based model were in good agreement with the experimental results of the mechanical and fracture behavior of cast Al alloys. The effect of the distribution and size of voids on the material's fracture was analyzed. In particular, we confirmed that the macrovoids considerably affect the fracture of the material. The proposed model can explain the material's damage evolution process starting from the cracking of the Si particles and the specimen fractures off-center.

Keyword : Cast Al alloy, microstructure-based fracture model, Mori–Tanaka mean-field method, Gurson–Tvergaard–Needleman model

Student Number : 2019-38965

Contents

List of tables

List of figures

1. Introduction

1.1. Cast Al alloy

Al–Si–Mg cast alloys, herein A365.0-T6, are used in aerospace and automotive industries. Material properties of cast aluminum alloys are light weight, high corrosion resistivity, good weldability, and castability. In the automobile industry, which aims to increase fuel efficiency by reducing weight, there is a movement to increase the use of aluminum castings that have excellent material properties as lightweight metals. Thus, it is necessary to understand their mechanical behavior properly to ensure their appropriate use as a structural material.

A365.0-T6 is composed of eutectic Si particles, intermetallic compounds, Mg_2Si precipitates, and an Al matrix. As shown in Figure 1-1(a), voids are observed due to air inflow during casting. In the cast Al alloy, the eutectic zone is formed [Figure 1-1(b)], which is the enlarged box of Figure 1-1(a). As shown in Figure 1-1(b), (c), and (d) are Si particle, intermetallic compound, and Al matrix, respectively. Mg_2Si precipitate is of the submicron size, so it is not observed in the optical micrographs. The eutectic Si particle is the most commonly observed particle in A365-T6 because of the high Si content. Table 1-1 presents the chemical composition of A365.0-T6. The main chemical components of the 3xx.x series cast Al alloys are Si and Mg. Si mainly influences the castability, and Mg strengthens the alloy by forming Mg_2Si precipitates. Mn in cast Al alloys improves ductility by forming an

intermetallic compound, $Al_{12}(Fe,Mn)_3Si$, rather than needle-like and plate-like secondary phase, such as $Al_9Fe_2Si_2$, which can cause brittleness [1].

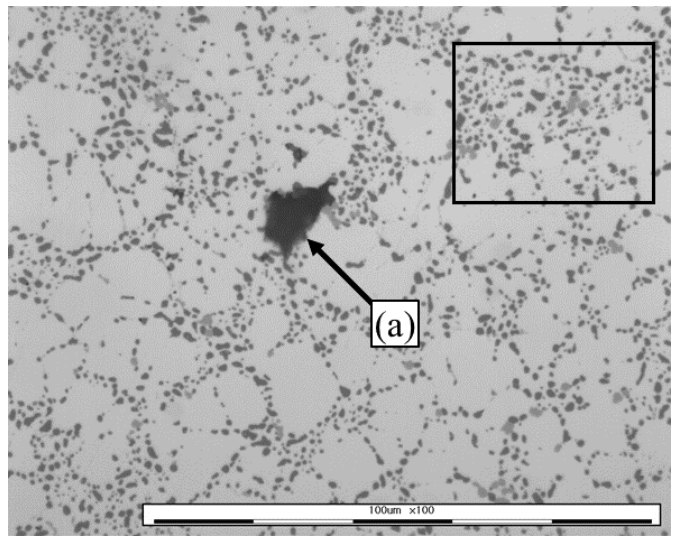

(a)

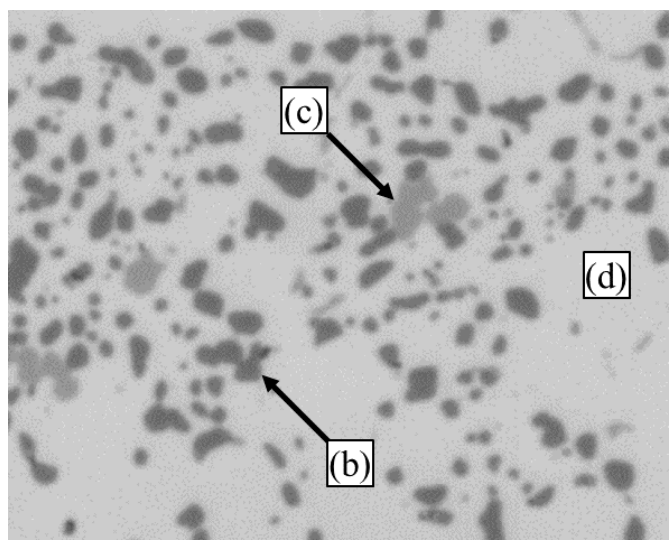

(b)

Figure 1-1. Optical microscope images of cast Al alloy. (b) Magnified image from box in (a). (a) in (a) is void. (b), (c), and (d) in (b) are Si particle, intermetallic compound, and Al matrix, respectively.

The T6 temper cycle applied to the material begins with a solution heat treatment at 490°C for 0.5 h, followed by air cooling at room temperature, and artificial aging at 200°C for 2 h. The solution heat treatment improves the alloy's ductility by dissolving the intermetallic phase and inducing the spheroidization of eutectic Si [2]. Artificial aging is involved in the formation of Mg_2Si and affects the material's strength and hardness [1].

Table 1-1. Chemical composition of A365.0-T6 (wt%).

Al	Si	Mn	Mg	Fe	Cu	Zn	Ti	Sr
Bal.	11.4	0.67	0.34	0.14	0.016	0.011	0.092	0.013

1.2. Mechanical properties of cast Al alloy

Large scattering of fracture displacements or strains is observed in the mechanical testing of cast Al alloys. Mae *et al.* [3] and Teng *et al.* [4,5] analyzed the correlation between large pores (macrovoids) and fracture scattering through several studies. They performed more than 30 repeated tensile tests to show the spread of the fracture strain and proposed a probabilistic fracture criterion based on the phenomenological fracture criterion proposed by Bao and Wierzbicky [6]. Besides, Francis and Cantin [7], Lee *et al.* [8], Liu *et al.* [9], and Lordan *et al.* [10] reached similar conclusions.

According to Wang *et al.*, the damage evolution of Al–Si–Mg alloys begins

with the crack of the Si particles in the absence of voids. During material deformation, when the material's internal stress reaches a critical value, the Si particles crack, and the strain between the cracks is concentrated to form a shear band, eventually cracking [11,12]. However, the interface separation between the Si particles and the Al matrix was not observed in their works.

Mueller *et al.* measured the strength of the Si particles using a microbending test and simulation. Si particles undergo elastic deformation until cracking occurs, and their strength ranges from 6–12 GPa. Besides, their strength decreases in the presence of defects [13]. Materials like Al–Si–Mg alloys, in which brittle particles are dispersed in a ductile metal matrix, are called metal matrix composites (MMCs).

1.3. Fracture approaches of cast Al alloy

The pores that are unavoidably formed during the casting process are unevenly distributed in the material. Voids are important in explaining the evolution of the damage of the material. Here, appropriate methodologies should be used to account for the relationship between the matrix, particulates, and voids to describe the material's mechanical behavior. It can be classified as a material in which voids are distributed in an effective medium composed of matrix and particles, or a material in which particles are distributed in an effective medium composed of matrix and voids. The former, which is the void-embedded material, could be effectively described using the Gurson-Tvergaard-Needleman (GTN) model. The GTN model was built by Gurson [14], Chu and Needleman [15], Tvergaard [16], and Tvergaard and Needleman

[17] by considering the void nucleation, growth, and coalescence. The representative volume element (RVE) with periodic boundary conditions and the mean-field method are widely used approaches for the latter case.

Horstemeyer *et al.* [18] used the McClintocks void growth model [19] and the Bammann–Chiesa–Johnson plasticity model [20] to describe the mechanical behavior and damage evolution of Al–Si–Mg alloys under different stress states. Statistically analyzed void nucleation data caused by cracking of Si particles and the decohesion between the Al matrix and Si particles were applied to describe the damage evolution of cast Al alloys [18]. The modeling was focused only on the nucleation and growth of voids, like the GTN model represented by the former case. They were unconcerned about the mechanical behavior variation caused by the interaction between the microstructures. Baral *et al.* [21] predicted the failure of die-cast Al–Si–Mg alloys using the widely used fracture criteria proposed by Oyane [22], Johnson-Cook [23], and Hosford-Coulomb [24], along with Yld2004-3D [25], which accounts for the plastic behavior of anisotropic materials. Their study did not focus on the microstructural changes and the fracture strain scattering.

Fagerholt *et al.* [26] used Cockcroft-Latham [27] fracture initiation criterion with parameters modified by the weakest-link Weibull distribution for describing large variations in the tensile ductility of cast Al alloys. They were also unconcerned about the role of microstructures.

1.4. Homogenization method of multiphase materials

The unit cell with reinforcement particles is suitable for specifically observing

the behavior of each phase according to the boundary conditions on the MMC using finite element analysis (FEA) [28–30]. Ghosh *et al.* proposed a multi-scale approach for homogenizing an MMC with a two-dimensional (2D) Voronoi cell, called VCFEM. The calculation of each integration point of the FEA was linked with 2D Voronoi cells of various morphologies, which have nonuniformly distributed particles. Additionally, the Weibull-type crack criterion was applied for the cracking of particles. However, due to the high computational cost, the number of morphologies was limited [31–34]. Ghosh *et al.* further improved the VCFEM for computational efficiency. The mean values of the mechanical response of the 2D RVE were reproduced with a homogenization-based continuous plasticity damage (HCPD) model [35]. The HCPD model would be useful when the fractions of voids and particles are uniform throughout the material. If there are variations in the fraction of voids and particles in the material, it becomes difficult to apply the HCPD model.

It is known that the 3D RVE is more suitable for describing the behavior of MMCs than the 2D RVE [36,37]. Böhm *et al.* showed that the mechanical behavior obtained using the 3D RVE and that obtained through the mean-field method agreed excellently. The Weibull distribution, which statistically describes the cracks of brittle particles, was used to simulate the crack of the reinforcement particles in the RVE simulation. The RVE simulation was performed severally, and it was shown that the crack tendency of the particles appeared differently in each trial. The decrease in strength due to particle cracking was also described [38]. There is a limit to the application of

microstructure diversity, such as when the particle distribution is different in the same fraction and shape.

Contrary to the hierarchy FEM model for MMCs, the Mori–Tanaka mean-field method (MT) has the advantage of applying different volume fraction microstructures on a statistical basis to each material point at a relatively low computational cost [39,40]. Delannay *et al.* used the incremental MT approach, which Doghri and Ouaar proposed, to model the phase transformation of TRIP steel in loading and predicted the behavior of multiphase steel in tension–compression cycles [41–43]. Simar *et al.* analyzed the strength of interfacial debonding between the matrix and the particles using the MT method for friction stir-processed Mg-C composites [44]. Rutecka *et al.* used the MT method to describe the damage evolution of AA2124/SiC MMC based on the elastic modulus degradation during loading–unloading test [45].

1.5. Research objectives

Herein, we develop a microstructure-based ductile fracture model, in which the mechanical properties and fracture mechanism are formulated based on the mean-field method and probabilistic failure analysis. For the mean-field method, the well-known MT method is used, which results in the homogenized mechanical behavior of Al alloys, including the stress on the Si particles embedded in the aluminum matrix. The GTN model is used to describe the ductile fracture of the Al matrix, coupled with the Weibull distribution function.

2. Microstructure-based fracture model

2.1. Mori–Tanaka mean-field method

The Mori–Tanaka mean-field method (MT method) was employed for homogenizing the mechanical responses of the Si-added Al alloy, where the Si particles are embedded in the eutectic zone of the investigated Al alloy. The MT method has been employed for calculating the homogenized mechanical behavior of metal matrix composites (MMC) based on the elastoplastic properties of each constituent phase. In this method, the well-known Eshelby's equations are solved, which results in the strain and stress of each phase [46]. Note that there are alternative approaches for homogenizing multiphase or inhomogeneous materials, such as the classical Voigt or Reuss method and Hill's self-consistent method [47].

Herein, approximations are applied in the MT method to simplify the solution procedure. First, Si particles are assumed to deform only elastically. Mueller *et al.* [13] observed the fully elastic unloading behavior of Si particles during a microbending test. Second, the Si particles are homogeneously distributed in the Al matrix and do not interact with each other. The Si particles in the investigated Al–Si–Mg alloys have various sizes and aspect ratios. According to a prior study related to the Weibull statistics, it was reported that the cracking of Si particles depended on the sizes and dimensions of the Si particles [48–50]. However, to implement a simplified simulation, the Si particles are assumed to have the same spherical shape with different sizes, and do not change shape during loading. Finally, the nucleation of the void

corresponds to the cracked Si particle, which will be used for the Gurson-Tvergaard-Needleman (GTN) model.

2.1.1. Mean-field homogenization

The material properties of each phase must be considered to describe the behavior of multiphase materials, such as MMC. It is impractical and inefficient to calculate the material's behavior by shaping the material's microstructure exactly as it is in reality, so another method is needed. It is an efficient method to consider each material point in the computational analysis as an representative volume element (RVE). There are two ways to compute the homogenized response of RVE at a material point. One way is to link the material point and the RVE. Another way is to express an imaginary RVE with assumptions and formulas. Based on the former, the calculated homogenized response of the material is highly accurate, but has the following limitations. The shape of the phase distribution of the RVE is inevitably uniform and computationally expensive. However, the homogenized response using an assumption-based equation, such as the mean-field method, is free from these limitations.

The homogenized mechanical behavior calculated at the material point of the multiphase material simulation must satisfy the following Hill-Mandel condition

$$\bar{\boldsymbol{\sigma}} : \bar{\boldsymbol{\varepsilon}} = \langle \boldsymbol{\sigma} \rangle_{\omega} : \langle \boldsymbol{\varepsilon} \rangle_{\omega} = \langle \boldsymbol{\sigma} : \boldsymbol{\varepsilon} \rangle_{\omega} \tag{2.1}$$

This means that the average volume of the mechanical work must be equivalent regardless of the calculation scale. Here $\langle\ \rangle_{\omega}$ denotes a volume-

averaged variable in the domain of RVE, ω, and can be expressed as follows.

$$\langle \boldsymbol{\sigma} \rangle_{\omega_k} = \frac{1}{V} \int_{\omega_k} \boldsymbol{\sigma} dV = \bar{\boldsymbol{\sigma}}_{\omega_k} \tag{2.2}$$

$$\omega = \sum_k \omega_k \tag{2.3}$$

Where ω_k is the domain of the *k-th* phase. In the imaginary RVE, compatibility and equilibrium must be satisfied, and the corresponding relationship is given as follows.

$$\bar{\boldsymbol{\sigma}} = \sum_k v_k \bar{\boldsymbol{\sigma}}_{\omega_k}, \quad \bar{\boldsymbol{\varepsilon}} = \sum_k v_k \bar{\boldsymbol{\varepsilon}}_{\omega_k} \tag{2.4}$$

where v_k is the volume fraction of the k-th phase.

The stress and strain of each phase can be calculated using concentration factor tensors as follows:

$$\bar{\boldsymbol{\varepsilon}}_{\omega_k} = \mathbf{A}_k : \bar{\boldsymbol{\varepsilon}} \tag{2.5}$$

$$\bar{\boldsymbol{\sigma}}_{\omega_k} = \mathbf{B}_k : \bar{\boldsymbol{\sigma}} \tag{2.6}$$

where $\mathbf{A}_k$ and $\mathbf{B}_k$ are the strain and stress concentration factor tensors of the *k-th* phase, respectively. The fundamental properties of the concentration factor tensors are introduced as follows.

$$\sum_k v_k \mathbf{A}_k = \mathbf{I} \tag{2.7}$$

$$\sum_k v_k \mathbf{B}_k = \mathbf{I} \tag{2.8}$$

The stiffness tensor of the homogenized RVE can be calculated from the following equation.

$$\mathbf{C} = \sum_k v_k \mathbf{C}_k : \mathbf{A}_k \tag{2.9}$$

2.1.2. Homogenization method

The Voigt and Reuss methods are the easiest approaches to estimate the homogenized mechanical behavior of a multiphase material. The Voigt method assumes the equivalent strain is applied to all phases of the RVE. That is, $\mathbf{A}_k = \mathbf{I}$. In contrast, the equivalent stress of all phases is assumed in the Reuss method, $\mathbf{B}_k = \mathbf{I}$. It is difficult to expect accuracy in these methods.

Eshelby's solution for calculating the stress of the ellipsoid inclusion embedded in the matrix triggered the emergence of sophisticated homogenization approaches [46]. Hill and Budiansky developed a self-consistent method considering the interaction between the grain and the matrix for a polycrystalline material [47,51].

The study by Tanaka and Mori for explaining hardening behavior with strong inclusion-provided clues to a simpler homogenization approach for two-phase materials [40]. They introduced Eshelby's equivalent inclusion theory to calculate the internal stress field caused by non-deforming particles. Bate *et al.* [52] promoted the elastic inclusion model by adding simple assumptions based on the work of Tanaka and Mori. Barlat and Liu [53] further developed this model to propose a kinematic hardening model for a binary alloy containing elastic particles. This model can show the Bauschinger material effect by applying the back stress effect due to strong inclusions. These can be considered simple homogenization models.

Mori and Tanaka applied the idea of average stress in their previous work. In

the process, the prototype of the well-known MT model was created [39]. Weng [54], Benveniste [55], and Lagoudas *et al.* [56] reformulated the Mori–Tanaka model to calculate the effective properties of composite materials. The theory reconstructed with the concentrated factor tensor is explained in the next subsection.

2.1.3. Mori–Tanaka mean-field method

When the boundary condition of an MMC is prescribed to correspond to the average strain $\bar{\boldsymbol{\varepsilon}}$, the average perturbed strain of the matrix due to the embedded particles and the perturbed strain of the particles are $\tilde{\boldsymbol{\varepsilon}}$ and $\boldsymbol{\varepsilon}^{pt}$, respectively. In this situation, the stress of inclusion in the matrix can be expressed as follows based on Eshelby's equivalent inclusion principle [46].

$$\boldsymbol{\sigma}_1 = \mathbf{C}_1 : \left(\bar{\boldsymbol{\varepsilon}} + \tilde{\boldsymbol{\varepsilon}} + \boldsymbol{\varepsilon}^{pt}\right) = \mathbf{C}_0 : \left(\bar{\boldsymbol{\varepsilon}} + \tilde{\boldsymbol{\varepsilon}} + \boldsymbol{\varepsilon}^{pt} - \boldsymbol{\varepsilon}^{*}\right) \tag{2.10}$$

$\boldsymbol{\sigma}_1$ is the stress of inclusion, $\mathbf{C}_0$ and $\mathbf{C}_1$ are the elastic stiffness values of the matrix and inclusion, respectively, and $\boldsymbol{\varepsilon}^{*}$ is the strain introduced to compensate for the $\boldsymbol{\varepsilon}^{pt}$ effect. The relationship between the strains can be written as follows.

$$\boldsymbol{\varepsilon}^{pt} = \mathbf{S}\boldsymbol{\varepsilon}^{*} \tag{2.11}$$

Where $\mathbf{S}$ is the Eshelby tensor and $\boldsymbol{\varepsilon}^{*}$ is the particle strain in the absence of stress, known as the transformation strain or eigenstrain. The inclusion and matrix strains can be rewritten as

$$\bar{\boldsymbol{\varepsilon}}_1 = \bar{\boldsymbol{\varepsilon}} + \tilde{\boldsymbol{\varepsilon}} + \boldsymbol{\varepsilon}^{pt} \tag{2.12}$$

$$\bar{\boldsymbol{\varepsilon}}_0 = \bar{\boldsymbol{\varepsilon}} + \tilde{\boldsymbol{\varepsilon}} \tag{2.13}$$

Using Equation (2.4), the perturbed strain can be expressed

$$\tilde{\boldsymbol{\varepsilon}} = -v_1 \boldsymbol{\varepsilon}^{pt} = -v_1 \mathbf{S} : \boldsymbol{\varepsilon}^* \tag{2.14}$$

From Equations (2.10), (2.12), and (2.13),

$$\mathbf{C}_1 : \bar{\boldsymbol{\varepsilon}}_1 = \mathbf{C}_0 : \left(\bar{\boldsymbol{\varepsilon}}_1 - \boldsymbol{\varepsilon}^* \right)$$

$$\boldsymbol{\varepsilon}^* = \mathbf{C}_0^{-1} : \left(\mathbf{C}_0 - \mathbf{C}_1 \right) : \bar{\boldsymbol{\varepsilon}}_1 \tag{2.15}$$

Equation (2.12) can be expressed as

$$\bar{\boldsymbol{\varepsilon}}_1 = \bar{\boldsymbol{\varepsilon}} + v_0 \mathbf{S} : \boldsymbol{\varepsilon}^* \tag{2.16}$$

Substituting (2.15) into (2.16)

$$\bar{\boldsymbol{\varepsilon}} = \left[\mathbf{I} - v_0 \mathbf{S} : \mathbf{C}_0^{-1} : \left(\mathbf{C}_0 - \mathbf{C}_1 \right) \right] \bar{\boldsymbol{\varepsilon}}_1 \tag{2.17}$$

Then, the strain concentration factor tensor for the particle phase is given as

$$\mathbf{A}_1^{-1} = \left[\mathbf{I} - v_0 \mathbf{S} : \mathbf{C}_0^{-1} : \left(\mathbf{C}_0 - \mathbf{C}_1 \right) \right] \tag{2.18}$$

Another way to compute the strain concentration factor tensor is similar to the above. From Equations (2.12) and (2.13)

$$\bar{\boldsymbol{\varepsilon}}_1 = \bar{\boldsymbol{\varepsilon}}_0 + \boldsymbol{\varepsilon}^{pt} = \bar{\boldsymbol{\varepsilon}}_0 + \mathbf{S} : \boldsymbol{\varepsilon}^* \tag{2.19}$$

Substituting (2.17) into (2.19),

$$\bar{\boldsymbol{\varepsilon}}_1 = \bar{\boldsymbol{\varepsilon}}_0 + \mathbf{S} : \left[\mathbf{C}_0^{-1} : \left(\mathbf{C}_0 - \mathbf{C}_1 \right) : \bar{\boldsymbol{\varepsilon}}_1 \right] \tag{2.20}$$

$$\left[\mathbf{I} - \mathbf{S} : \left(\mathbf{I} - \mathbf{C}_0^{-1} : \mathbf{C}_1 \right) \right] : \boldsymbol{\varepsilon}_1 = \mathbf{H}^{-1} : \boldsymbol{\varepsilon}_1 = \boldsymbol{\varepsilon}_0 \tag{2.21}$$

where $\mathbf{H}$ is a tensor which describes the relationship between the phases.

From (2.4)

$$v_1 \bar{\boldsymbol{\varepsilon}}_1 + \left(1 - v_1 \right) \bar{\boldsymbol{\varepsilon}}_0 = \mathbf{A}_1^{-1} : \bar{\boldsymbol{\varepsilon}}_1 \tag{2.22}$$

$$v_1 \mathbf{H} : \bar{\boldsymbol{\varepsilon}}_0 + \left(1 - v_1 \right) \bar{\boldsymbol{\varepsilon}}_0 = \mathbf{A}_1^{-1} : \mathbf{H} : \bar{\boldsymbol{\varepsilon}}_0$$

$$\mathbf{A}_1 = \mathbf{H} : \left(v_1 \mathbf{H} + v_0 \mathbf{I} \right)^{-1} = \left(v_1 \mathbf{I} + v_0 \mathbf{H}^{-1} \right) \tag{2.23}$$

Also, from (2.4)

$$\bar{\boldsymbol{\varepsilon}} = v_1 \mathbf{H} : \bar{\boldsymbol{\varepsilon}}_0 + v_0 \bar{\boldsymbol{\varepsilon}}_0$$

$$\mathbf{A}_0 = \left(v_1\mathbf{H} + v_0\mathbf{I}\right)^{-1} \tag{2.24}$$

The tangent modulus for the homogenized response can be calculated as follows.

$$\begin{aligned}\mathbf{C} &= v_1\mathbf{C}_1 : \mathbf{H} : \left(v_1\mathbf{H} + v_0\mathbf{I}\right)^{-1} + v_0\mathbf{C}_0 : \left(v_1\mathbf{H} + v_0\mathbf{I}\right)^{-1} \\ &= \left[v_1\mathbf{C}_1 : \mathbf{H} + v_0\mathbf{C}_0\right] : \left[v_1\mathbf{H} + v_0\mathbf{I}\right]^{-1}\end{aligned} \tag{2.25}$$

From Equation (2.7), $\mathbf{A}_0$ can be expressed as follows.

$$\mathbf{A}_0 = \frac{1}{v_0}\left(\mathbf{I} - v_1\mathbf{A}_1\right)$$

Then another form of the tangent modulus of the MMC is

$$\mathbf{C} = v_1\mathbf{C}_1 : \mathrm{A}_1 + \mathbf{C}_0 : \left(\mathbf{I} - v_1\mathbf{A}_1\right) = \mathbf{C}_0 + v_1\left(\mathbf{C}_1 - \mathbf{C}_0\right) : \mathbf{A}_1 \tag{2.26}$$

2.1.4. Implementation of Mori–Tanaka mean-field method

An excellent strategy for implementing the MT homogenization method has been suggested by Doghri and Ouaar [41]. Perdahcıoğlu and Geijselaers [57] also briefly suggested the method. Referring to the methods of Doghri and Ouaar [41] and Perdahcıoğlu and Geijselaers [57], the process of calculating the homogenized reaction of an MMC is summarized as follows. The calculation flow is schematically shown in Figure 2-1.

The prescribed strain at the material point is distributed to each phase through the following equations.

From Equations (2.4) and (2.5)

$$\Delta\overline{\boldsymbol{\varepsilon}}_1 = \mathbf{A}_1\Delta\overline{\boldsymbol{\varepsilon}} \tag{2.27}$$

$$\Delta\overline{\boldsymbol{\varepsilon}}_0 = \frac{\Delta\overline{\boldsymbol{\varepsilon}} - v_1\Delta\overline{\boldsymbol{\varepsilon}}_1}{1 - v_1}$$

The initial value of the strain concentration factor tensor $\mathbf{A}_1$ is assumed as the fourth-order identity tensor $\mathbf{I}$.

The elastoplastic behavior and the consistent tangent modulus $\mathbf{C}_0$ of the matrix phase can be calculated using a given strain increment $\Delta\bar{\boldsymbol{\varepsilon}}_0$. Then, the Eshelby tensor is needed to compute the strain concentration factor tensor. Doghri and Ouaar empirically pointed out that the prediction accuracy was improved when obtaining the Eshelby tensor $\mathbf{S}$ using the isotropic consistent tangent modulus $\mathbf{C}_0^{iso}$ of the matrix phase. They calculated $\mathbf{C}_0^{iso}$ using the following equation proposed by Bornet *et al.* [41,58].

$$\mathbf{C}_0^{iso} = \left(\mathbf{I}^{vol} :: \mathbf{C}_0\right)\mathbf{I}^{vol} + \frac{1}{5}\left(\mathbf{I}^{dev} :: \mathbf{C}_0\right)\mathbf{I}^{dev} \tag{2.28}$$

Two double dot operator means a scalar product between the two fourth-order tensors as follows.

$$\mathbf{I}^{vol} :: \mathbf{C}_0 = I_{ijkl}^{vol} C_{0,lkji}$$

$\mathbf{I}^{vol}$ and $\mathbf{I}^{dev}$ are defined as

$$\mathbf{I}^{vol} = \frac{1}{3}\mathbf{1} \otimes \mathbf{1}$$

$$\mathbf{I}^{dev} = \mathbf{I} - \mathbf{I}^{vol} \tag{2.29}$$

With $\mathbf{C}_0^{iso}$, $\mathbf{S}$, can be computed based on the work of Mura and that of Gavazzi and Lagourdas [59,60].

The tensors, $\mathbf{A}_1$, $\mathbf{A}_0$, and $\mathbf{H}$, which describe the relationship between the strains of the MMC, the aluminum matrix, and Si particles can be calculated from Equations (2.21), (2.23), (2.24). The following equation is used to determine the appropriateness of the initial condition.

$$\mathbf{R} = \Delta\bar{\boldsymbol{\varepsilon}} - \mathbf{A}_1^{-1}\Delta\bar{\boldsymbol{\varepsilon}}_1 \tag{2.30}$$

If the residual exceeds the tolerance, this procedure is repeated from Equation (2.27), using $\mathbf{A}_1$, which was calculated in the last iteration. After convergence, the stress, strain, and consistent tangent modulus of the MMC are calculated using Equations (2.4) and (2.26).

Christensen *et al.* [61] studied the validity of the MT method according to the inclusion fraction and the stiffness ratio of each phase. Herein, we referred to Christensen's work.

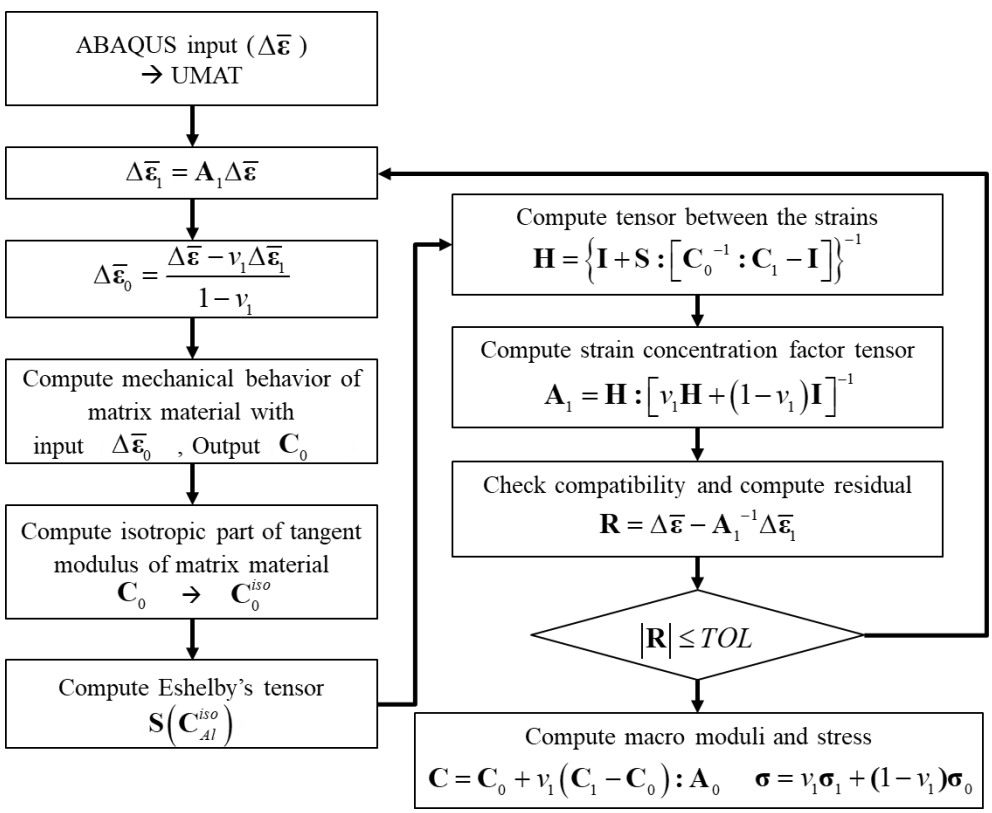

Figure 2-1. Stress-update algorithm of Mori–Tanaka method.

2.2. Modified Gurson–Tvergaard–Needleman model

The GTN model is used for describing the plasticity and ductile failure of the Al matrix. The GTN model has been successfully applied to the failure prediction, where pre-existing or newly nucleated voids in metals are the major origin of the ductile fracture. Herein, the local failure of Si the particle in the Al matrix has been known to be the potential void nucleation cites, which rationales the GTN model implementation.

2.2.1 Gurson–Tvergaard–Needleman model

Several models exist for explaining the ductile failure of polycrystalline metals, including the works by McClintock [19] and Rice and Tracey [62]. They analyzed the void growth in relation to the plastic strain and its role in the ductile fracture [19,62]. Gurson [14] proposed the damage model that couples the ductile failure and the void growth mechanism. Later, Tvergaard and Needleman [17] introduced the void nucleation effect statistically for completing the microvoid-associated ductile fracture of metals; that is, the fracture by void nucleation, growth, and coalescence. In the following, the GNT model is summarized.

The strain rate of the Al matrix with voids can be decomposed additively as follows.

$$\Delta\bar{\boldsymbol{\varepsilon}}_0 = \Delta\bar{\boldsymbol{\varepsilon}}_0^{e} + \Delta\bar{\boldsymbol{\varepsilon}}_0^{p} \tag{2.31}$$

where superscripts *e* and *p* denote the elastic and plastic components. The yield function (or stress potential) of the GTN model is given as follows.

$$\Phi\left(p,q,H_\alpha\right)=\left(\frac{q}{\sigma_Y}\right)^2+2q_1f^*\cosh\left(-\frac{3q_2p}{2\sigma_Y}\right)-\left(1+q_3f^{*2}\right) \tag{2.32}$$

where q is the equivalent stress and p is the hydrostatic stress defined below.

$$p=-\frac{1}{3}\bar{\boldsymbol{\sigma}}_0:\mathbf{1} \tag{2.33}$$

$$q=\sqrt{\frac{3}{2}\left(\mathbf{s}:\mathbf{s}\right)} \tag{2.34}$$

where $\mathbf{s}$ is a deviatoric stress tensor and σ_Y is the flow stress of the Al matrix. The scalar state variable H_α represents an equivalent plastic strain of the Al phase and the void volume fraction, which affects σ_Y and f^* in Equation (2.32). q_1, q_2, and q_3 are material parameters, which are assumed to be 1.5, 1, and 2.25, respectively, according to Tvergaard [63]. The effective void volume fraction f^* can be defined as,

$$f^*=\begin{cases} f, & f<f_c \\ f_c+\left(\dfrac{1}{q_1}-f_c\right)\dfrac{\left(f-f_c\right)}{\left(f_f-f_c\right)}, & f\geq f_c \end{cases} \tag{2.35}$$

where f is one of the scalar state variables, the void volume fraction f_c is the volume fraction for the void coalescence, and f_f is the void volume fraction at the fracture onset. The evolution of the void volume fraction can be described by summing the increase in voids due to nucleation Δf^n and growth Δf^g.

$$\Delta f=\Delta f^n+\Delta f^g \tag{2.36}$$

In the original GTN model, the increment of the void volume fraction by

nucleation has been described by statistical parameters ε_N and S_N, which denote the mean and standard deviation of the void nucleation strain, respectively. Thus, $\Delta f^n = \frac{f_N}{S_N\sqrt{2\pi}}\exp\left[-\frac{1}{2}\left(\frac{\bar{\varepsilon}^p - \varepsilon_N}{S_N}\right)^2\right]\Delta e^p$. Here, f_N is the volume fraction for initiating the void nucleation. However, as mentioned in the previous section, the main void nucleation mechanism is assumed to be caused by Si particle cracking, which will be described by the MT-based analysis. The evolution of the existing void volume fraction can be described as a function of the plastic strain increment of the Al matrix $\Delta\bar{\boldsymbol{\varepsilon}}_0^p$ as follows.

$$\Delta f^g = (1-f)\Delta\bar{\boldsymbol{\varepsilon}}_0^p : \mathbf{1} = (1-f)\Delta\varepsilon_p \tag{2.37}$$

When the flow stress of the Al matrix is prescribed as a function of the plastic strain, e^p,

$$\sigma_Y = \mathrm{f}\left(e^p\right) \tag{2.38}$$

the plastic work equivalence principle results in the following relationship.

$$\bar{\boldsymbol{\sigma}}_0 : \Delta\bar{\boldsymbol{\varepsilon}}_0^p = (1-f)\sigma_Y\Delta e^p \tag{2.39}$$

In the above equation, Δe^p is the equivalent plastic strain increment of the matrix. From the associated flow rule, the plastic strain of the matrix with voids can be defined as follows.

$$\Delta\bar{\boldsymbol{\varepsilon}}_0^p = \Delta\lambda\frac{\partial\Phi}{\partial\bar{\boldsymbol{\sigma}}_0} \tag{2.40}$$

where $\Delta\lambda$ is a positive scalar variable related to the plastic flow. Equation (2.40) can be extended by a chain rule with Equations (2.33) and (2.34). Then,

$$\Delta\bar{\boldsymbol{\varepsilon}}_0^p = \Delta\lambda\left(\frac{\partial\Phi}{\partial q}\mathbf{n} - \frac{1}{3}\frac{\partial\Phi}{\partial p}\mathbf{1}\right) = \Delta\varepsilon_q\mathbf{n} + \frac{1}{3}\Delta\varepsilon_p\mathbf{1} \tag{2.41}$$

where $\Delta\varepsilon_p$ and $\Delta\varepsilon_q$ are the dilatational and equivalent strains. $\Delta\varepsilon_p$, $\Delta\varepsilon_q$, and $\mathbf{n}$ are defined as, $\mathbf{n}=\frac{3}{2q}\mathbf{s}$, $\Delta\varepsilon_p=-\Delta\lambda\frac{\partial\Phi}{\partial p}$, $\Delta\varepsilon_q=\Delta\lambda\frac{\partial\Phi}{\partial q}$. Then, the stress tensor can be rewritten as follows.

$$\bar{\boldsymbol{\sigma}}_0=-p\mathbf{1}+\frac{2q}{3}\mathbf{n} \tag{2.42}$$

2.2.2. Shear-modified GTN model

The original GTN model has been known to be unable to predict failure under shear deformation. Later, therefore, Xue [64] and Nahshon and Hutchinson [65] introduced the Lode angle-related damage parameter by modifying the GTN model for reproducing the ductile failure under low-stress triaxiality [64,65]. The modified GTN model by Xue is given as follows.

$$\Phi\left(p,q,H_\alpha,D\right)=\left(\frac{q}{\sigma_Y}\right)^2+2D\cosh\left(-\frac{3q_2p}{2\sigma_Y}\right)-\left(1+D^2\right) \tag{2.43}$$

where a new damage parameter D is introduced, which is a function of the void fraction and shear-induced damage. The evolution of the damage parameter additionally by shear localization is prescribed as follows.

$$\Delta D=K_D\left(q_1\Delta f+\Delta D_{shear}\right) \tag{2.44}$$

$$K_D=\begin{cases}1, & D<D_c\\ \dfrac{\left(1/q_1-f_c\right)}{\left(f_f-f_c\right)}, & D_c<D\le 1\end{cases} \tag{2.45}$$

where K_D is the damage-related coefficient and $D_c=q_1f_c$. Note that Equation (2.43) becomes Equation (2.32) if the shear-induced failure is

ignored. When the value of the damage parameter exceeds D_c, the damage evolution is accelerated. Finally, it reaches 1, which initiates ultimate failure. Herein, the damage evolution by shear deformation is described by ΔD_{shear} in Equation (2.44). Xue [63] also suggested that the damage by shear deformation can be referred to the results of McClintock *et al.* [66] and Berg [67], and proposed the evolution law.

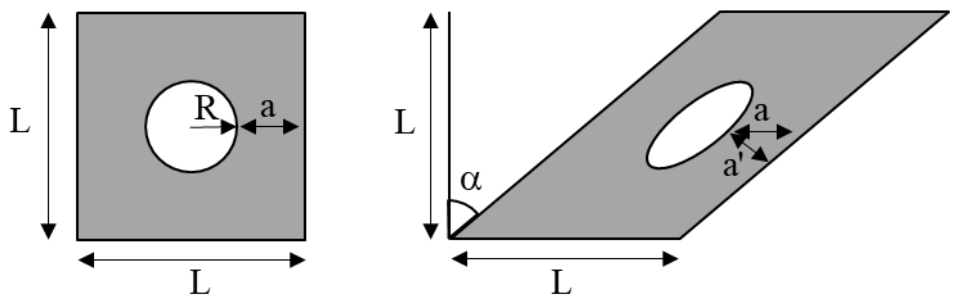

(a) (b)

Figure 2-2. Unit cell with void. (a) Undeformed and (b) deformed configurations.

Figure 2-2 shows the shear deformation of a unit cell containing a void in the center. Xue [63] assumed the minimum distance between the voids could be changed from $2a$ to $2a'$ [Figure 2-2(b)] due to the deformation. The minimum distance between the cell boundary and the void a is

$$a = \frac{L}{2} - R. \tag{2.46}$$

Through simple shearing, the unit cell of Figure 2-2(a) can be deformed, as shown in Figure 2-2(b). The simple shear strain γ can be expressed as the

angle α resulting from deformation as

$$\tan\alpha = \gamma \tag{2.47}$$

Therefore, the minimum distance between the void and the cell boundary in the deformed configuration can be represented as

$$a' = a\cos\alpha = \frac{a}{\sqrt{1+\gamma^2}}. \tag{2.48}$$

The logarithmic artificial strain ε_{art}, which results by reducing the minimum distance, was newly introduced by Xue [68].

$$\varepsilon_{art} = \ln\frac{a}{a'} = \ln\sqrt{1+\gamma^2} \tag{2.49}$$

Equation (2.49) can be reformulated with Taylor series expansion.

$$\varepsilon_{art} \approx \frac{1}{2}\gamma^2 \tag{2.50}$$

McClintock *et al.* [66] proposed a fracture criterion in the shear band that void contacts the longitudinal direction of the shear band.

$$\varepsilon_{shearband} = \frac{L}{2R} \tag{2.51}$$

The damage caused by the shear deformation was defined by Xue [68] as follows.

$$D_{shear} = \frac{\varepsilon_{art}}{\varepsilon_{shearband}} \approx \frac{R}{L}\gamma^2 \tag{2.52}$$

The void volume fraction of the 3D case is expressed as follows.

$$f = \frac{1}{L^3}\left(\frac{4}{3}\pi R^3\right) \tag{2.53}$$

Equation (2.53) can be rearranged as follows.

$$\frac{R}{L}=\left(\frac{3}{4}\frac{f}{\pi}\right)^{1/3} \tag{2.54}$$

Also, the simple shear strain can be expressed in terms of the equivalent plastic strain as

$$\gamma^2=3\varepsilon_q^2. \tag{2.55}$$

Then, the shear-induced damage is given as

$$D_{shear}=q_3 f^{q_4}\varepsilon_q^2. \tag{2.56}$$

Also, the shear damage increment can be represented as follows.

$$\Delta D_{shear}=q_3 f^{q_4}\varepsilon_q\Delta\varepsilon_q. \tag{2.57}$$

where q_3 and q_4 are material parameters. From a previous study, $q_3=3.38$, $q_4=1/2$ and $q_3=3.72$, $q_4=1/3$ were recommended for 2D and 3D models, respectively. The Lode angle-related parameter g_θ was introduced so that Equation (2.57) only works under stress triaxiality of shear.

$$\Delta D_{shear}=q_3 f^{q_4} g_\theta\varepsilon_q\Delta\varepsilon_q, \tag{2.58}$$

$$g_\theta=1-\frac{6|\theta_L|}{\pi} \tag{2.59}$$

$$\theta_L=\tan^{-1}\left[\frac{2}{\sqrt{3}}\left(\frac{s_2-s_3}{s_1-s_3}-\frac{1}{2}\right)\right] \tag{2.60}$$

where s_1, s_2, and s_3 are principal deviatoric stress components. Under a simple tension condition, the stress triaxiality and the Lode angle are 1/3 and $\theta_L=-\pi/6$ (or $g_\theta=0$); thus, the shear damage effect disappears. In contrast, under pure shear deformation, the stress triaxiality is 0, while $\theta_L=0$ (or $g_\theta=1$), which leads to the shear-induced failure evolution. Herein, when the

stress triaxiality exceeds 1/3 (or higher stress triaxiality region), the damage contribution from shear is assumed to be negligible.

Herein, implicit finite element (FE) simulation was employed; thus, the above constitutive laws were implemented into the ABAQUS FE software with user material subroutine, UMAT. Additionally, the consistent tangent modulus is defined as follows.

$$\mathbf{C}_j = \left(\frac{\partial \overline{\boldsymbol{\sigma}}_0}{\partial \overline{\boldsymbol{\varepsilon}}_0} \right)_{t+\Delta t} \tag{2.61}$$

Numerical implementation of the modified GTN model is presented in the next subsection.

2.2.3. Implementation of shear-modified GTN model

The backward Euler procedure for the GTN model was proposed by Aravas [68]. Based on the work of Aravas, the implementation strategy of the shear-modified GTN model is introduced as follows [69,70]. The modified GTN yield function proposed by Xue [64] is

$$\Phi\left(p, q, H_\alpha\right) = \left(\frac{q}{\sigma_Y} \right)^2 + 2D\cosh\left(-\frac{3q_2 p}{2\sigma_Y} \right) - \left(1 + D^2\right) = 0 . \tag{2.62}$$

The additive decomposition of the strain increment is assumed

$$\Delta\overline{\boldsymbol{\varepsilon}}_{t+\Delta t} = \Delta\overline{\boldsymbol{\varepsilon}}^{e}_{t+\Delta t} + \Delta\overline{\boldsymbol{\varepsilon}}^{p}_{t+\Delta t} \tag{2.63}$$

For conciseness, the subscript "*0*", which means the matrix phase, is omitted. t and $t+\Delta t$ are the time values at the start and end of the increment, respectively.

The trial stress tensor can be obtained from Hooke's law. There is no plastic

strain increment for the trial stress.

$$\bar{\boldsymbol{\sigma}}^{i}_{t+\Delta t} = \mathbf{C}^{e} : \left(\bar{\boldsymbol{\varepsilon}}^{e}_{t} + \Delta \bar{\boldsymbol{\varepsilon}}_{t+\Delta t} \right) \tag{2.64}$$

$\mathbf{C}^{e}$ is the fourth-order elastic stiffness tensor for the matrix. $\bar{\boldsymbol{\varepsilon}}^{e}_{t}$ is the elastic strain of the last time increment. With the trial stress tensor, the hydrostatic and equivalent stresses can be computed as follows. The trial variables have superscript "*i*".

$$p^{i} = -\frac{1}{3} \bar{\boldsymbol{\sigma}}^{i}_{t+\Delta t} : \mathbf{1} \tag{2.65}$$

$$q^{i} = \sqrt{\frac{3}{2} \left(\mathbf{s}^{i} : \mathbf{s}^{i} \right)} \tag{2.66}$$

$\mathbf{1}$ is the second-order identity tensor and $\mathbf{s}$ is the deviatoric stress tensor.

The Kuhn-Tucker and consistency conditions should be satisfied to describe the elastoplastic behavior of the material [71] numerically.

$$\Phi\left(p, q, H_{\alpha} \right) \le 0, \quad \dot{\Phi}\left(p, q, H_{\alpha} \right) \le 0 \tag{2.67}$$

For

$$\Phi\left(p^{i}, q^{i}, H^{i}_{\alpha} \right) \le 0, \quad \dot{\Phi}\left(p^{i}, q^{i}, H^{i}_{\alpha} \right) \le 0,$$

with trial values, the material undergoes only elastic deformation. Then, the conditions are fulfilled; therefore, the time step is completed with trial values. In contrast, for

$$\Phi\left(p^{i}, q^{i}, H^{i}_{\alpha} \right) > 0, \quad \dot{\Phi}\left(p^{i}, q^{i}, H^{i}_{\alpha} \right) > 0,$$

with trial values, the material begins to deform plastically. The conditions are violated. Therefore, the values should be corrected using Newton's method to meet the conditions.

The plastic flow is defined using the normality rule.

$$\Delta\bar{\boldsymbol{\varepsilon}}^{p} = \Delta\lambda\left(\frac{\partial\Phi}{\partial\bar{\boldsymbol{\sigma}}}\right)_{t+\Delta t} \tag{2.68}$$

By using chain rule with Equations (2.65) and (2.66), the plastic flow can be rewritten as

$$\Delta\bar{\boldsymbol{\varepsilon}}^{p} = \Delta\lambda\left(\frac{\partial\Phi}{\partial q}\mathbf{n}_{t+\Delta t} - \frac{1}{3}\frac{\partial\Phi}{\partial p}\mathbf{1}\right) = \Delta\varepsilon_{q}\mathbf{n}_{t+\Delta t} + \frac{1}{3}\Delta\varepsilon_{p}\mathbf{1}. \tag{2.69}$$

Where

$$\mathbf{n}_{t+\Delta t} = \frac{3}{2q^{i}}\mathbf{s}^{i}, \tag{2.70}$$

$$\Delta\varepsilon_{p} = -\Delta\lambda\frac{\partial\Phi}{\partial p},\ \Delta\varepsilon_{q} = \Delta\lambda\frac{\partial\Phi}{\partial q}. \tag{2.71}$$

$\Delta\varepsilon_{p}$ and $\Delta\varepsilon_{q}$ are increments of the dilatational and equivalent strains in the time step, respectively. The stress tensor can be expressed as follows.

$$\bar{\boldsymbol{\sigma}}_{t+\Delta t} = -p_{t+\Delta t}\mathbf{1} + \frac{2q_{t+\Delta t}}{3}\mathbf{n} \tag{2.72}$$

$$\bar{\boldsymbol{\sigma}}_{t+\Delta t} = \bar{\boldsymbol{\sigma}}^{i}_{t+\Delta t} - K\Delta\varepsilon_{p}\mathbf{1} - 2G\Delta\varepsilon_{q}\mathbf{n}_{t+\Delta t} \tag{2.73}$$

Equation (2.73) results from combining Equations (2.63), (2.64), and (2.69). K is the bulk modulus and G is the shear modulus. $\mathbf{n}_{t+\Delta t}$ can be obtained using only the trial values, as described in Equation (2.70), because the trial and corrected stresses are arranged along the $\mathbf{n}_{t+\Delta t}$ direction [Equation (2.73)]. The state variables in this study are the equivalent plastic strain of the matrix, the void fraction, and the accumulated damage. It can be expressed as follows.

$$\Delta H_{\alpha} = h_{\alpha}\left(p, q, \Delta\varepsilon_{p}, \Delta\varepsilon_{q}, H_{\beta}\right) \tag{2.74}$$

$H_{1} = e^{p}, H_{2} = f, H_{3} = D$

From the plastic work equivalence, it is possible to define the relationship between the plastic strain of the matrix and macromatrix-containing voids.

$$\bar{\boldsymbol{\sigma}} : \Delta \bar{\boldsymbol{\varepsilon}}^{p} = (1-f)\sigma_{Y} \Delta e^{p} \tag{2.75}$$

$$\Delta e^{p} = \frac{\bar{\boldsymbol{\sigma}} : \Delta \bar{\boldsymbol{\varepsilon}}^{p}}{(1-f)\sigma_{Y}} = \frac{-p\Delta\varepsilon_{p} + q\Delta\varepsilon_{q}}{(1-f)\sigma_{Y}} \tag{2.76}$$

Using Equations (2.69) and (2.72), the equivalent plastic strain increment of the matrix can be rewritten as a function of $\Delta\varepsilon_{p}$ and $\Delta\varepsilon_{q}$. The increment of other state variables also can be expressed as a function of $\Delta\varepsilon_{p}$ and $\Delta\varepsilon_{q}$.

$$\Delta f = (1-f)\Delta\varepsilon_{p} \tag{2.77}$$

$$\Delta D = K_{D}\left(q_{1}\Delta f + \Delta D_{shear}\right) = K_{D}\left\{(1-f)q_{1}\Delta\varepsilon_{p} + q_{3} f^{q_{4}} g_{\theta}\varepsilon_{q}\Delta\varepsilon_{q}\right\} \tag{2.78}$$

Using Equations (2.73) and (2.65), the mean stress can also be rewritten as a function of $\Delta\varepsilon_{p}$. The equivalent stress is a function of $\Delta\varepsilon_{q}$ with Equations (2.73) and (2.66).

$$p = p^{i} + K\Delta\varepsilon_{p} \tag{2.79}$$

$$q = q^{i} - 3G\Delta\varepsilon_{q} \tag{2.80}$$

All the above variables for the GTN model are the functions of $\Delta\varepsilon_{p}$ and $\Delta\varepsilon_{q}$. Therefore, two equations are needed to identify two primary variables using Newton's method.

$$\Delta\varepsilon_{p}\left(\frac{\partial\Phi}{\partial q}\right) + \Delta\varepsilon_{q}\left(\frac{\partial\Phi}{\partial p}\right) = 0 \tag{2.81}$$

$$\Phi\left(p, q, H_{\alpha}\right) = 0 \tag{2.82}$$

Equation (2.81) results from Equation (2.71) by eliminating the positive scalar $\Delta\lambda$. By partially differentiating Equations (2.81) and (2.82) with two primary variables, it can be summarized as follows.

$$\begin{bmatrix} A_{11} & A_{12} \\ A_{21} & A_{22} \end{bmatrix} \begin{bmatrix} d\Delta\varepsilon_p \\ d\Delta\varepsilon_q \end{bmatrix} = \begin{bmatrix} B_1 \\ B_2 \end{bmatrix} \tag{2.83}$$

The components in Equation (2.83) are

$$b_1 = -\Delta\varepsilon_p \left(\frac{\partial \Phi}{\partial q} \right) - \Delta\varepsilon_q \left(\frac{\partial \Phi}{\partial p} \right), \tag{2.84}$$

$$b_2 = -\Phi\,, \tag{2.85}$$

$$\begin{aligned} A_{11} = & \left(\frac{\partial \Phi}{\partial q} \right) + \Delta\varepsilon_p \left(K \frac{\partial^2 \Phi}{\partial p \partial q} + \sum_{\alpha=1}^{n} \frac{\partial^2 \Phi}{\partial q \partial H_\alpha} \frac{\partial H_\alpha}{\partial \Delta\varepsilon_p} \right) \\ & + \Delta\varepsilon_q \left(K \frac{\partial^2 \Phi}{\partial p^2} + \sum_{\alpha=1}^{n} \frac{\partial^2 \Phi}{\partial p \partial H_\alpha} \frac{\partial H_\alpha}{\partial \Delta\varepsilon_p} \right) \end{aligned}, \tag{2.86}$$

$$\begin{aligned} A_{12} = & \left(\frac{\partial \Phi}{\partial p} \right) + \Delta\varepsilon_p \left(-3G \frac{\partial^2 \Phi}{\partial q^2} + \sum_{\alpha=1}^{n} \frac{\partial^2 \Phi}{\partial q \partial H_\alpha} \frac{\partial H_\alpha}{\partial \Delta\varepsilon_q} \right) \\ & + \Delta\varepsilon_q \left(-3G \frac{\partial^2 \Phi}{\partial p \partial q} + \sum_{\alpha=1}^{n} \frac{\partial^2 \Phi}{\partial p \partial H_\alpha} \frac{\partial H_\alpha}{\partial \Delta\varepsilon_q} \right) \end{aligned}, \tag{2.87}$$

$$A_{21} = K \frac{\partial \Phi}{\partial p} + \sum_{\alpha=1}^{n} \frac{\partial \Phi}{\partial H_\alpha} \frac{\partial H_\alpha}{\partial \Delta\varepsilon_p}\,, \text{ and} \tag{2.88}$$

$$A_{22} = -3G \frac{\partial \Phi}{\partial p} + \sum_{\alpha=1}^{n} \frac{\partial \Phi}{\partial H_\alpha} \frac{\partial H_\alpha}{\partial \Delta\varepsilon_q}\,. \tag{2.89}$$

The primary variables are updated as follows in the k-th iteration.

$$\Delta\varepsilon_p^{k+1} = \Delta\varepsilon_p^{k} + d\Delta\varepsilon_p$$

$$\Delta\varepsilon_q^{k+1} = \Delta\varepsilon_q^{k} + d\Delta\varepsilon_q$$

If $d\Delta\varepsilon_p$ and $d\Delta\varepsilon_q$ are < the tolerance, it ends the iteration. The partial derivatives in Equations (2.86)–(2.89) are presented in Appendix A.

2.2.4. Calculation of consistent tangent modulus

Aravas also covered the procedure for calculating consistent tangent modulus. The consistent tangent modulus affects the convergence of the computational simulation [68]. Herein, the consistent tangent modulus of the macromatrix is used to establish the relationship of each phase. Based on this relationship, the strain increment for each phase is determined. The consistent tangent modulus can be expressed as

$$\mathbf{C}_j = \left(\frac{\partial \overline{\boldsymbol{\sigma}}}{\partial \overline{\boldsymbol{\varepsilon}}} \right)_{t+\Delta t}. \tag{2.90}$$

With the combination of Equations (2.63), (2.64), and (2.69), the stress tensor can be written as

$$\overline{\boldsymbol{\sigma}} = \mathbf{C} : \left(\overline{\boldsymbol{\varepsilon}} - \overline{\boldsymbol{\varepsilon}}_t^{\,p} - \frac{1}{3}\Delta\varepsilon_p \mathbf{1} - \Delta\varepsilon_q \mathbf{n} \right). \tag{2.91}$$

The stress tensor differential $\partial\overline{\boldsymbol{\sigma}}$ is expressed as

$$\partial\overline{\boldsymbol{\sigma}} = \mathbf{C} : \left(\partial\overline{\boldsymbol{\varepsilon}} - \frac{1}{3}\partial\Delta\varepsilon_p \mathbf{1} - \partial\Delta\varepsilon_q \mathbf{n} - \Delta\varepsilon_q \frac{\partial \mathbf{n}}{\partial \overline{\boldsymbol{\sigma}}} : \partial\overline{\boldsymbol{\sigma}} \right). \tag{2.92}$$

with the differential of the independent variables, $\partial\overline{\boldsymbol{\varepsilon}}$, $\partial\Delta\varepsilon_p$, $\partial\Delta\varepsilon_p$, and $\partial\mathbf{n}$. The partial derivatives of $\mathbf{n}$ according to the stress is computed as follows from Equation (2.70).

$$\frac{\partial \mathbf{n}}{\partial \overline{\boldsymbol{\sigma}}} = \frac{1}{q}\left(\frac{3}{2}\mathbf{I} - \frac{1}{2}\mathbf{1}\otimes\mathbf{1} - \mathbf{n}\otimes\mathbf{n} \right) \tag{2.93}$$

$$I_{ijkl} = \delta_{ik}\delta_{jl}$$

$$\left(\mathbf{n}\otimes\mathbf{n}\right)_{ijkl} = n_{ij}n_{kl}$$

$\mathbf{I}$ is the fourth-order identity tensor and δ_{ik} is the Kronecker delta function.

$\otimes$ indicates the dyadic product. $\partial\Delta\varepsilon_p$ and $\partial\Delta\varepsilon_q$ must be removed to express Equation (2.92) in terms of $\partial\bar{\boldsymbol{\sigma}}$ and $\partial\bar{\boldsymbol{\varepsilon}}$. The process for this is listed as follows.

Differentiate Equation (2.81)

$$\begin{aligned}&\partial\Delta\varepsilon_p\left(\frac{\partial\Phi}{\partial q}\right)+\Delta\varepsilon_p\left[\left(\frac{\partial^2\Phi}{\partial p\partial q}\frac{\partial p}{\partial\bar{\boldsymbol{\sigma}}}+\frac{\partial^2\Phi}{\partial q^2}\frac{\partial q}{\partial\bar{\boldsymbol{\sigma}}}\right):\partial\bar{\boldsymbol{\sigma}}+\sum_{\alpha=1}^{n}\frac{\partial^2\Phi}{\partial q\partial H_\alpha}\partial H_\alpha\right]\\&+\partial\Delta\varepsilon_q\left(\frac{\partial\Phi}{\partial p}\right)+\Delta\varepsilon_q\left[\left(\frac{\partial^2\Phi}{\partial p^2}\frac{\partial p}{\partial\bar{\boldsymbol{\sigma}}}+\frac{\partial^2\Phi}{\partial p\partial q}\frac{\partial q}{\partial\bar{\boldsymbol{\sigma}}}\right):\partial\bar{\boldsymbol{\sigma}}+\sum_{\alpha=1}^{n}\frac{\partial^2\Phi}{\partial p\partial H_\alpha}\partial H_\alpha\right]=0\end{aligned}\quad . \tag{2.94}$$

From Equation (2.82),

$$\left(\frac{\partial\Phi}{\partial p}\frac{\partial p}{\partial\bar{\boldsymbol{\sigma}}}+\frac{\partial\Phi}{\partial q}\frac{\partial q}{\partial\bar{\boldsymbol{\sigma}}}\right):\partial\bar{\boldsymbol{\sigma}}+\sum_{\alpha=1}^{n}\frac{\partial\Phi}{\partial H_\alpha}\partial H_\alpha=0\,. \tag{2.95}$$

The differential of the state variables is

$$\partial H_\alpha=\sum_{\beta=1}^{n}c_{\alpha\beta}\left[\frac{\partial h_\beta}{\partial\Delta\varepsilon_p}\partial\Delta\varepsilon_p+\frac{\partial h_\beta}{\partial\Delta\varepsilon_q}\partial\Delta\varepsilon_q+\left(\frac{\partial h_\beta}{\partial p}\frac{\partial p}{\partial\bar{\boldsymbol{\sigma}}}+\frac{\partial h_\beta}{\partial q}\frac{\partial q}{\partial\bar{\boldsymbol{\sigma}}}\right):\partial\bar{\boldsymbol{\sigma}}\right]. \tag{2.96}$$

where

$$\frac{\partial p}{\partial\bar{\boldsymbol{\sigma}}}=-\frac{1}{3}\mathbf{1}$$

and

$$\frac{\partial q}{\partial\bar{\boldsymbol{\sigma}}}=\mathbf{n}\,.$$

Equations (2.94), (2.95), and (2.96) can be rearranged by $\partial\Delta\varepsilon_p$, $\partial\Delta\varepsilon_q$, and $\partial\bar{\boldsymbol{\sigma}}$ in the following form.

$$\begin{bmatrix}A_{11}&A_{12}\\A_{21}&A_{22}\end{bmatrix}\begin{bmatrix}\partial\Delta\varepsilon_p\\\partial\Delta\varepsilon_q\end{bmatrix}=\begin{bmatrix}B_{11}&B_{12}\\B_{21}&B_{22}\end{bmatrix}\begin{bmatrix}\mathbf{1}\\\mathbf{n}\end{bmatrix}:\partial\bar{\boldsymbol{\sigma}} \tag{2.97}$$

Each component in Equation (2.97) is summarized as follows.

$$A_{11} = \frac{\partial \Phi}{\partial q} + \sum_{\alpha=1}^{n}\sum_{\beta=1}^{n}\left(\Delta\varepsilon_p \frac{\partial^2 \Phi}{\partial q \partial H_\alpha} + \Delta\varepsilon_q \frac{\partial^2 \Phi}{\partial p \partial H_\alpha} \right) c_{\alpha\beta} \frac{\partial h_\beta}{\partial \Delta\varepsilon_p}$$

$$A_{12} = \frac{\partial \Phi}{\partial p} + \sum_{\alpha=1}^{n}\sum_{\beta=1}^{n}\left(\Delta\varepsilon_p \frac{\partial^2 \Phi}{\partial q \partial H_\alpha} + \Delta\varepsilon_q \frac{\partial^2 \Phi}{\partial p \partial H_\alpha} \right) c_{\alpha\beta} \frac{\partial h_\beta}{\partial \Delta\varepsilon_q}$$

$$A_{21} = \sum_{\alpha=1}^{n}\sum_{\beta=1}^{n} \frac{\partial \Phi}{\partial H_\alpha} c_{\alpha\beta} \frac{\partial h_\beta}{\partial \Delta\varepsilon_p}$$

$$A_{22} = \sum_{\alpha=1}^{n}\sum_{\beta=1}^{n} \frac{\partial \Phi}{\partial H_\alpha} c_{\alpha\beta} \frac{\partial h_\beta}{\partial \Delta\varepsilon_q}$$

$$B_{11} = \frac{1}{3}\Delta\varepsilon_p \left(\frac{\partial^2 \Phi}{\partial p \partial q} + \sum_{\beta=1}^{n}\sum_{\alpha=1}^{n} \frac{\partial^2 \Phi}{\partial q \partial H_\alpha} c_{\alpha\beta} \frac{\partial h_\beta}{\partial p} \right) + \frac{1}{3}\Delta\varepsilon_q \left(\frac{\partial^2 \Phi}{\partial p^2} + \sum_{\beta=1}^{n}\sum_{\alpha=1}^{n} \frac{\partial^2 \Phi}{\partial p \partial H_\alpha} c_{\alpha\beta} \frac{\partial h_\beta}{\partial p} \right)$$

$$B_{12} = -\Delta\varepsilon_p \left(\frac{\partial^2 \Phi}{\partial q^2} + \sum_{\beta=1}^{n}\sum_{\alpha=1}^{n} \frac{\partial^2 \Phi}{\partial q \partial H_\alpha} c_{\alpha\beta} \frac{\partial h_\beta}{\partial q} \right) - \Delta\varepsilon_q \left(\frac{\partial^2 \Phi}{\partial q \partial p} + \sum_{\beta=1}^{n}\sum_{\alpha=1}^{n} \frac{\partial^2 \Phi}{\partial p \partial H_\alpha} c_{\alpha\beta} \frac{\partial h_\beta}{\partial q} \right)$$

$$B_{21} = \frac{1}{3}\left(\frac{\partial \Phi}{\partial p} + \sum_{\beta=1}^{n}\sum_{\alpha=1}^{n} \frac{\partial \Phi}{\partial H_\alpha} c_{\alpha\beta} \frac{\partial h_\beta}{\partial p} \right)$$

$$B_{22} = -\left(\frac{\partial \Phi}{\partial q} + \sum_{\beta=1}^{n}\sum_{\alpha=1}^{n} \frac{\partial \Phi}{\partial H_\alpha} c_{\alpha\beta} \frac{\partial h_\beta}{\partial q} \right)$$

Equation (2.97) can be rewritten as

$$\begin{bmatrix} \partial\Delta\varepsilon_p \\ \partial\Delta\varepsilon_q \end{bmatrix} = \begin{bmatrix} m_{p1} & m_{pn} \\ m_{q1} & m_{qn} \end{bmatrix} \begin{bmatrix} \mathbf{1} \\ \mathbf{n} \end{bmatrix} : \partial\bar{\boldsymbol{\sigma}} \,. \tag{2.98}$$

Substituting the variables $\partial\Delta\varepsilon_q$ and $\partial\Delta\varepsilon_p$, which are functions of $\partial\bar{\boldsymbol{\sigma}}$, into Equation (2.92) transforms it into a function of $\partial\bar{\boldsymbol{\sigma}}$ and $\partial\bar{\boldsymbol{\varepsilon}}$ as follows.

$$\left(\mathbf{I} + \mathbf{C} : \mathbf{M}\right) : \partial\bar{\boldsymbol{\sigma}} = \mathbf{C} : \partial\bar{\boldsymbol{\varepsilon}} \tag{2.99}$$

where

$$\mathbf{M} = \tfrac{1}{3} m_{p1} \mathbf{1} \otimes \mathbf{1} + \tfrac{1}{3} m_{pn} \mathbf{1} \otimes \mathbf{n} + m_{q1} \mathbf{n} \otimes \mathbf{1} + m_{qn} \mathbf{n} \otimes \mathbf{n} + \Delta \varepsilon_q \frac{\partial \mathbf{n}}{\partial \bar{\boldsymbol{\sigma}}}.$$

The consistent tangent modulus is given as

$$\mathbf{C}_j = \left(\mathbf{I} + \mathbf{C} : \mathbf{M}\right)^{-1} : \mathbf{C} = \left(\mathbf{C}^{-1} + \mathbf{M}\right)^{-1}. \tag{2.100}$$

The partial derivatives are presented in Appendix A.

2.3. Weibull distribution function

In GTN-based ductile fracture modeling, an appropriate void nucleation law is essential. To date, the void nucleation law has often been employed based on a statistical and empirical equation as a function of the mean and standard deviation of the plastic strain that initiates the voids' nucleation in the matrix. As an alternative approach, the Weibull distribution was introduced to determine the probabilistic cracking of the Si particles embedded in the Al matrix, which acts as initiation sites of the void nucleation [3,4]. A similar approach was successfully applied to the cracks of brittle particles in ductile matrices, such as MMC [48–50,72–76].

The Weibull distribution function is expressed as follows.

$$B = 1 - \exp\left[-\frac{V}{V_0} \left(\frac{\sigma_1}{\sigma_{\mathrm{f}}} \right)^m \right], \tag{2.101}$$

where B is the probability for cracked Si particles under the maximum principal stress criterion. In other words, the Si particle is assumed to crack statistically, and initiating the void nucleation when the stress transfers from the Al matrix satisfies the stress-based fracture criterion. In the above equation, V and σ_1 are the volume and maximum principal stress of a Si particle,

respectively. m is the Weibull modulus, and σ_f and V_0 are parameter-related stress and volume of the particles, usually determined experimentally.

The use of the maximum principal stress criterion [σ_1 in Equation (2.101)] has been rationalized by experimental observations. For example, the probability of cracked Si particles increased as the larger volume particles were loaded in the direction perpendicular to the maximum principal stress.

The identification of the Weibull parameters is challenging. Therefore, various statistical methods have been proposed to determine the parameters, such as a simplified Eshelby-type calculation, RVE-based FE simulation, or *in situ* experimental characterization [73]. For example, Lewis and Withers determined the Weibull parameters by changing the size of the particles embedded in the Al matrix [72], and Llorca *et al.* reported that the SiC particles in 2618 Al alloy obeyed the Weibull distribution function well with the Weibull modulus of 1 [74]. Brechet *et al.* showed that the Weibull modulus of the SiC particles in A356 had a large scatter between 1 and 6 [75], whereas its value was measured by Mochida *et al.* for Al_2O_3 particles in 6061 was 1.43 [73]. This large variation of the Weibull parameters may be attributed to the complex microstructural characteristics, including particle size and dimensional shape effects. For the similar Si particles in the A356 alloy with T6 temper, the Weibull parameters V_0, σ_f, and m were reported to be 33 μm^3, 3 GPa, and 3, respectively, according to Caceres and Griffiths [76].

2.4. Summary of algorithmic implementation

The FE modeling is used for predicting the fracture of the investigated cast Al

alloy by integrating the MT and GTN models and the probabilistic Weibull approach. As an FE software, the static implicit ABAQUS/Standard was used, and all the constitutive laws were implemented using the user material subroutine, UMAT.

The developed algorithm for calculating the homogenized mechanical behavior of the Al alloy (or, in general, MMCs) is a two-level iteration method, which solves the MT and GTN models. The schematic diagram of the algorithmic flow for the proposed modeling is shown in Figure 2-3, which is summarized as follows.

1) First, the total strain increment $\Delta\bar{\boldsymbol{\varepsilon}}$ according to the prescribed boundary conditions is given in the integration point. Then, the strain increment of the MMC (Al alloy) is decomposed into the component for the Al matrix $\Delta\bar{\boldsymbol{\varepsilon}}_0$ and that for the Si particles $\Delta\bar{\boldsymbol{\varepsilon}}_1$, according to the strain concentration factor tensor of the MT model.
2) The stress in the Si particles $\bar{\boldsymbol{\sigma}}_1$ can be simply calculated using the generalized Hooke's law under the assumption of isotropic linear elastic material.
3) However, the Al matrix stress $\bar{\boldsymbol{\sigma}}_0$ is computed by using the fully implicit GTN model. In this step, the first level Newton–Raphson iteration is conducted until the converged stress following the GTN model is obtained.
4) Once the converged solution is achieved during the first level iteration, the second level Newton–Raphson iteration is performed by repeating steps (1)–(3) until the MT model converges. In other words, the second

iteration is stopped when the stress change in the Si particles is within the prescribed tolerance.

5) After obtaining the stresses of the Al matrix and Si particles using the two-level iteration scheme, the initiation criterion for particle cracking is checked using the Weibull distribution. Note that this step is done in an explicit manner; thus, it is assumed that the cracking of the Si particles does not influence the Al alloy stresses. If a Si particle begins cracking, the volume of the particle is replaced with a void volume for the next time step. The updated void volume is used for the GTN model.
6) Finally, all state variables associated with plasticity and ductile fracture, stresses, and consistent tangent modulus are updated.

In the above numerical approach, the two major mechanisms of mechanical properties deterioration can be explained. First, the Al alloy stiffness decreases due to the cracking of the Si particles in the Al matrix. The cracked Si particles cannot sustain the loading or stress-free state; thus, the overall homogenized stress and stiffness by the MT mean-field method decrease as the fraction of the active Si particles decreases. Second, the mechanical properties of the Al alloy decrease through the growth and coalescence of voids introduced by the cracking of the Si particles. Therefore, the present model is more advanced than the conventional GTN-based model, in which only the void evolution effect can be considered for the mechanical degradation during plastic deformation.

For the probabilistic implementation of the Weibull distribution for

determining particle cracking, the number of particles is prescribed in the matrix point. Herein, 500 Si particles were assumed. The size distribution of the Si particles is also informed in the approach using the statistical analysis of the optical microscopy image, which will be described later. As a criterion for particle cracking, a simple method using a random number (a) varying between 0 and 1 was used. Thus, from the probability of the particle cracking B, defined as Equation (2.101), at the end of each increment, the cracking of the Si particles is determined if $B \geq a$.

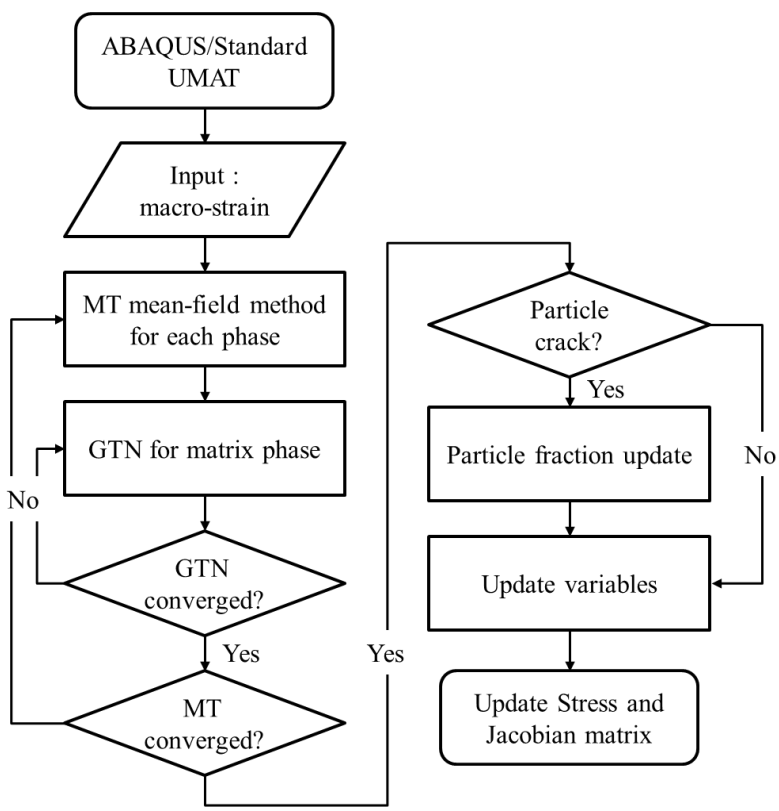

Figure 2-3. Flow chart of microstructure-based fracture model.

Figure 2-4 shows the (initial) cracking of Si particles (black), the transition of the cracked Si particles to microvoids (white), and their growth in the Al matrix (gray). Figure 2-4(a), (b), and (c) represent the start of time increment, and others denote the end of time increment. When $B < a$, the probability of particle cracking is < the random number, which leads to only the void growth using simulation [Figure 2-4(a)–(d)]. When the probability of cracking exceeds the random number $B \geq a$, an additional particle crack occurs (Figure 2-4(b)–(e). Also, at the beginning of the next time increment (Figure 2-4(c)) the cracked particles are transformed into the microvoids in the material point. Finally, the voids' volume increases as the amount occupied by the cracked Si particles.

In the proposed numerical algorithm, the nucleation of voids by the cracking of the Si particles, the growth of microvoids, and the damage increment due to the shear deformation affect the overall damage of the Al alloy. Therefore, the total damage indicator increases rapidly to 1 after large deformation. Once a material point is fully damaged (or damage indicator 1), the material point is assumed to lose the load-carrying capacity. To avoid the numerical convergence problem due to the abrupt stiffness change during failure, the material point is assumed to act like a macrovoid with the following (reduced) mechanical properties when the damage parameter exceeds 0.95.

$$\bar{\boldsymbol{\sigma}}_v = \mathbf{C}_v \bar{\boldsymbol{\varepsilon}}_v, \ \mathbf{C}_v = \mathbf{C}_0 / 10^6 \tag{2.102}$$

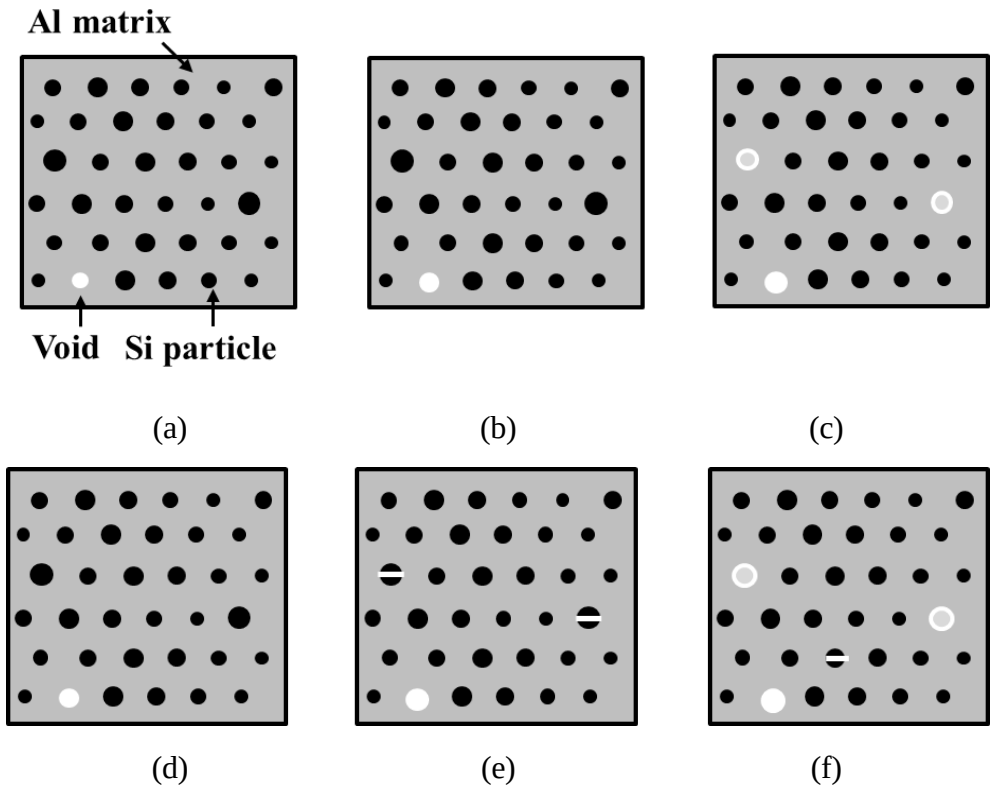

Figure 2-4. Schematics of microstructure evolution at material point. (a), (b) and (c) are start of time step increment. (d)–(f) are end of time step for (a), (b) and (c), respectively.

3. Experiments

3.1. Mechanical test

The basic mechanical properties and fracture behavior of the investigated Al alloy were measured using a universal tensile testing machine, Instron 8801™. For measuring the strain, a full field method based on the digital image correlation (DIC) was used. For the full field analysis, the VIC-3D software was used, and two CCD cameras are set, as shown in Figure 3-1. The test specimens were designed and shown in Figure 3-2(a)–(e), which correspond to the simple tension (ST), center hole (CH), notch tension (NT), in-plane shear (PS), and U-notch (UT) specimens, respectively. The gage length of the tensile test was 10 mm, whereas that of the fracture test was 25 mm.

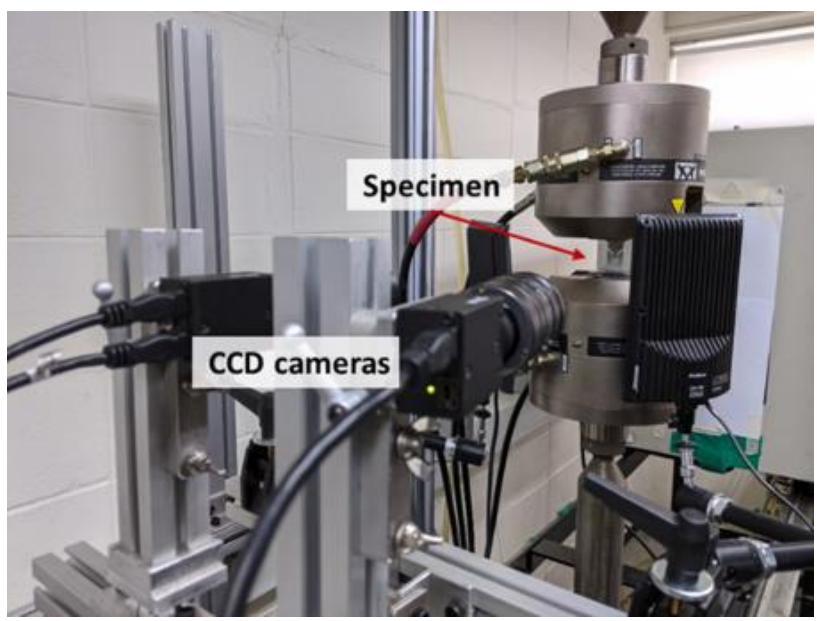

Figure 3-1. Experimental setup.

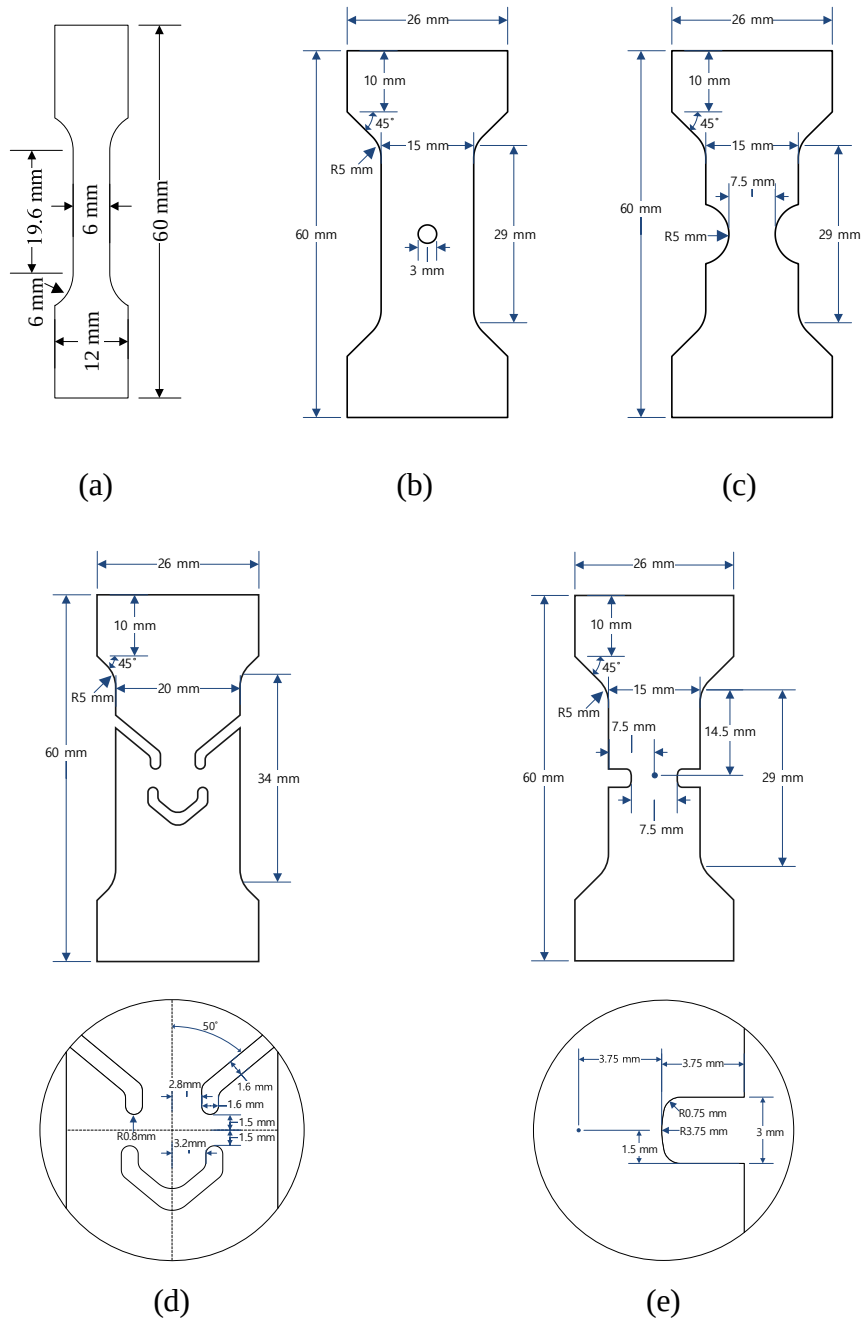

Figure 3-2. Dimension of specimens. (a) Simple tension (ST), (b) center hole (CH), (c) notch (NT), (d) in-plane shear (PS), and (e) U-notch (UT).

The conditions for the mechanical experiments and DIC are summarized in Tables 2 and 3. The crosshead speeds are 1.176 and 1 mm/min for the ST and fracture tests, respectively. The resolutions of the area of interest (AOI) are 1210 × 250 and 1210 × 630 for the ST and fracture tests, respectively.

Table 3-1. Conditions for mechanical experiments.

Frame	Instron 8801
Load cell capacity	100kN
Test speed (Simple tension test)	1.176 mm/min
Test speed (Fracture test)	1mm/min

Table 3-2. Conditions for DIC.

DIC type : Stereo DIC (3D)	
Software	VIC-3D 7
Resolution (pixels)	2448 x 2048
Resolution of AOI (Simple tension test)	1210 x 250
Resolution of AOI (Fracture test)	1210 x 630

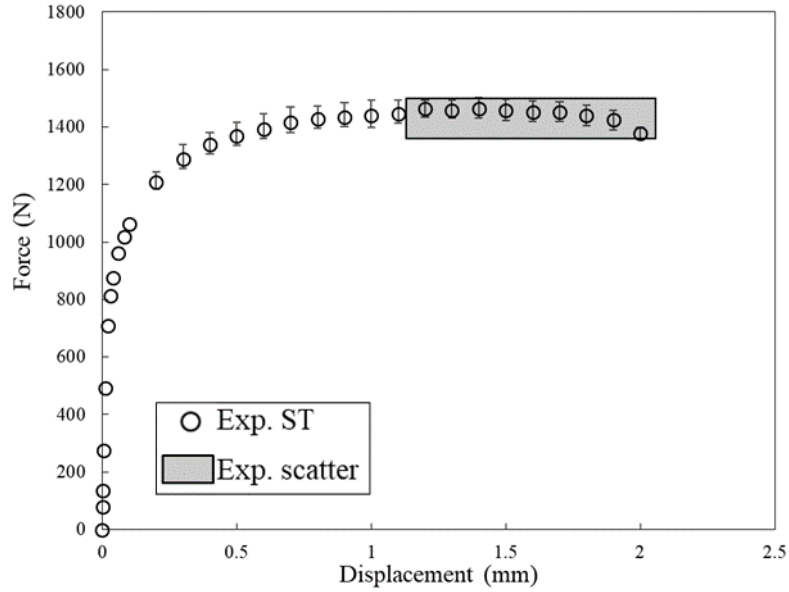
Force (N)
Displacement (mm)
Exp. ST
Exp. scatter

(a)

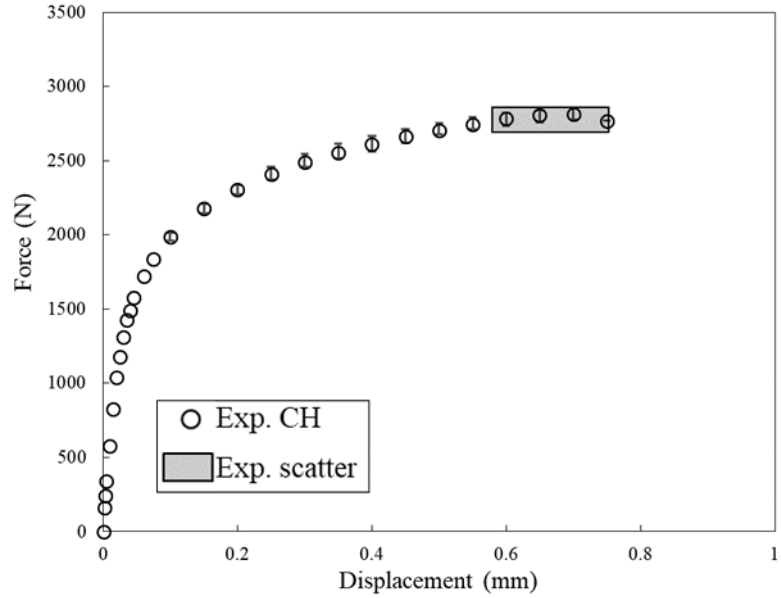
Force (N)
Displacement (mm)
Exp. CH
Exp. scatter

(b)

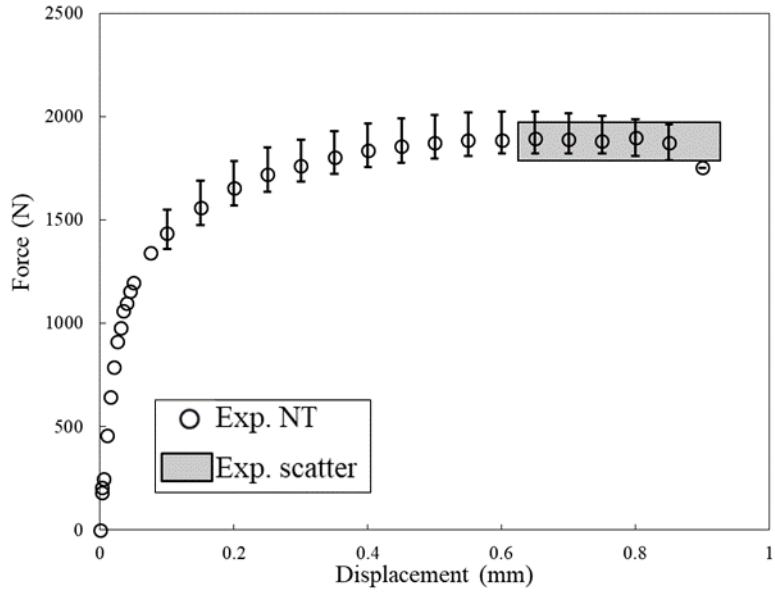

(c)

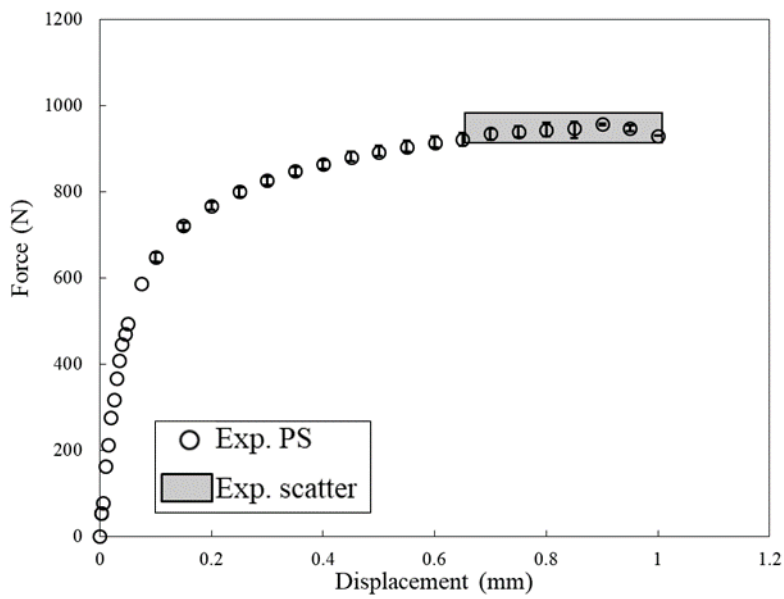

(d)

Figure 3-3. Force–displacement curves of tensile experiments with (a) Simple tension (ST), (b) center hole (CH), (c) notch (NT), and (d) in-plane shear (PS).

For the repeatability of the tests, at least five tests were conducted for each test condition. Figure 3-3(a)–(d) presents the load–displacement curves of ST, CH, NT, and PS, respectively. The square boxes indicate the experimental scatters of the average load (vertical edge) and fractured displacements (horizontal edge). The figures clearly show that the scatters in the load curves are marginal for most tests, but the fracture strains (or displacements at fracture) have significantly larger scatters for all investigated tests.

3.2. Statistical microstructural analysis

The microstructure of the investigated Al alloy is characterized by the Si particles embedded in the eutectic zone of the Al matrix, and additional macroscopic and/or microscopic voids. The macroscopic voids are often introduced during the casting process, and they mostly affect the mechanical properties negatively. Therefore, these microstructure characteristics were experimentally measured as inputs for the developed microstructure-based fracture model.

The distribution and size of the Si particles, the microvoids fraction, and the macrovoids' volume fraction are the primary parameters for modeling the ductile fracture herein. Since the microvoids were nonuniformly distributed through the Al matrix, their distribution was statistically quantified by measuring the fractions of the microvoids in different sections of the sample. Note that the microvoid fraction probability serves as an input for the integration point of the finite element (FE) model. Herein, the sample domain was divided into squares with 100-μm edge length, and the microvoids'

fraction was quantitatively measured in each divided region. Similarly, the distribution of Si particle fraction was also calculated, but the deviation in different regions was insignificant than that of microvoids. Therefore, the fraction of Si particles was averaged and assumed to be evenly distributed through the material. The average volume fraction of Si particles was 9% in the Al alloy.

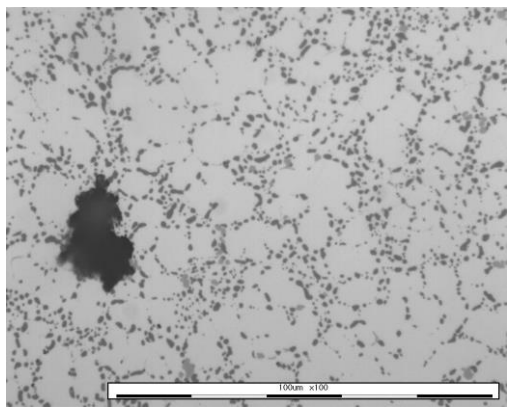

(a)

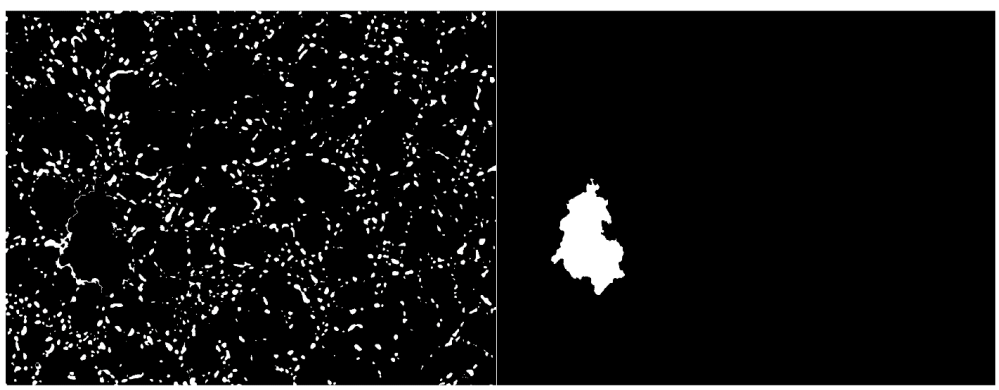

(b) (c)

Figure 3-4. (a) Optical microscope image. (b) Si particles and (c) void obtained through image analysis from (a), respectively.

The macrovoids were analyzed by X-ray microtomography using the Rayscan 250™ micro-CT machine. A voxel analyzed by X-ray microtomography, which corresponds to a pixel in two dimensions, has a size of 20 μm. The volume fraction of the macrovoids with measured sizes > 50 μm was ~0.01%. The microvoids and Si particles were observed using an optical microscope (OM). An image processing tool in MATLAB was used to analyze the microstructure quantitatively. The original OM image was converted to black and white by adjusting the contrast, which can better distinguish the voids and the Si particles, (Figure 3-4). The distribution of the void fraction and the size of the Si particles were analyzed using several OM images, and their results are shown in Figure 3-5 with a histogram and cumulative density function. The histograms were fitted to the following probability density function of the lognormal distribution.

$$y = \frac{1}{x\sigma\sqrt{2\pi}} \exp\left[-\frac{\left(\ln x - \mu\right)^2}{2\sigma^2} \right] \tag{3.1}$$

where y is a probability density as a function of x, and μ and σ are the mean and standard deviation, respectively.

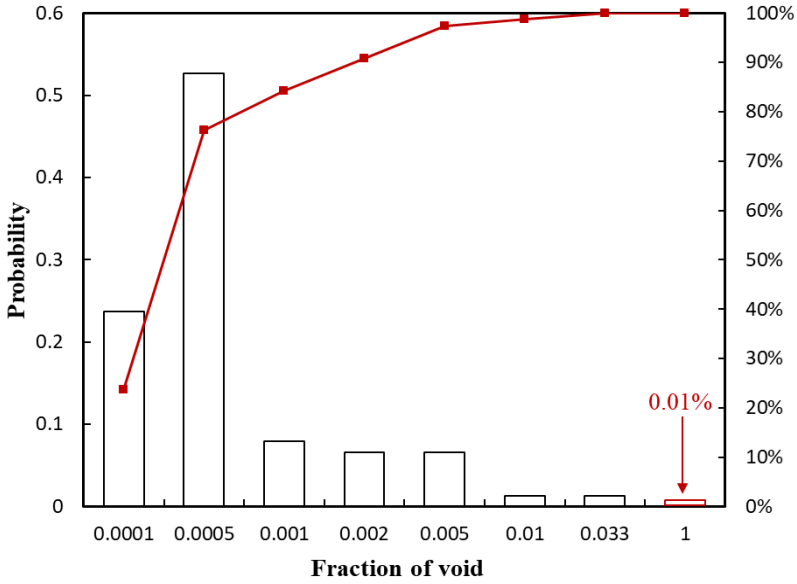

(a)

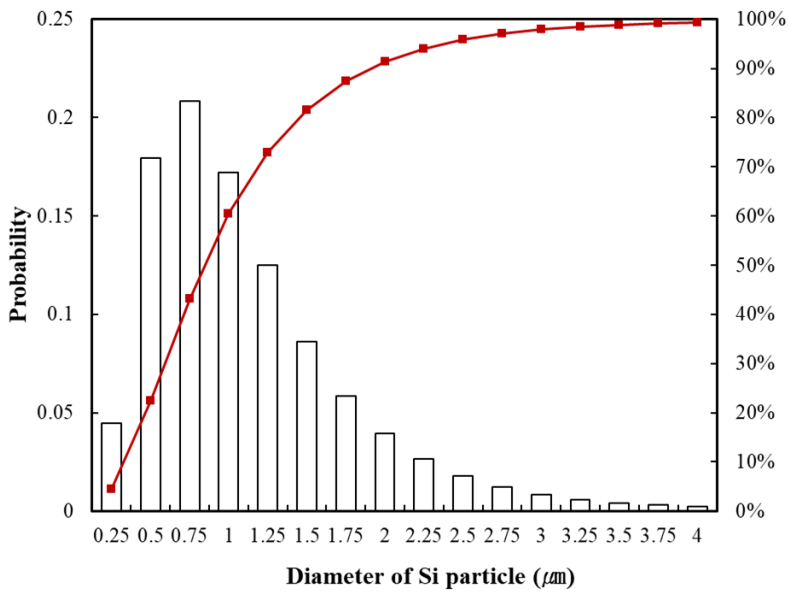

(b)

Figure 3-5. Histogram and cumulative probability of (a) fraction of voids and (b) diameter of Si particles.

Note that the diameter of the Si particles could not be accurately measured because the area measured by the OM is partially exposed in the Al matrix. Therefore, the correction was made following the work of Lewis and Withers [72] summarized in Appendix B. The identified parameters were $\mu = -0.03$, $\sigma = 0.58$ and $\mu = -7.7$, $\sigma = 1.24$ for the distribution of the Si particle size and void volume fraction, respectively.

The statistically identified volume fractions of the voids and Si particles were distributed to the FE integration points. For the macrovoids, the corresponding fraction (or 0.01%) of the integration points was assigned as the degraded mechanical properties of the voids, as in Equation (2.102).

For a distribution with 100 particles at each material point, experience has shown that a particle's volume fraction can cause void coalescence due to its size distribution. We judged that it is inappropriate for a material point to have a fracture condition with only a crack on the particle. As a compromise between the numerical efficiency and the number of Si particles for damage evolution due to multigrain cracking, 500 Si particles with size distributions according to the probability density function were assigned in each FE integration point.

3.3. Microstructural analysis using Energy-dispersive spectroscopy (EDS)

EDS is a useful technique for identifying the chemical content of microstructures. Here, the spectra from the energy-dispersive X-ray (EDX) spectroscopy analysis of the microstructures are presented.

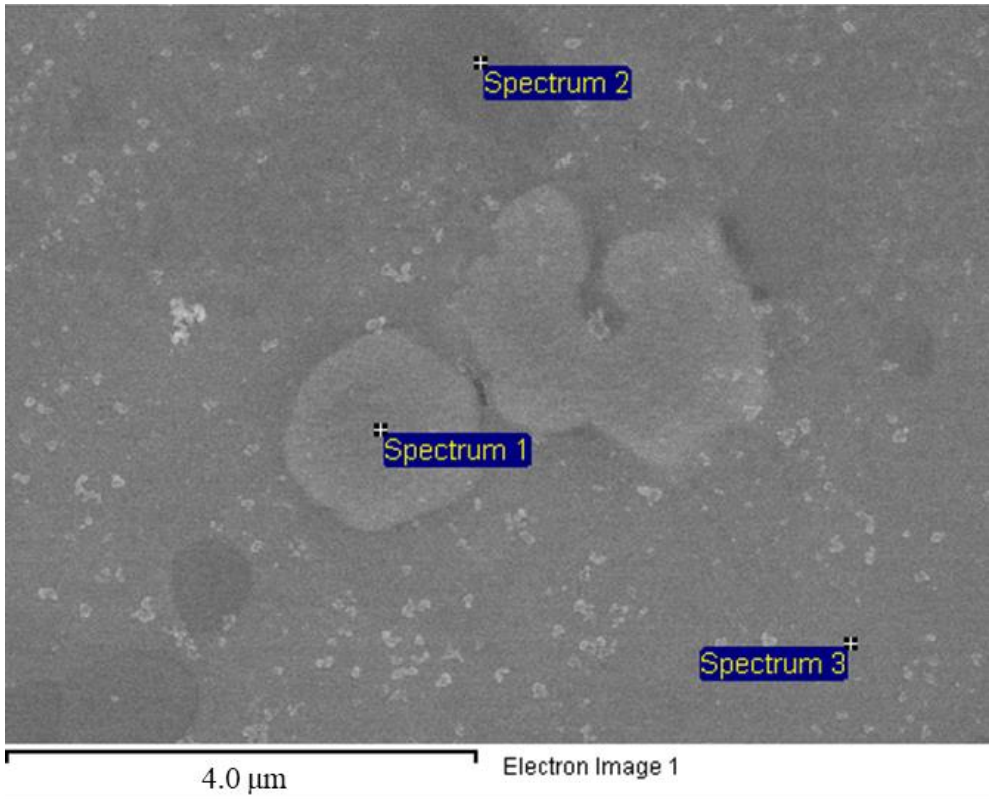
Spectrum 2
Spectrum 1
Spectrum 3
4.0 µm
Electron Image 1

(a)

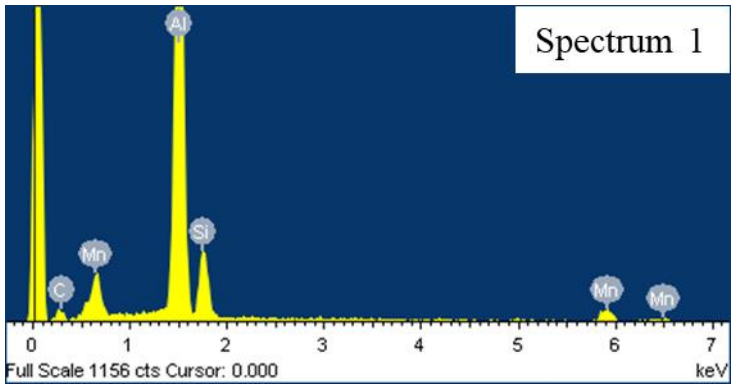
Spectrum 1
Al
Si
Mn
C
Mn
Mn
0
1
2
3
4
5
6
7
Full Scale 1156 cts Cursor: 0.000
keV

(b)

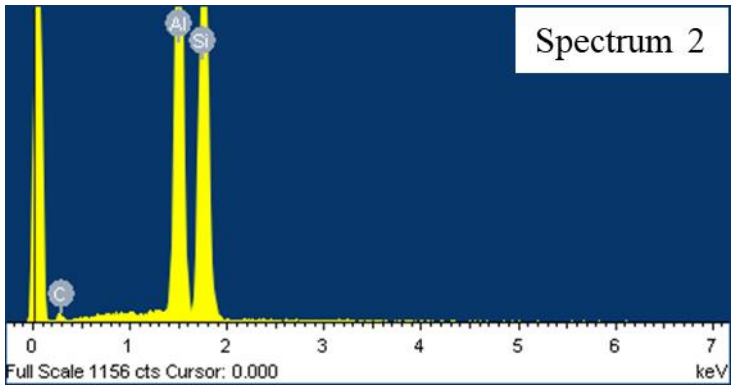

(c)

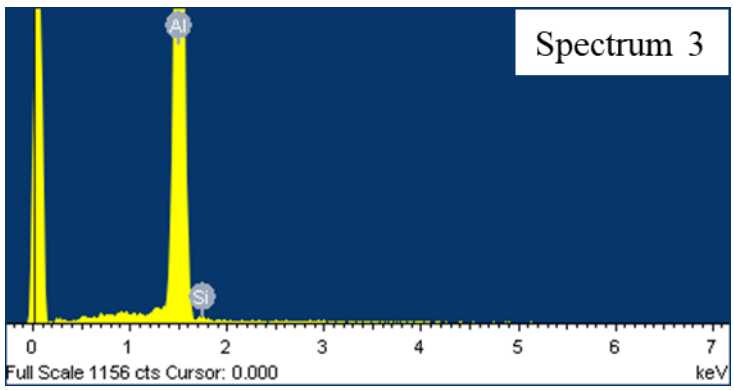

(d)

Figure 3-6. (a) Scanning electron microscopy (SEM) image. Spectra (b) 1, (c) 2, and (d) 3 are obtained by EDS analysis at each point in (a).

Figure 3-6(a) is a scanning electron microscopy (SEM) image, where each point is located on an unidentified secondary particle (point 1), Si particle (point 2), and Al matrix (point 3) at the observation time. Figure 3-6(b)–(d) presents the chemical content spectra containing quantitative information obtained from the EDX spectroscopy analysis of each point in Figure 3-6(a). With EDS, the surface of the analysis point and the subsurface components are detected, so Al is observed in all spectra in Figure 3-6(b)–(d).

As a result of the EDX spectroscopy analysis (Figure 3-6(b), Mn was detected along with Al and Si. Mn is added to cast Al alloys to limit the formation of brittle and needle-shaped Fe intermetallic compounds (β-Al_5FeSi) that adversely affect material properties [1,77,78]; Instead, Mn intermetallic compounds $Al_{12}(Fe,Mn)_3Si$ [79] or $Al_{15}(MnFe)_3Si_2$ [80] are formed. Mn intermetallic compounds are also brittle, but form polyhedral or star-like shapes. Image analysis showed that the volume fraction was < 1%.

In Figure 3-6(c), the analysis result of point 2, which is a Si particle, shows that only Al and Si were detected. Similarly, in the Al matrix, point 3, no components other than Al were detected.

4. Finite element simulation

4.1. Simulation conditions

Herein, the proposed model is designed to be influenced by probabilistic factors. The processes of distributing the void volume fraction and the Si particle size, and determining the crack of the Si particle are determined by probability. Therefore, each simulation integration point has a slightly different microstructure each time, and the fracture behavior of the material predicted by the simulation shows a scatter. Usually, the computational simulation of the mechanical behavior prediction is performed by applying a symmetric boundary condition to a 1/4 or 1/8 model of the specimens in Figure 3-2 (Figure 4-1). However, since the proposed model might show a different mechanical behavior depending on the specimen's position due to the microstructural distributions based on probability. Based on the viewpoint that fracture may occur in various parts of the specimen, the full model was used to predict the fracture. However, there was no significant difference in the results compared to the model to which the symmetric boundary condition was applied. Figure 4-1(a) shows the boundary conditions prescribed for the specimen in the XY plane. The X and Y directions are the width and longitudinal directions of the specimen, respectively. The symbols of symmetric boundary conditions are explained on the right side of the figure. The nodes located on a plane perpendicular to the X-direction where the symbol is located are restricted to only the X-direction movement. Symmetric boundary conditions in the Y and Z directions are similarly applied. Figure 4-

1(b) shows the boundary condition in the Z-direction, which is the thickness direction.

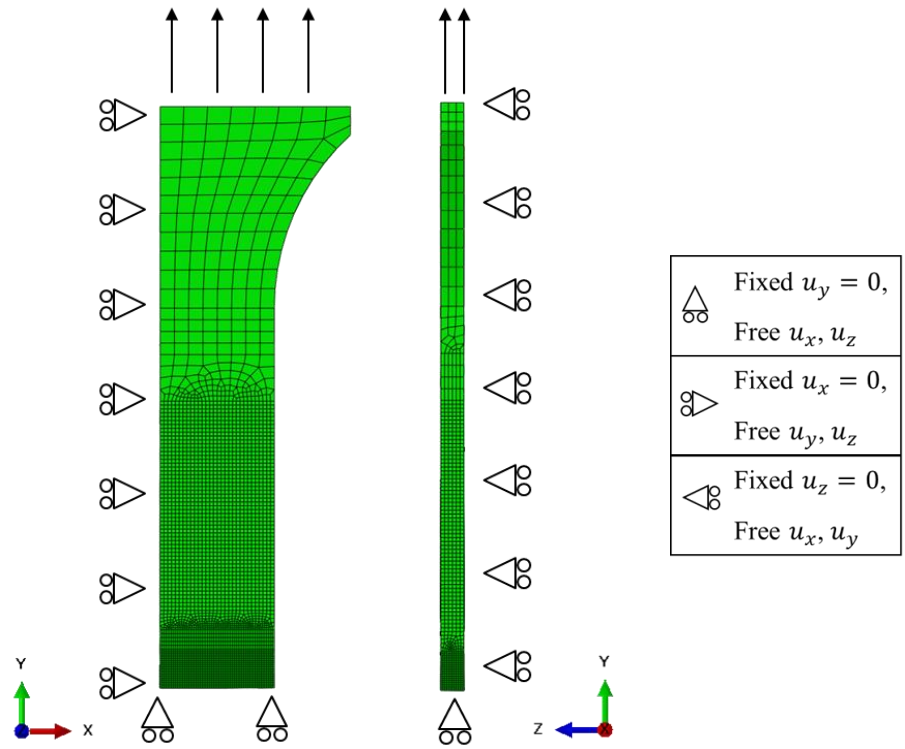

(a) (b)

Figure 4-1. Symmetric boundary conditions for 1/8 finite element (FE) model. In (a) X-Y (longitudinal-width) and (b) Z-Y (thickness-longitudinal) planes.

As mentioned in the previous subsection, ABAQUS/Standard with user material subroutine (UMAT) is used to execute the proposed model in an implicit scheme. The 3D brick element with a reduced integration point (C3D8R) was used. The size of elements used herein was determined after sensitivity analysis. Simple tension FE models for the element size sensitivity

analysis are shown in Figure 4-2. Figure 4-2(a) is a 1/8 model with a minimum element size of 50 μm placed in the region where the strain is concentrated and fracture is expected. Similarly, Figure 4-2(b) is a full model with a minimum of 100 μm mesh arranged. In the FE model in Figure 4-2 (c), most elements are 150 μm in size.

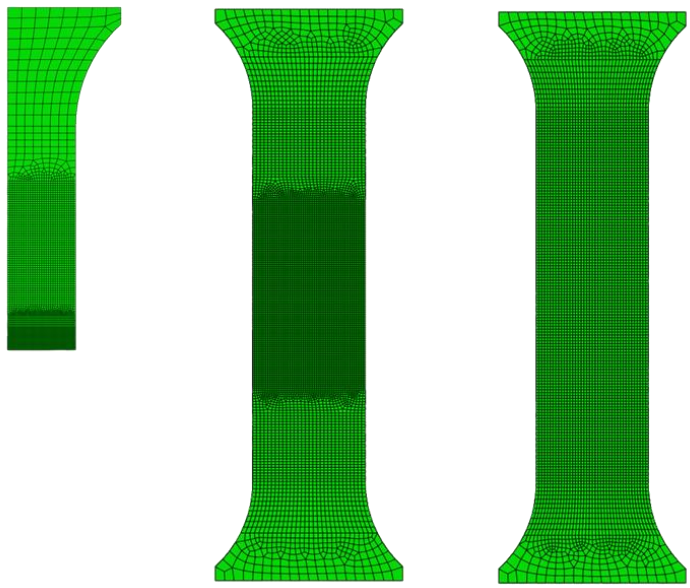

(a) (b) (c)

Figure 4-2. FE models of ST for element size sensitivity analysis. (a) 1/8 model with 50-μm minimum element size. (b) Full model with 100-μm minimum element size. (c) Full model with 150-μm element size.

The results of the element size sensitivity analysis are shown in Figure 4-3. The solid line of the force–displacement graph represents the superimposition of the tensile simulation results using (a), (b), and (c) in Figure 4-2, and they completely overlap each other. The box in Figure 4-3 represents the scattering

of the fracture displacement. The scatter in the simulation result using the FE model (a) of the element with the smallest size was the largest, but no significant difference exists between the scatter in the results of (b) and (c). It was concluded that it is meaningless to use a smaller element for computational efficiency.

The size of elements is consistent with the image analysis domain, which is 100 μm, and the size of minimum macrovoids using micro-CT, which is 50 μm.

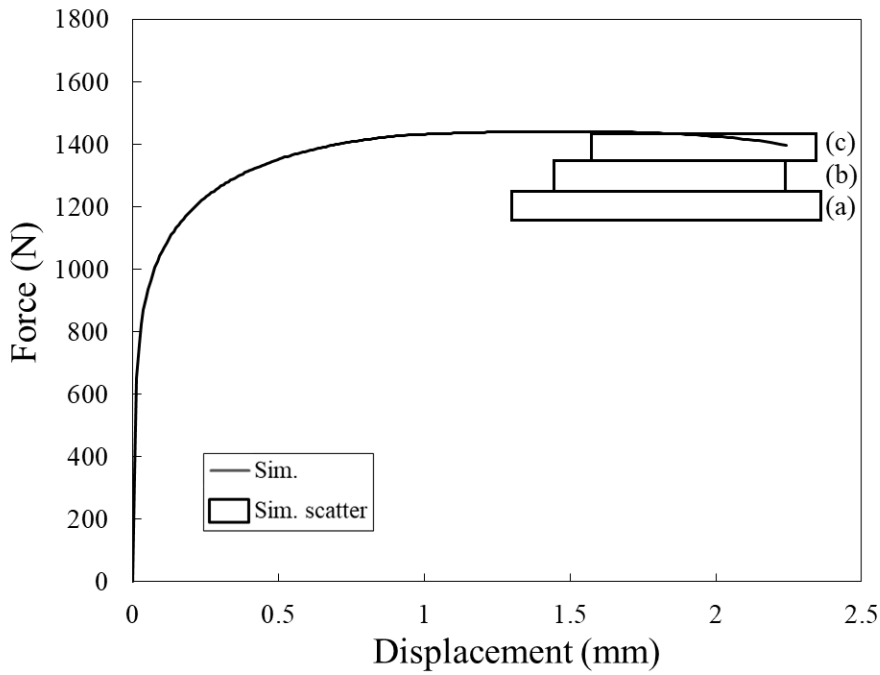

Figure 4-3. Force–displacement curves of element size sensitivity analysis.

4.2. Parameter identification

The fundamental idea for identifying the model parameters was based on a hybrid experimental-numerical approach as one of the inverse methods. To optimize the FE simulation parameters, the macrovoids' effect was excluded, and other effects by microvoids and Si particles were applied in a statistical manner.

For the basic mechanical properties, the elastic modulus and Poisson's ratio of the Al matrix and Si particles were obtained from the literature [13,36]. The Si particle was assumed to be a linear isotropic elastic material with a fracture at the principal critical stress. Since the pure plastic properties of the Al matrix cannot be readily determined due to the effect of the Si particles embedded in the Al matrix, an iterative method after applying the MT homogenization method to the microstructure of the Al alloy was employed. For the plasticity of the Al matrix, the isotropic yield was assumed, and the hardening was modeled by the combined Swift–Voce-hardening law.

$$\sigma = RK(\varepsilon_0 + e^p)^n + (1-R)\left[k_0 + Q\left\{1-\exp(-ce^p)\right\}\right] \tag{4.1}$$

where K, ε_0, and n are material parameters for the Swift-hardening part, and k_0, Q, c are those for the Voce-hardening part. Also, R is an additional model parameter controlling the relative contribution of each hardening behavior.

After assuming that the cracking of the Si particles is free in the early deformation stage, the hardening parameters of the Al matrix were determined iteratively by fitting the MT-coupled FE simulation result to the stress–strain curves of the ST test. The main target of the fitting was the range before 5%

strain, and if possible, an attempt was made to fit the hardening to the elongation limit after 5% strain. After obtaining the hardening parameters of the Al matrix, the flow curves were well-matched in the early deformation stage, where the damage of the Si particles is rarely observed. However, as the deformation increased, herein ~10% strain, the calculated flow stress overestimated the experimental flow curve. The resulting optimized parameters are presented in Table 4-1.

Table 4-1. Elastic and plastic parameters of Si particle and Al matrix.

E_{Al} (GPa)	ν_{Al}	E_{Si} (GPa)	ν_{Si}
70	0.3	169	0.262
R	K (MPa)	ε_0 (10^{-4})	n
0.7965	324.7	2.122	0.157
	k_0 (MPa)	Q (MPa)	c
	85.66	49.27	33.7

Next, the Weibull distribution and GTN parameters were adjusted by fitting the flow curves under different stress states. Here, the load–displacement curves of the CH, NT, and shear specimens presented in Figure 3-6(b)–(d) were fitted by iteratively changing the parameters. Due to the influence of the Si particle cracks based on probability, different fracture behaviors are shown

for each trial, even if the simulation is performed based on the same parameter set. Therefore, at least five simulations should be performed with the same set of parameters during the identification procedure.

The GTN parameters q_1 and q_2 were adopted from Tvergaard's study [63], and q_4 has a value of 1/3 in the 3D model. V_0, one of the Weibull parameters, was set to 1.53 μm^3 of the average volume of the Si particles obtained through the image analysis, as the work of Caceres and Griffiths [76], and the remaining parameters were found. The identified Weibull and GTN parameters are listed in Table 4-2 and 4-3, respectively.

Table 4-2. Weibull parameters.

V_0 [μm^3]	σ_f [MPa]	m
1.53	845	2

Table 4-3. GTN parameters.

q_1	q_2	q_3	q_4	f_c	f_f
1.5	1.0	3.72 x 0.9	1/3	0.02	0.08

In the literature, direct identification methods exist based on experiments for the Weibull distribution parameters [72–76]. However, herein, the Weibull

parameters were also determined by fitting. The Weibull parameter value is smaller than that of previous studies because the assumptions applied herein are different from those of previous studies. Contrary to the MT method used herein, Caceres and Griffiths [76] and Brechet *et al.* [75] estimated the stress of elastic inclusions based on the studies by Brown [81], Brown and Clarke [82], and Brown and Stobbs [83,84]. They also obtained the Weibull parameter σ_f by multiplying the particle's stress by the aspect ratio [75,76]. However, herein, its parameters were determined by comparing the simulated and measured overall mechanical responses by calibrating the parameters as inverse schemes. Note that the identified Weibull parameters herein did not much deviate from those of the previous studies. Herein, the mean aspect ratio of the Si particles was determined as ~1.67. Using their method, σ_f would be 1411 MPa.

The GTN parameters identified herein were also obtained by the FE inverse analysis. In some literature, GTN parameters, such as f_N, f_c, and f_f, were identified through microstructural analysis. Min *et al.* [81] considered that voids could be nucleated from secondary particles, and based on their fraction, the f_N value can be determined, a parameter related to the potential fraction of void nucleation. The parameters, void fractions of coalescence and failure can also be defined experimentally, or with the FE inverse method as performed herein. The GTN parameters f_c and f_f of steel and Al alloys proposed by experimental and FE inverse analysis in previous studies are listed in Table 4-4. Even though such studies dwelt on the same material, different researchers have different GTN parameters, and the parameter

deviation of steel exceeds that of Al alloy. Herein, the GNT parameters f_c and f_f were identified as 0.02 and 0.08, respectively, and were determined at a reasonable level because they had similar values to the Al parameter values of previous studies.

Table 4-4. GTN parameters in previous works.

f_c	f_f	Material [Ref]	f_c	f_f	Material [Ref]
0.03	0.048	Al5052 [85]	0.0134	0.0216	IF steel [93]
0.005	0.07	AA5182 [86]	0.08	0.12	Mild steel [94]
0.02	0.04	3A21-O [87]	0.002	0.0024	High C steel [95]
0.014	0.1	AA6060 [88]	0.028	0.09	DP600 [96]
0.035	0.063	AA6061-T4 [88]	0.013	0.207	DP780 [97]
0.05	0.15	AA6016-T4 [89]	0.11	0.156	SUS304 [98]
0.013	0.04	AA6061-T6 [90]	0.0135	0.2628	SS304 [99]
0.087	0.14	AA6061-T6 [91]	0.11	0.25	SS304 [100]
0.014–0.045	0.1–0.15	AA7075 [92] (300℃)	0.003	0.18	API X65 [101]
			0.015	0.25	

Simulation results using the model parameters identified in Tables 4-1, 4-2, and 4-3 are shown in Figure 4-4 along with the experimental results. In the experiments, the fracture strain scattering is indicated by an elongated empty box. In the simulation, the macrovoids' effect was also considered by distributing a 0.01% macrovoid volume fraction. The figure shows that the simulated flow curves are well-matched with all experimental flow curves

under different loading conditions, which validates the accuracy of the identified parameters of the proposed microstructure-based homogenized fracture modeling.

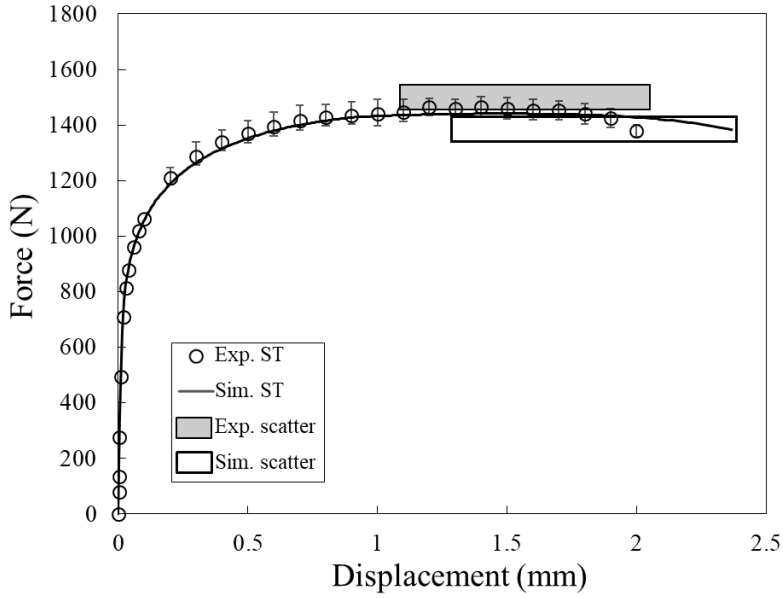

(a)

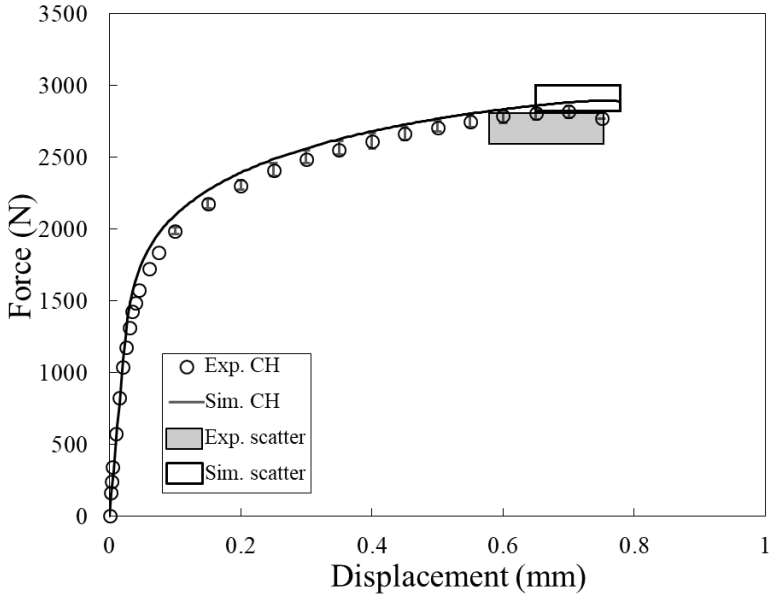

(b)

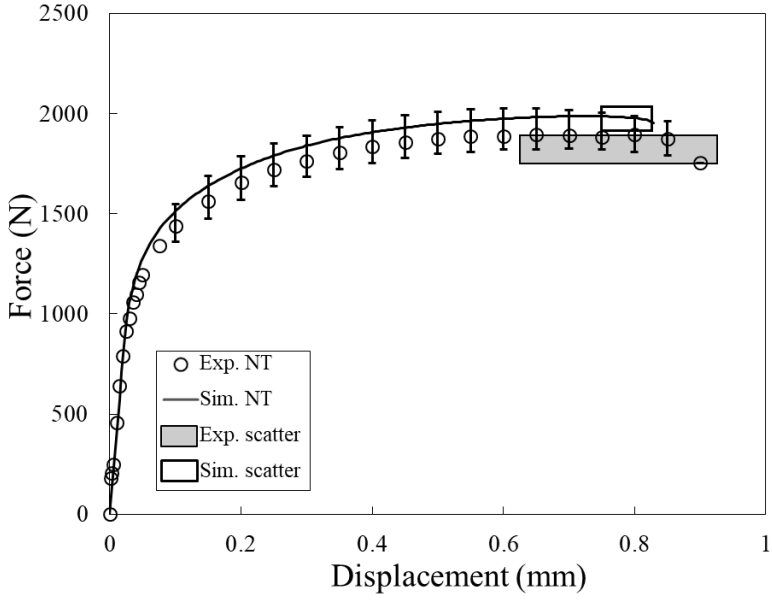

(c)

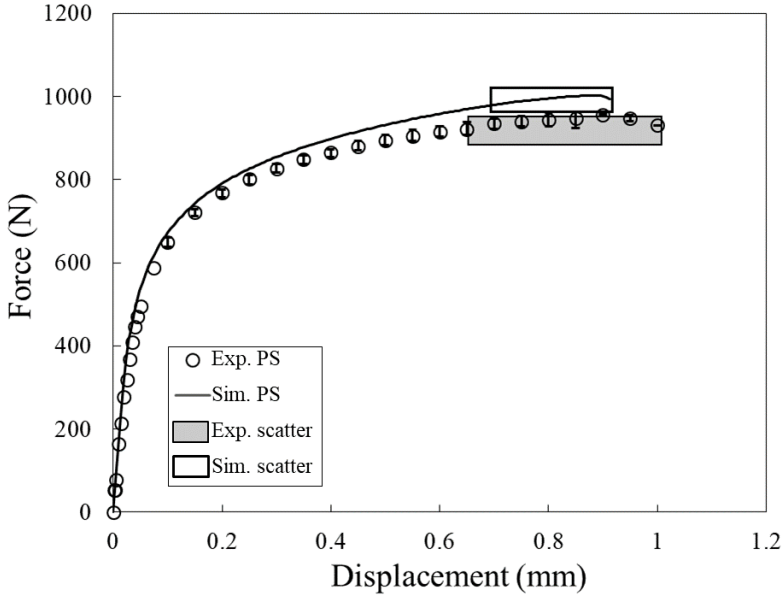

(d)

Figure 4-4. Force–displacement curves of both experiments and simulations with (a) ST, (b) CH, (c) NT, and (d) PS.

In Figure 4-5, the onset of fracture was determined by counting the number of damaged elements, which represented rapid increase once the damage propagates abruptly. The points of the fracture strains are indicated in Figure 4-5.

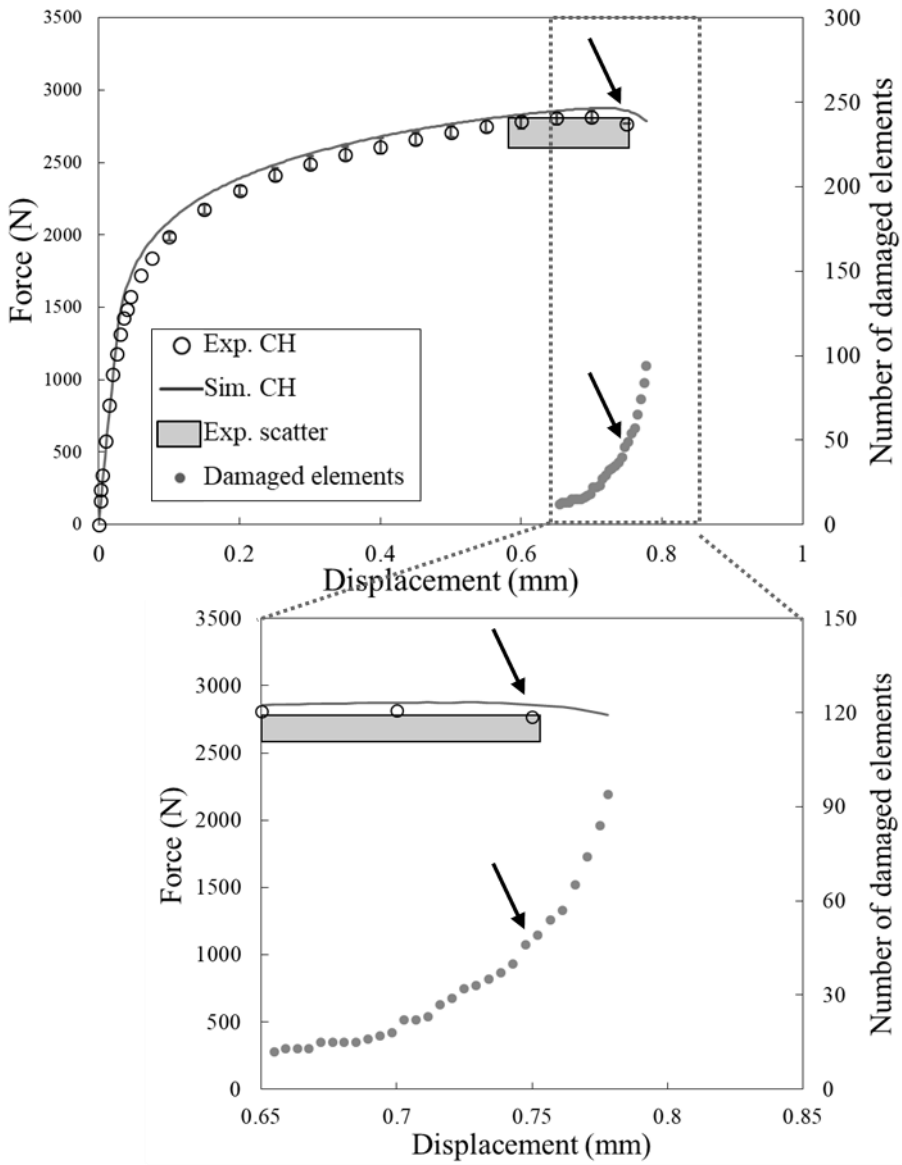

(a)

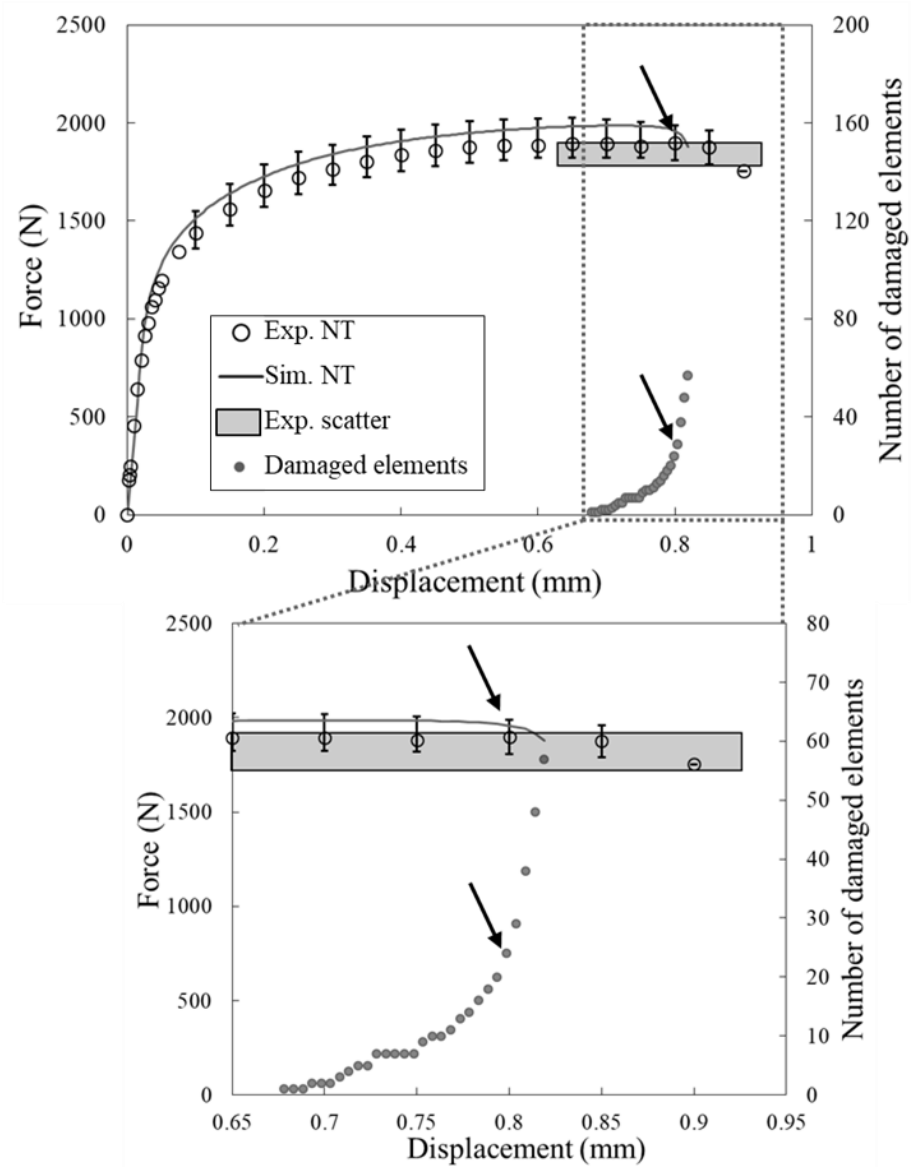

(b)

Figure 4-5. Force–displacement curves with several damaged elements of (a) CH and (b) NT simulation.

4.3. Model validation

In Section 4.2, it was shown that the proposed microstructure-based probabilistic mean-field FE model could well capture both the experimentally measured plastic behavior and fracture strains with scatters for the investigated loading cases (Figure 4-4). Also, the correlations between the experiments and modeling justify the model parameter identification procedure.

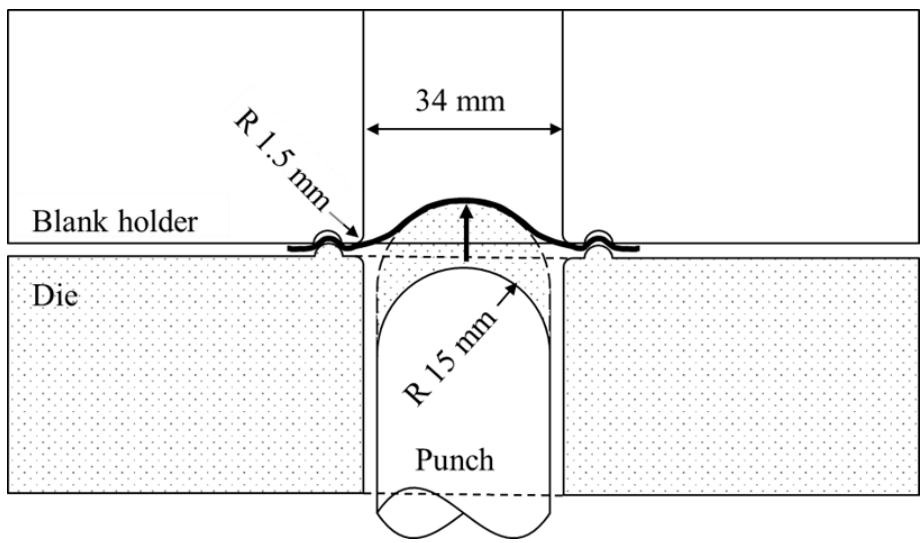

(a)

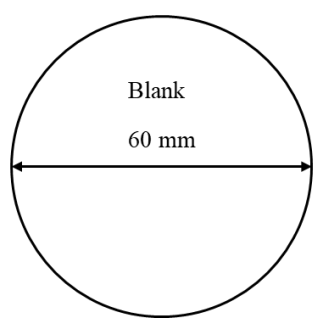

(b)

Figure 4-6. (a) Schematics of limiting dome height (LDH) test and (b) LDH test specimen.

To further validate the developed FE model, two more simulations were conducted, and their load–displacement curves and fracture points were compared with that of the experiments. The two test conditions are a U-notch specimen subjected to the plane strain deformation and a limiting dome height (LDH) test subjected to the balanced biaxial deformation. A schematic of the LDH test with a 15-mm punch radius is shown in Figure 4-6(a). The shape and dimension of the test specimens are shown in Figures 3-6(e) and 4-6(b). The stress triaxialities of the two test conditions range between 0.5 and 0.66. Therefore, the validation is designed to check if the developed model and its material parameters work well for the deformation with rather higher stress triaxiality. Figure 4-7(a) and (b) show the force–displacement curves of the plane strain and balanced biaxial modes, respectively, indicating that the developed model could well predict the plastic deformation and the fracture onset within reasonable accuracy when compared to those of the experiments. The result also shows that the flow curve of the plane strain (or U-notch tension) mode rather overestimates the experimental flow curve. This trend may be attributed to the isotropic yield function used for the basis of the GTN model. It has been reported that Al alloys can be better described with non-quadratic yield functions, which represent the sharp corners between the balanced biaxial and uniaxial tension [102–104]. Therefore, the flow stress under the plane strain condition decreases, and the fracture is rather faster due to the earlier localization at large plastic deformations. However, even with the simple isotropic (quadratic) yield function employed herein could capture the main characteristics of the flow stress and ductile fracture at a wide range of

stress triaxiality.

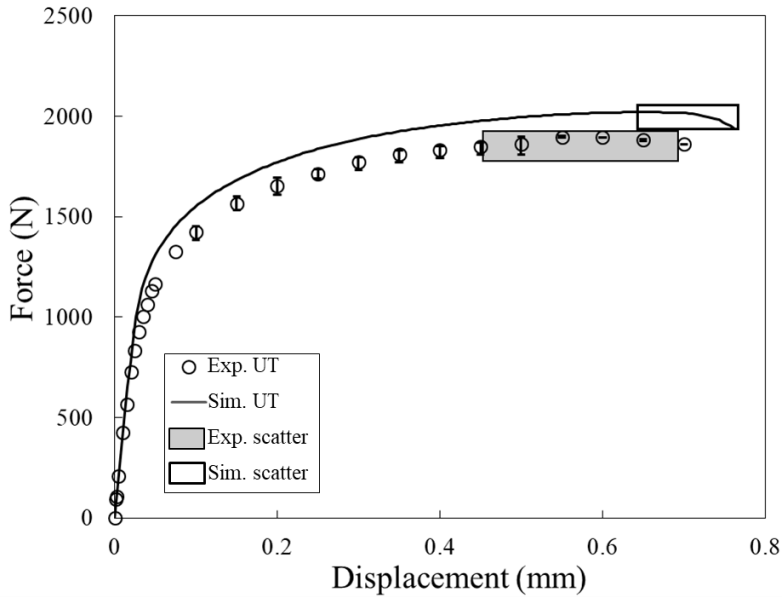

(a)

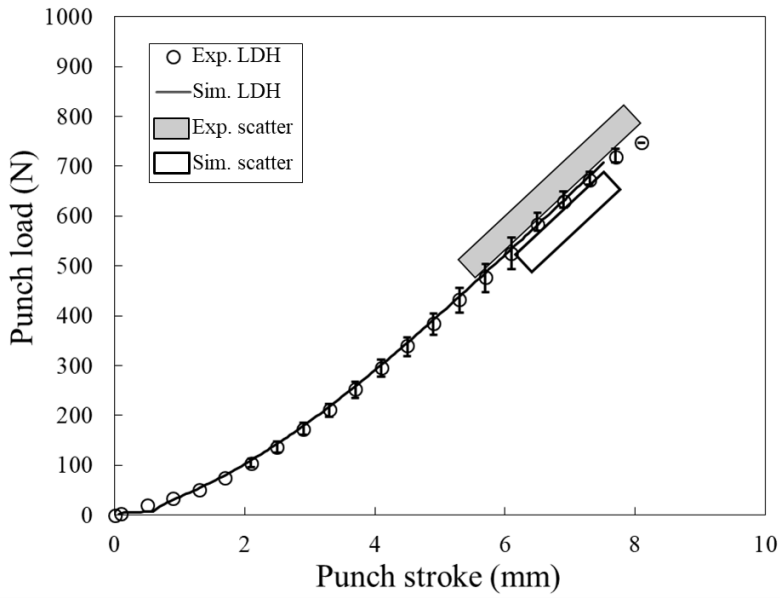

(b)

Figure 4-7. Force–displacement curves of both experiments and simulations with (a) UT and (b) LDH.

5. Discussion

5.1. Mechanism of void nucleation

It is well-known that voids in cast Al alloys mainly appear as Si particle cracks, but debonding of the matrix and particle interface can also be affected, so the void nucleation mechanism should be observed. The scanning electron microscopy (SEM) image in Figure 5-1 (a) was obtained from the adjacent region of the fracture. Due to the strain concentration near the fracture surface, a significant number of cracks occurred and are easily observed. The cracks formed in the Si particles are indicated by white arrows.

In contrast, Figure 5-1(b) shows voids that are difficult to distinguish in what way they were created. Figure 5-1(b) is an SEM image obtained from a region with an average strain of ~0.1 away from the fracture location, and voids are indicated by white arrows. It is meaningless to distinguish the generation method of voids because the number and size of voids are small. Besides, it is difficult to find a factor that can cause damage propagation. However, in Figure 5-1(a), where the strain is concentrated, the voids caused by cracks in Si particles are overwhelmingly observed. Therefore, it was concluded that it is reasonable to calculate the damage evolution of the cast Al alloy considering only the cracks of the Si particles, without considering the generation of voids by debonding.

Figure 5-1(c) is an enlarged image of the cracked Si particle indicated by the white arrow in Figure 5-1(a). The cracks occurred in relatively large particles, which is consistent with the description in Weibull statics. The width of the

lower crack of the Si particle is 0.5 μm and is twice the width of the upper crack. If the deformation was continued in this part, it could be assumed that the crack propagated in the downward direction of the image.

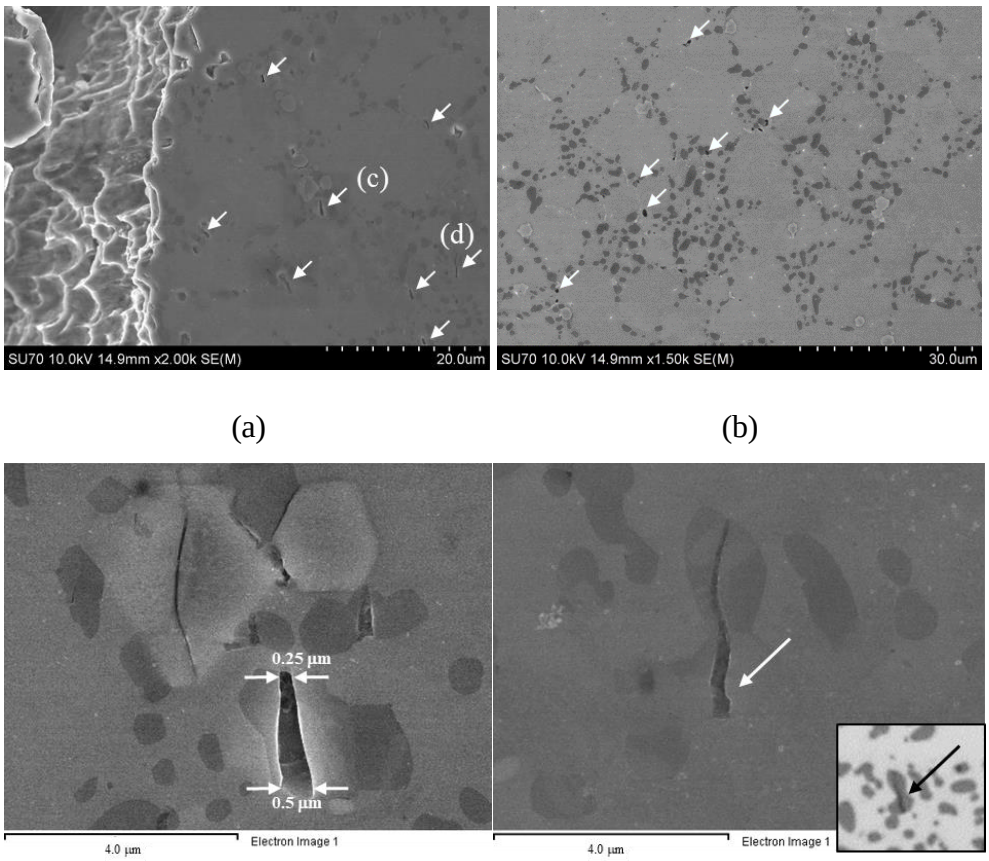

Figure 5-1. SEM images. (a) Near the fracture region and (b) in the region with an average strain of 10% far from (a). (c and d) Magnified images from (a).

In Figure 5-1(d), cracks were also found in relatively large Si particles. The cracks indicated by the white arrows in the SEM image appear to have

propagated to the Al matrix, but are actually cracks that only occurred inside the Si particles. It can be clearly seen by observing the optical microscopy image inserted at the bottom right of Figure 5-1(d). In Figure 5-1(d), the width of the lower part of the crack is wider than that of the upper part as shown in Figure 5-1(c). This phenomenon indirectly proves that the main factor of damage propagation is the Si particle crack

5.2. Effect of macroscopic voids on ductile fracture

The calculated flow stresses and fracture strains under various stress states could well predict those of the experiments within reasonable accuracy. However, deviations still exist from the measurements, particularly the fracture strains (or displacements). One of the possible causes for this discrepancy may be attributed to the macroscopic voids and their distribution in the specimens. Note that the macrovoids are often introduced as artifacts during the inappropriately controlled casting processes. Also, the size of macrovoids and distributions are noncontrollable, and they are generally non-uniform.

The measured size and volume fraction of macrovoids are ~50–300 μm and 0.01%, respectively. In the simulation, the macrovoids effect cannot be easily investigated, and the statistical analysis on their size and distribution is challenging because the number of material (or integration) points in the simulation is limited. Note that other defects, such as microvoids and Si particle cracking, can be implemented with a probabilistic approach, whereas the macrovoids should be considered by allocating them directly in the FE model.

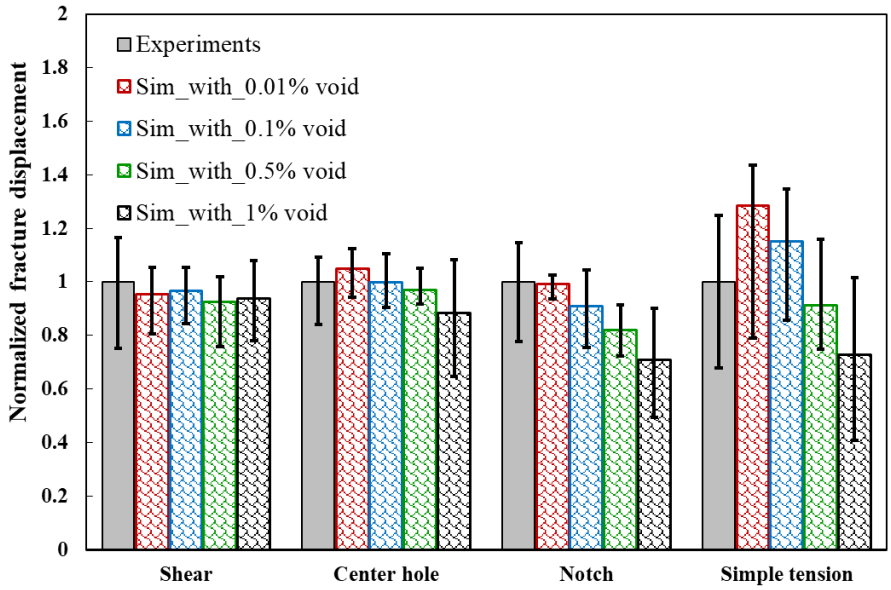

(a)

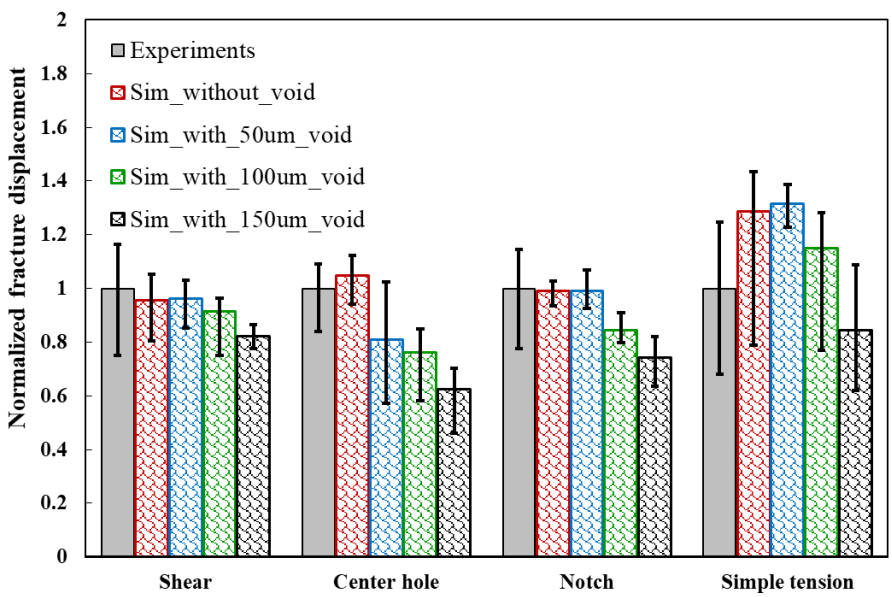

(b)

Figure 5-2. Normalized fracture displacement based on effects of (a) volume fraction of macrovoids and (b) distribution of macrovoids.

Therefore, the macrovoid effect was further investigated by analyzing the volume fraction and critical location of the macrovoids. For this purpose, first, the macrovoids were statistically distributed with different volume fractions on the four test specimens, i.e., PS, CH, NT, and ST specimens. Figure 5-2(a) shows the fracture strains (or displacements) with different macrovoid volume fractions. The fractured displacements were normalized by the experimental-averaged values. The results clarify that the fracture strains decrease as the volume fraction of the macrovoids increases, which is readily expected. However, the magnitude of the fracture strain reduction was still marginal even when the factor of the increased volume fraction was significant. That is, the averaged fracture strains were reduced ~20% when the volume fraction of the macrovoids increased by 100 times.

As another effect of the macrovoids on the mechanical and ductile fracture of the Al alloy, the location of macrovoids was investigated. The analysis is motivated by the fact that the macrovoids can be located unexpectedly near the critical deformation, where the fracture initaition is most anticipated. For this, the three different radii of macrovoids, 50, 100, and 150 μm, were intentionally placed at the critical location of the fracture. Note that the volume fractions of the macrovoids with three different sizes are < 0.01%, which was similar to the measured volume fraction. Figure 5-2(b) shows that the reduced fracture strains were more pronounced than the reduction by changing the volume fraction. Thus, the effect of macrovoids located at the critical fracture site is similar to the case where the volume fraction increased 100 times.

The above analysis clarifies that the macrovoids (or processing artifacts) introduced during the casting process should be carefully controlled not to be located near the critical fracture initiation sites.

5.3. Detailed analysis of fracture evolution

The mechanical properties of typical ductile metals are generally uniform enough due to their (nearly) homogeneous microstructures, leading to manageable scatters in the fracture strains. Therefore, the continuum-based ductile fracture models, such as Mohr-Coulomb [105,106] as an uncoupled plasticity-ductile fracture criterion and the GTN model [14-17] as a coupled plasticity-fracture model, can be employed. The mathematical formulations of these models were proposed based on the observation that the ductile fracture can be a function of the stress state, especially the hydrostatic stress and material hardening, but the material inhomogeneity effect was not directly included. Thus, the damage evolution of a material point is similar to that of the material point in a very close neighborhood because the stress states of the material points (or FEs) during the simulation are virtually the same.

For the detailed analysis of the damage evolution behavior under the developed probabilistic fracture model, the individual damage behavior of a few elements was monitored in relation to the stress state, void volume fraction, and material strength (in terms of the equivalent stress) from Figures 5-3, 5-5, and 5-6. Both the stress states and strength of the Al matrix and Al alloy (homogenized) were analyzed in Figures 5-6 and 5-7 using a ST specimen (Figure 5-6) and other specimens with various averaged stress

triaxiality (Figure 5-7).

Figure 5-3 shows the contour of the damage value of the ST specimen, in which the coordinates X, Y, and Z represent the width, loading, and thickness directions, respectively. Figure 5-3(b)–(f) show the locally damaged FEs in the magnified area [in the red box of Figure 5-3(a)], where the red color denotes that the element lost the load-carrying capacity or the damage value reached 1. The corresponding force–displacement curve during ST is also shown in Figure 5-5. Note that the different strain levels indicated by vertical dot lines correspond to the deformation stages of Figure 5-3(b)–(f).

As a first observation from Figure 5-3, the fracture onset is not the specimen's center, which has often been predicted using the conventional ductile fracture model. This observation occurs because the plastic strain or major stress is mostly highest at the specimen's center. However, the fracture location initiation is predicted considering the microstructure, which comprises the distribution of Si particles in the Al matrix. In this simulation case, the damage was initiated regions away from the specimen's center, especially marked with a red box.

The maximum logarithmic strain contour of Figure 5-3 is shown in Figure 5-4(a). Figure 5-4(b) shows one of the test results with the maximum logarithmic strain contour. The fracture onset in the simple tensile test did not occur centrally, similar to the simulation results in Figures 5-3 and 5-4(a). As described herein, the size of Si particles and the fraction of microvoids are determined probabilistically. Without any adjustment, the simulation outcome showed almost the same mechanical behavior as the experiment. The contour

levels are set the same for easy comparison of Figure 5-4(a) and (b). The strain fields of both figures are almost identical.

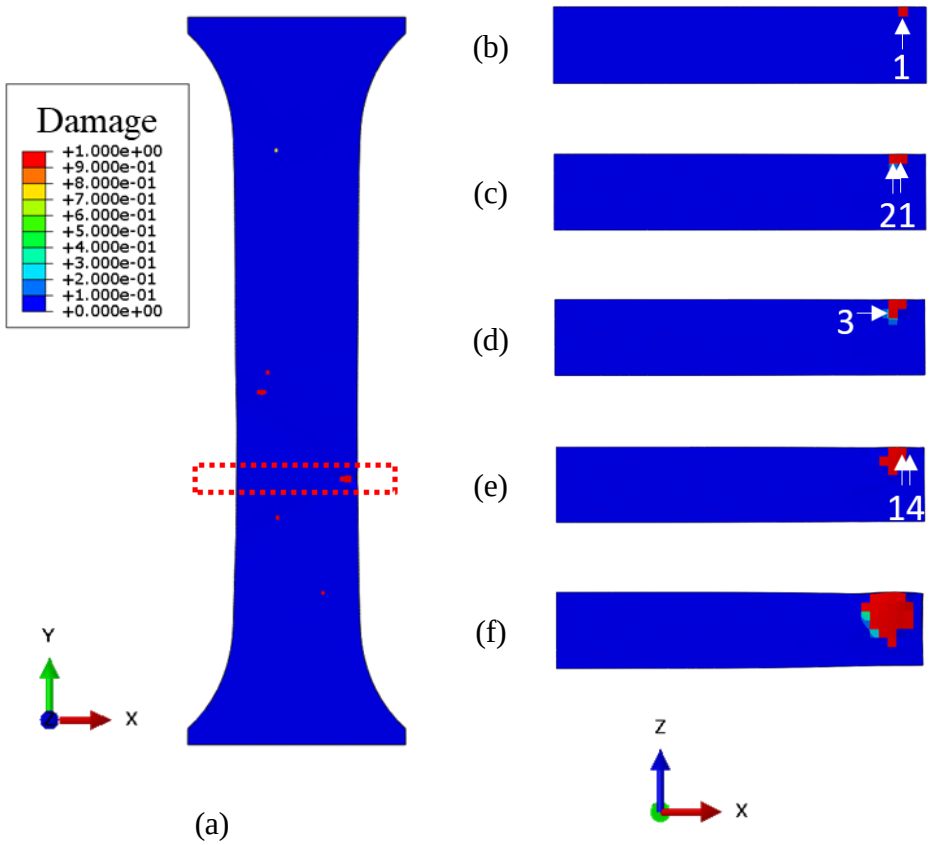

Figure 5-3. Damage contour of simple tension simulation in (a) in X–Y plane. (b)–(f) Damage propagation in Z–X plane listed in chronological order.

In Figure 5-3(b), element 1 first lost the load-carrying capacity (with a damage value of 1). Subsequently, as shown in Figure 5-3(c) and (d), elements 2 and 3 lost their strength. The strain required to initiate the damage in element 2 after the failure of element 1 was delayed significantly instead of successive damage propagation. Figure 5-5 shows the larger displacement (or strain) gap

between the two vertical lines (a) and (b). This result is attributed to the local stress relaxation of the neighborhood element when the nearby element lost its load-carrying capacity completely. For the damage propagation to proceed in the neighboring elements, more deformation needs to be accumulated [Figure 5-3(d)–(f)]. Note that the damage value of element 4 in Figure 5-3 did not increase until the end of the simulation, even when it was located near the same area. Based on this analysis, it was reasonable that the fracture onset in the specimen was determined when the number of damaged elements abruptly increased as the vertical line (e) in Figure 5-5.

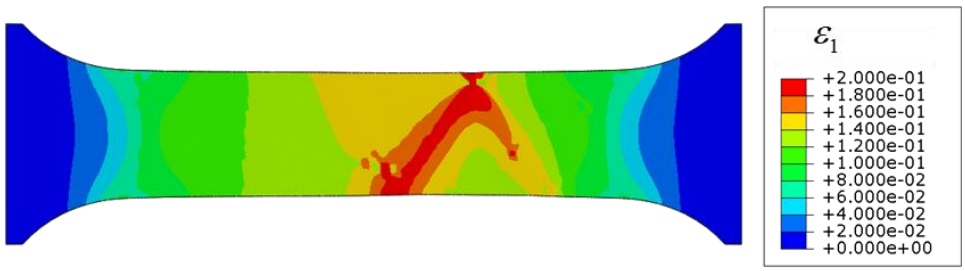

(a)

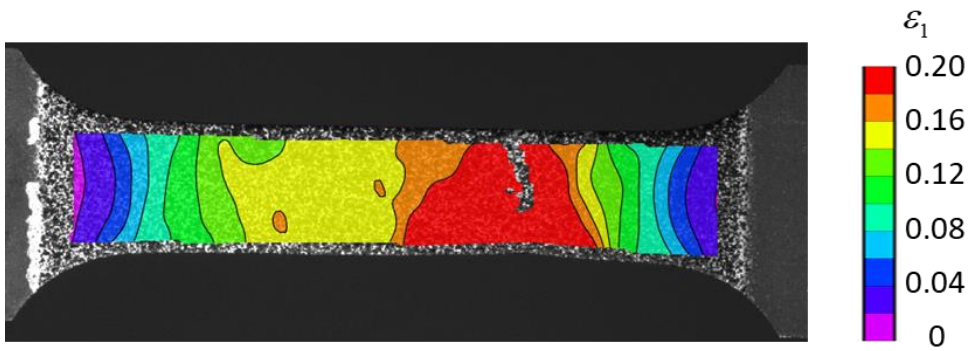

(b)

Figure 5-4. Logarithmic strain contour of (a) simulation and (b) test with DIC.

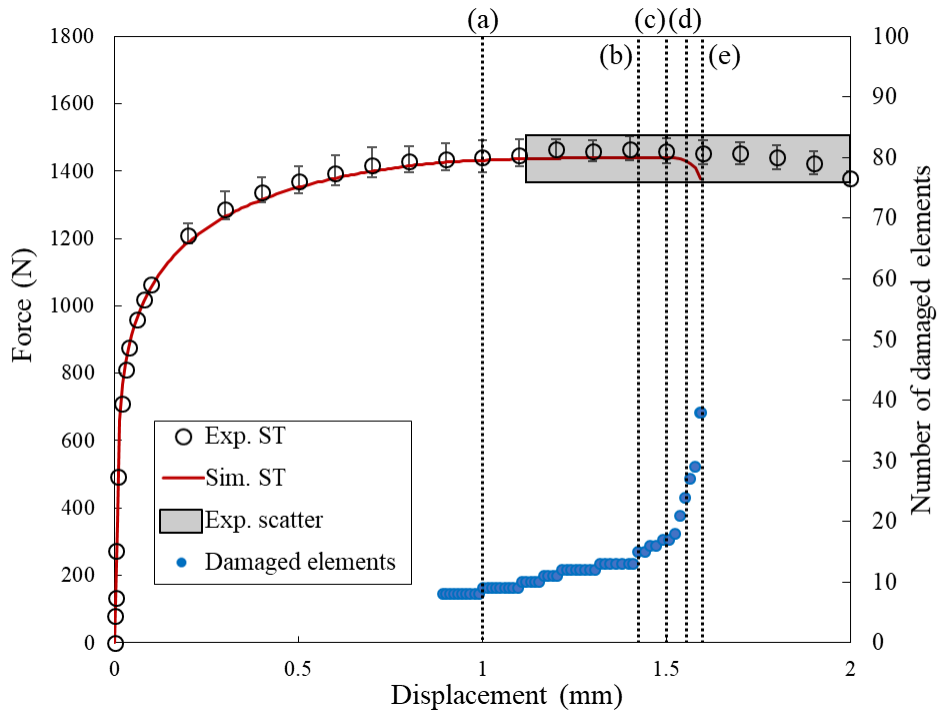

Figure 5-5. Force–displacement curves with several damaged elements of ST simulation of Fig 5-3. Dotted lines (a)–(e) correspond to (b)–(f) of Figure 5-3, respectively.

More detailed analyses are provided in Figure 5-6, in which the stress triaxiality, damage value, and void fraction were monitored for elements 1–4 in Figure 5-3(b)–(f). For the stress equivalent stress (black) and stress triaxiality (red), the dotted and solid lines denote the values of the Al matrix and the homogenized Al alloy, respectively. In the figure, the vertical dotted lines (a)–(e) also represent the deformation stages indicated in Figures 5-3 and 5-5).

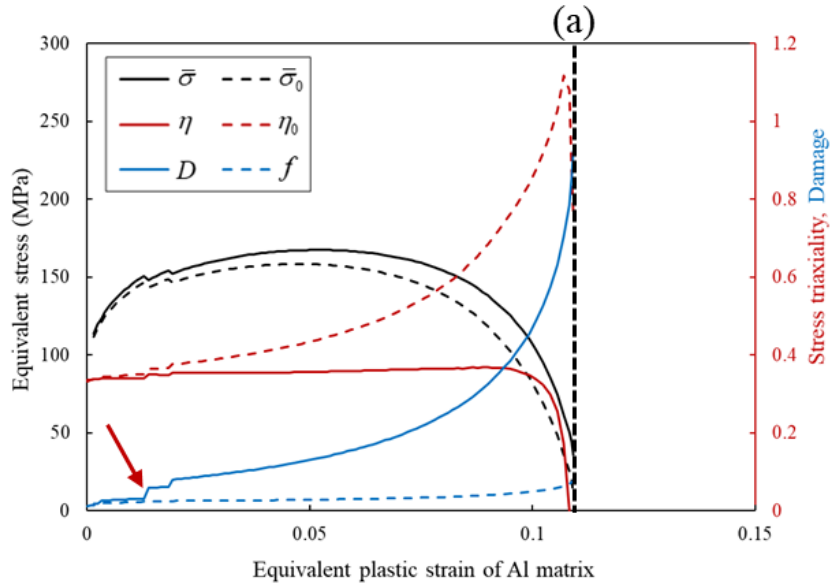
(a)
$\bar{\sigma}$
$\bar{\sigma}_0$
η
η_0
D
f
Equivalent stress (MPa)
Stress triaxiality, Damage
Equivalent plastic strain of Al matrix
0
50
100
150
200
250
300
0.2
0.4
0.6
0.8
1
1.2
0.05
0.1
0.15

(a)

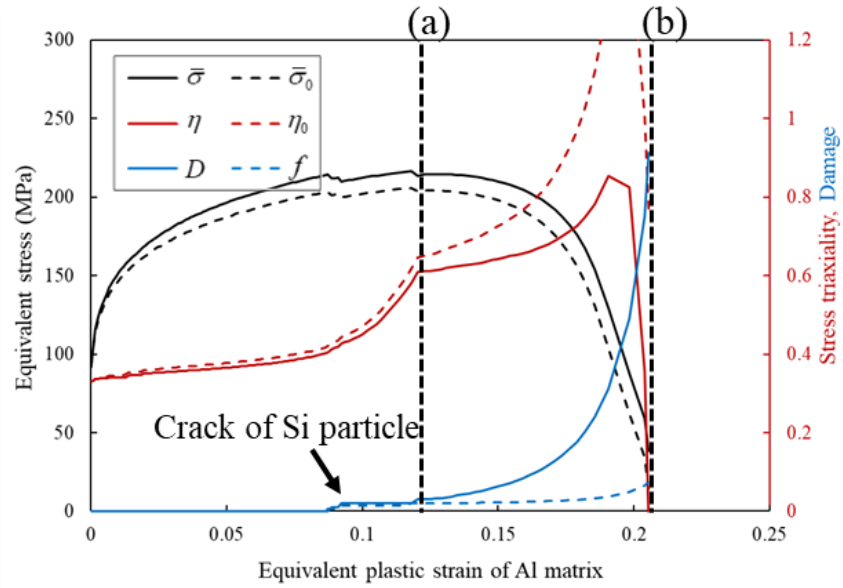
(a)
(b)
$\bar{\sigma}$
$\bar{\sigma}_0$
η
η_0
D
f
Crack of Si particle
Equivalent stress (MPa)
Stress triaxiality, Damage
Equivalent plastic strain of Al matrix
0
50
100
150
200
250
300
0.2
0.4
0.6
0.8
1
1.2
0.05
0.1
0.15
0.2
0.25

(b)

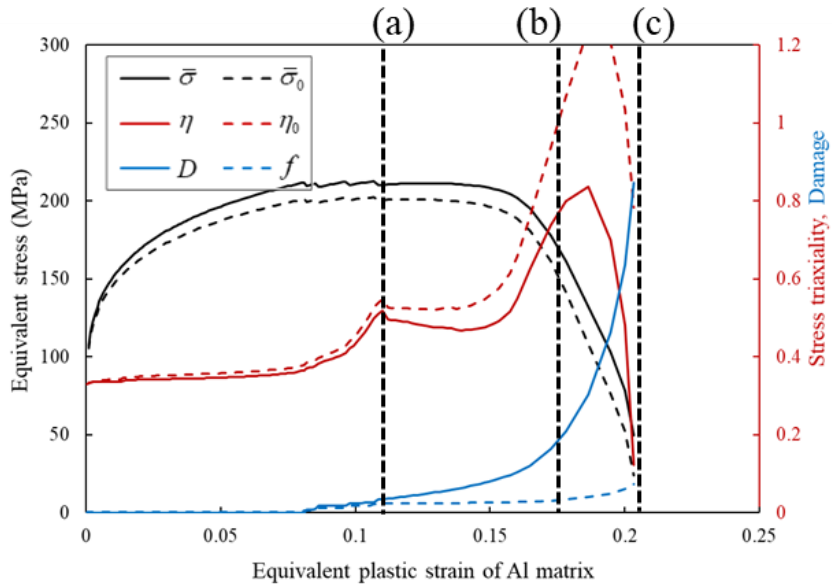

(c)

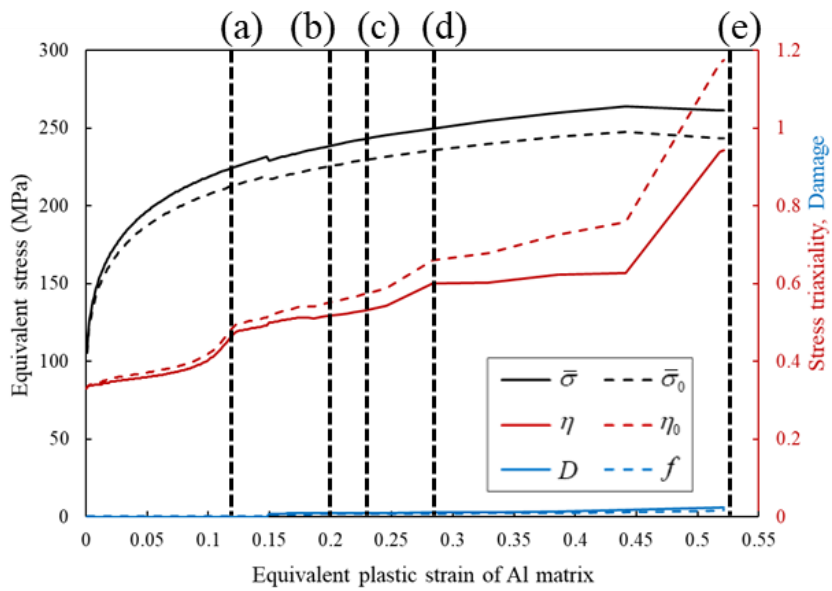

(d)

Figure 5-6. Equivalent stress, stress triaxiality, and damage-strain curves for material points of (a) 1, (b) 2, (c) 3, and (d) 4 in Figure 5-3. Dotted lines (a)–(e) correspond to (b)–(f) of Figure 5-3 and (a)–(e) of Figure 5-5.

Figure 5-6(a) shows that the void fraction was increased to 1% even before the plastic deformation of the Al matrix because of the cracking of the Si particles. The continuous cracking of the Si particles resulted in the void volume fraction exceeding f_c; thus, the damage accumulation was accelerated before the strain and is indicated by a red arrow. The cracking of the Si particles also occurred at the arrow point, and the damage increment was much larger, according to Eq. (2.45). The cracking of the Si particles could also be verified by the fact that the stress drops due to the decrease in the fraction of Si particles (and stress relief by the loss of the load-carrying capacity of the cracked Si particles).

In the process of strain partitioning to the Si particles and the Al matrix by the Mori‐Tanaka (MT) mean-field method, the strain was more concentrated in the Al matrix, in which the strength was lowered due to the void fraction increment (induced by Si particle cracking). As a result, the stress triaxiality of the Al matrix began increasing, and the damage of the Al matrix increased rapidly. Eventually, the void fraction reached the failure fraction f_f, or the damage value satisfied 1.0 at a strain value of 0.11.

For element 2 [Figure 5-3(b)], the cracking of the Si particles was observed after plastic deformation. At the failure point of element 1 [vertical dotted line (a)], the stress triaxiality continuously increased [Figure 5-6(b)]. As the load-carrying capacity of element 1 decreased, the load was partitioned to element 2, which was indicated by the stress triaxiality increment. For element 3, the stress triaxiality increased due to the strain partitioning after the increment in the damage of elements 1 and 2. However, after the fracture of element 1, it

was observed that the stress triaxiality increment of element 3 was less than that of element 2. This trend indicates that the strain (or load) partitioning after the fracture of an element is differently distributed depending on the location from the critical element. For element 4, no failure was predicted, unlike the other three elements in the neighborhood. This trend occurred because the voids generated by the cracking of the Si particles were sufficiently small, and the damage did not increase even with an increase in the stress triaxiality. The reduced cracking of the Si particles is mainly attributed to the significant loss of strength (or stress relief) in the nearby elements 1, 2, and 3.

From Figures 5-5 and 5-6, the propagation of damage through the specimen could be well understood. When only element 1 failed, the load was evenly distributed to the surrounding elements; thus, the damage propagation was marginally slow. However, after element 2 lost its strength, deformation was more locally concentrated in the area, and the damage propagated rapidly. The strain concentration can also be seen in Figure 5-6(d). In Figure 5-5, the displacement between the dashed lines (d) and (e) is only ~0.05, while the equivalent plastic strain of element 4 increased by 0.25.

To investigate the effect of the stress state (or deformation mode) on the damage evolution, similar analyses were provided for the specimens of the center hole (CH), notch tension (NT), limiting dome height (LDH), and in-PS. Figure 5-7 shows the equivalent stress, stress triaxiality, and damage value as functions of the equivalent plastic strain of the Al matrix. All data shown in Figure 5-7(a)–(d) were extracted from the elements, where the first failure was detected during the simulation of each specimen. Note that the specimens with

a CH, NT, and LDH represent the deformation with stress triaxialities > 0.33. Under these modes, the damage started by accumulating the Si particle cracking, like the ST case (Figure 5-5).

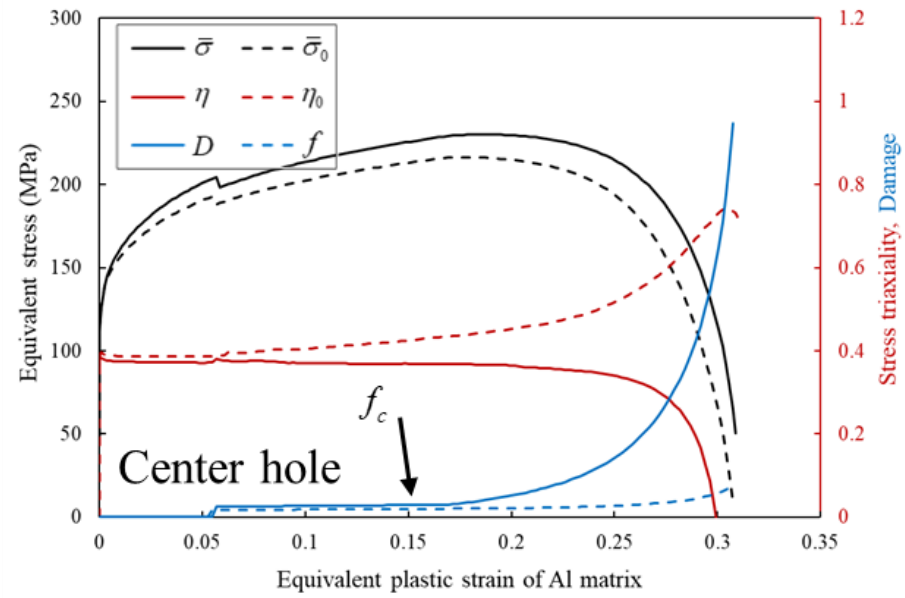

(a)

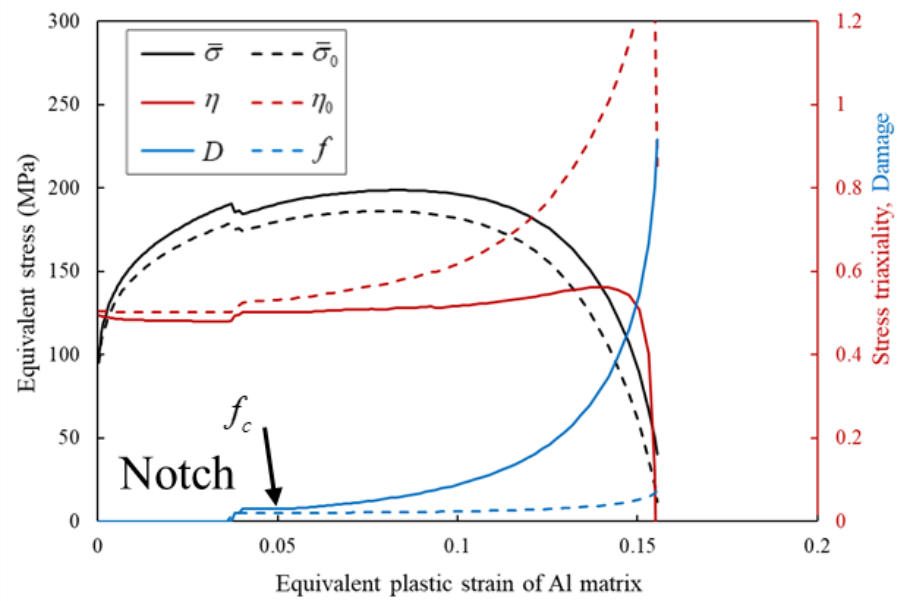

(b)

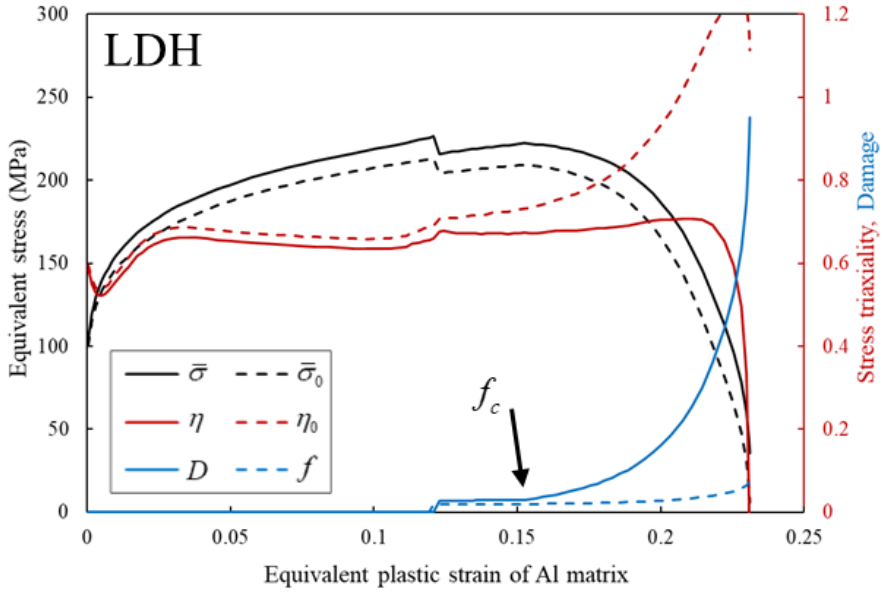

(c)

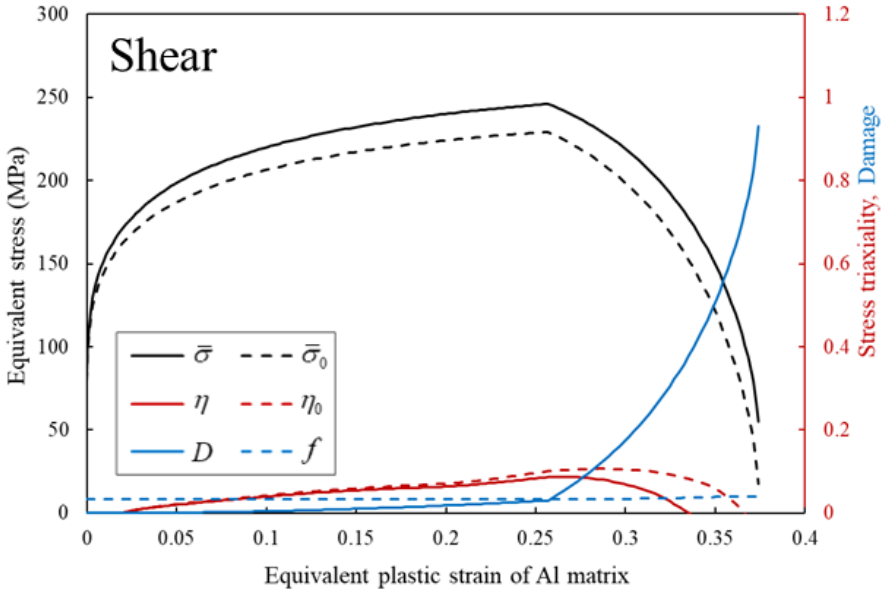

(d)

Figure 5-7. Equivalent stress, stress triaxiality, and damage-strain curves of fracture initiation material point of (a) CH, (b) NT, (c) LDH, and (d) PS simulation.

Using the simulation, the equivalent plastic strains of the homogenized Al phase were predicted for the CH, NT, and LDH specimens. First, the strains corresponding to the critical coalescence void fraction (f_c) were 0.16, 0.05, and 0.15, respectively, for the three specimens (marked with black arrows in Figure 5-6). Also, the equivalent plastic strains where the specimens showed final fracture were 0.31, 0.15, and 0.23, respectively. Therefore, the differences between the two points, i.e., between the final fracture and the initiation of void coalescence, can be regarded as the damage evolution speed, which are 0.15, 0.1, and 0.08 for the CH, NT, and NT LDH, respectively. As commonly expected, the damage evolution was fastest for the LDH specimen, where the major deformation mode is the balanced biaxial stress with the largest stress triaxiality.

Contrary to the other specimen, the damage evolution of the shear specimen is mainly controlled by the void shearing without significant evolution of the void fraction [Eq. (2.58)].

An important finding is that the number of cracked particles is not always proportional to strain magnitude. That is, the number of cracked particles was less predicted even with a very highly strained region because the Si particle cracking is selectively determined based on the Weibull distribution function, in which the large-sized Si particles crack first. For example, Figure 3-8(b) shows that the distributed particles generate a sufficient void volume, and it decreases the strength of the Al matrix even if only small cracks occur among 500 particles. During the process, the strain is concentrated in the matrix, while further cracking of the Si particles becomes stable. This phenomenon is similar

to the stress relaxation mentioned by Lewis and Withers [72].

5.4. Effect of macrovoid on ductile fracture

In Section 5.2, the analysis with developed modeling revealed that the fracture of the cast Al alloy was more sensitive to the macrovoid location than its overall volume fraction. Therefore, the fracture behavior of the material with macrovoids was further investigated by comparing the simulated results with experiments using specially designed specimens.

The two uniaxial specimens with different initial macrovoid configurations at the center (or major deformation region) were prepared [Figure 5-8 (a) and (c)], and also a specimen with a 5-mm notch radius [Figure 5-9(a)]. The voids in different sections along the sheet thickness were measured by X-ray tomography using GE/VtomeX240. Each image in Figures 5-8 and 5-9 was taken from the bottom of the sheet, and the number on each specimen indicates the distance (with unit mm) from the bottom. During deformation, the growth of macrovoids was observed, and their results are shown in Figures 5-8(b), (d), and 5-9(b). The figures clearly show the visible growth of macrovoids located at the major deformation region, which leads to the final fracture. Especially, for the two oval-shaped macrovoids located at the center of the tensile specimen in Figure 5-8(c), only the lower one selectively grew, though the upper one had a larger size [Figure 5-8(d)]. This trend may be because the voids located near the specimen's edge (indicated with white arrows) initiate the earlier fracture with the support of microvoids, and the fracture propagates through the macrovoids located at the major deformation region.

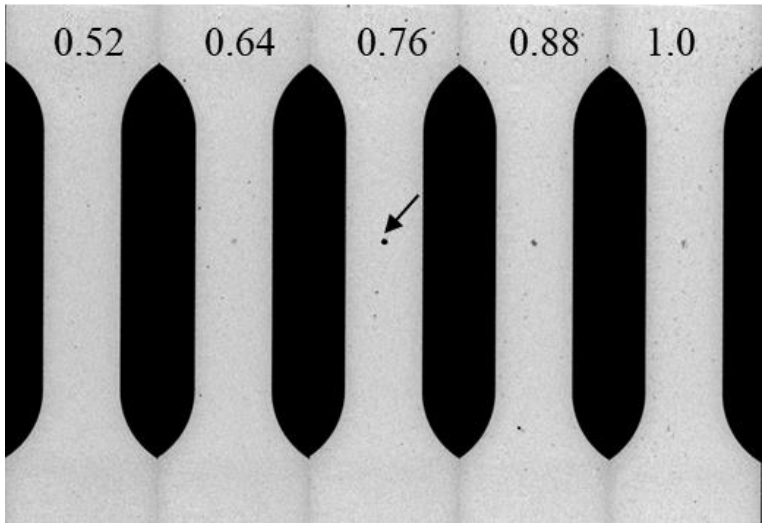

(a)

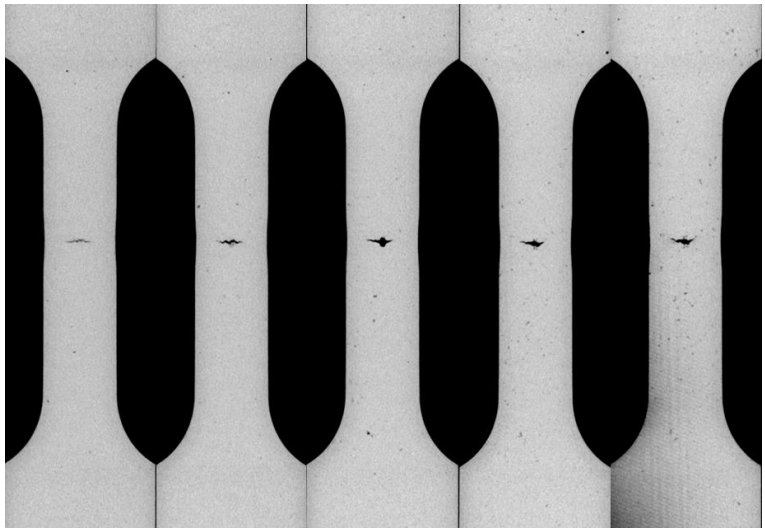

(b)

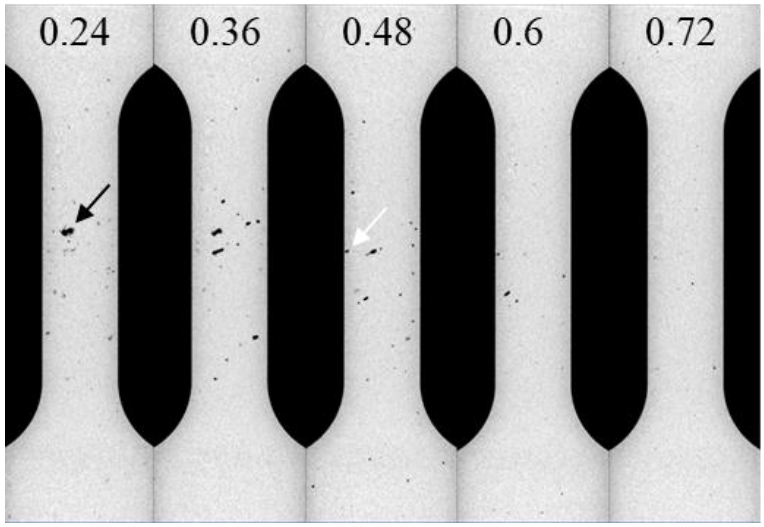

(c)

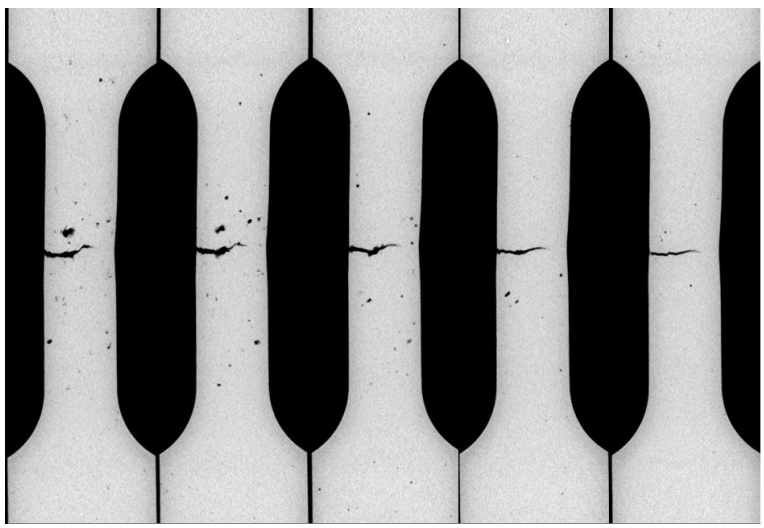

(d)

Figure 5-8. Series of Micro-CT images sliced in the specimen's thickness direction, including macrovoids. (b) and (d) are images after interrupted tests using (a) and (c), respectively. Numbers written on the images represent the distance from the bottom of the specimen.

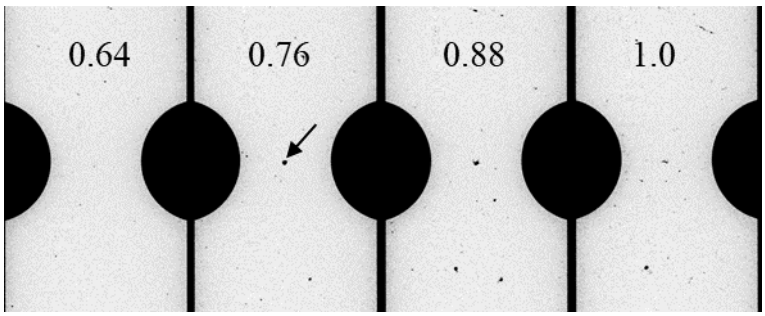

(a)

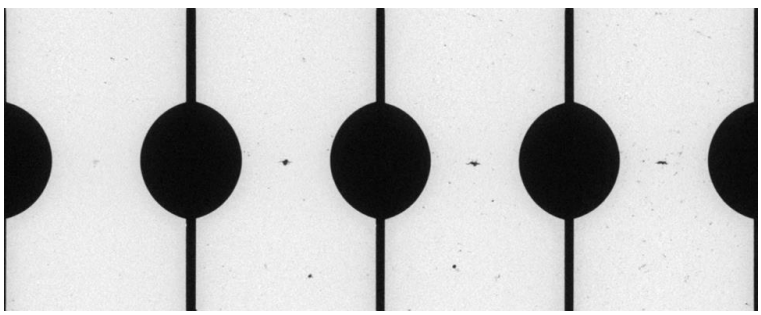

(b)

Figure 5-9. Series of Micro-CT images sliced in the thickness direction of NT, including macrovoids. (b) Image after interrupted tests using (a). Numbers written on the images indicate the distance from the bottom of the specimen.

To validate the effect of macrovoids on the observed fracture propagation, FE simulations were conducted with the same specimens and macrovoids as in Figures 5-8(a), (c), and 5-9(a). The exact size and location of macrovoids were measured by counting the number of pixels from the micro-CT. The pixel size in Figures 5-8 and 5-9 was 40 μm, which corresponds to the voxel size of the

3D micro-CT. Then, the lengths of major and minor axes of the voids indicated by the black arrows of Figures 5-8(a), (c), and 5-9(a) were approximately (0.5, 0.45), (1.0, 0.45), and (0.4, 0.3) mm, respectively. Figures 5-10(b), (d), and 5-11(b) show the results of the macrovoid evolutions during the tensile simulations, which all matched well with those of Figures 5-8(a), (c), and 5-9(a), respectively. The simulated results agree well with the experimental results where the fracture initiated from the macrovoids located at the major deformation region [Figures 5-10(b) and 5-11(b)]. White arrows indicate the propagation of the damage in Figure 5-10(d).

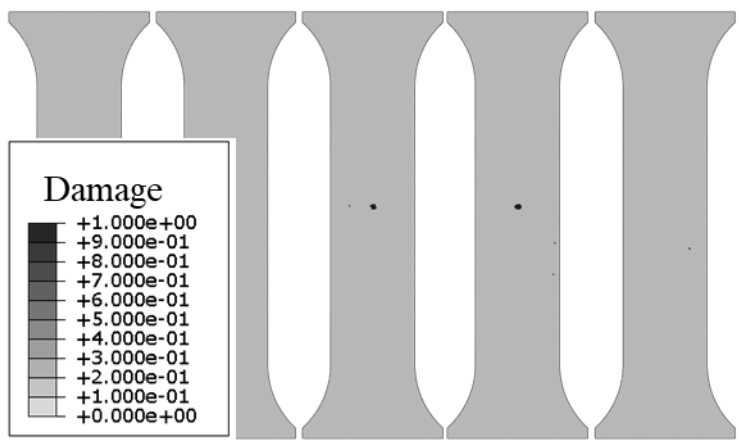

(a)

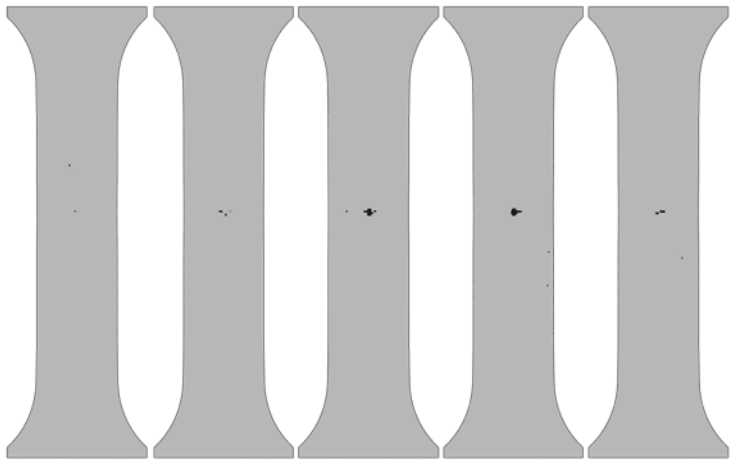

(b)

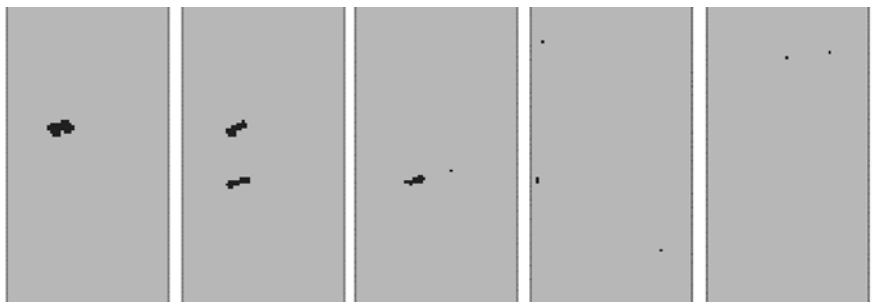

(c)

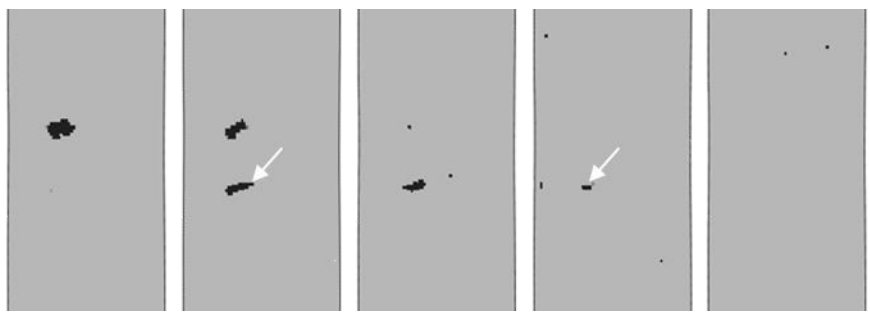

(d)

Figure 5-10. FE models of specimens containing voids as micro-CT images in Figure 5-8. (a) and (c) correspond to (a) and (c) in Figure 5-8, respectively. (b) and (d) are simulation results with damage contours.

The load–displacement curves of the three specimens are shown in Figure 5-12 for both the experiments and simulations. As usual, the scatters shown in the simulated curves are indicated as empty boxes. Note that the predicted load–displacement curves agree excellently with those of the experiment in terms of both flow stresses and fracture strains. Moreover, compared to Figure 4-4(a) and (c), rather earlier fracture was predicted when macrovoids are located at the center of the specimens.

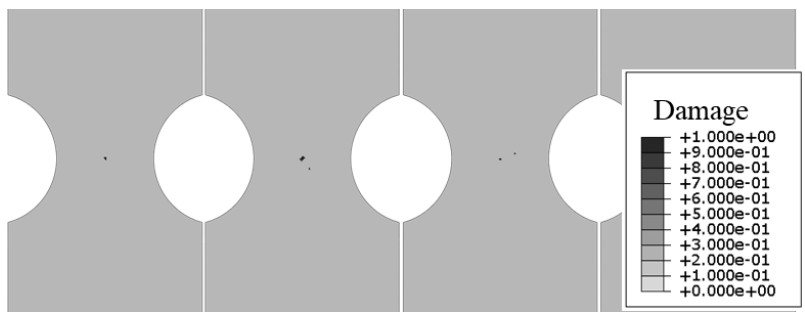

(a)

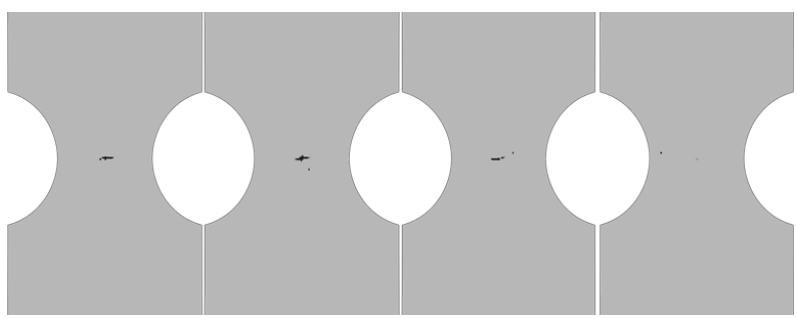

(b)

Figure 5-11. FE models of specimens containing voids as micro-CT images in Figure 5-9. (a) Corresponds to (a) in Figure 5-9. (b) Simulation result with damage contours.

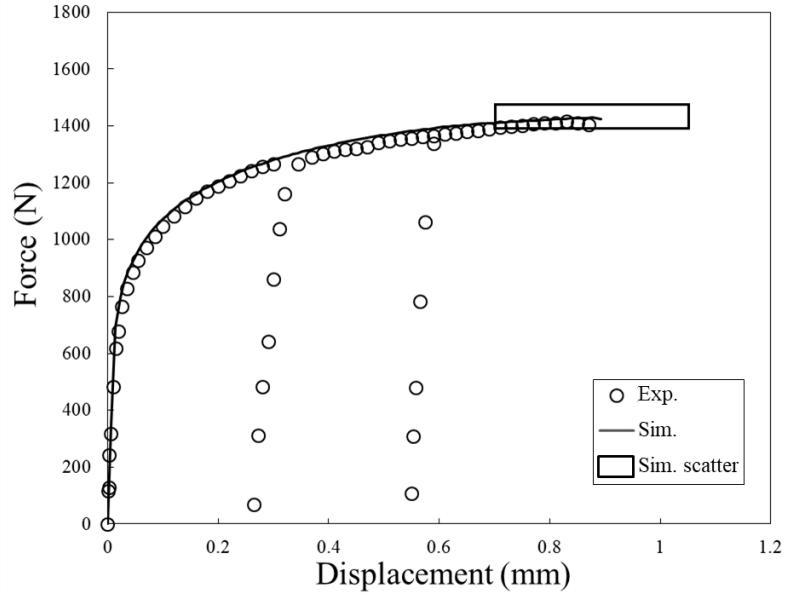
Force (N)
Displacement (mm)
Exp.
Sim.
Sim. scatter

(a)

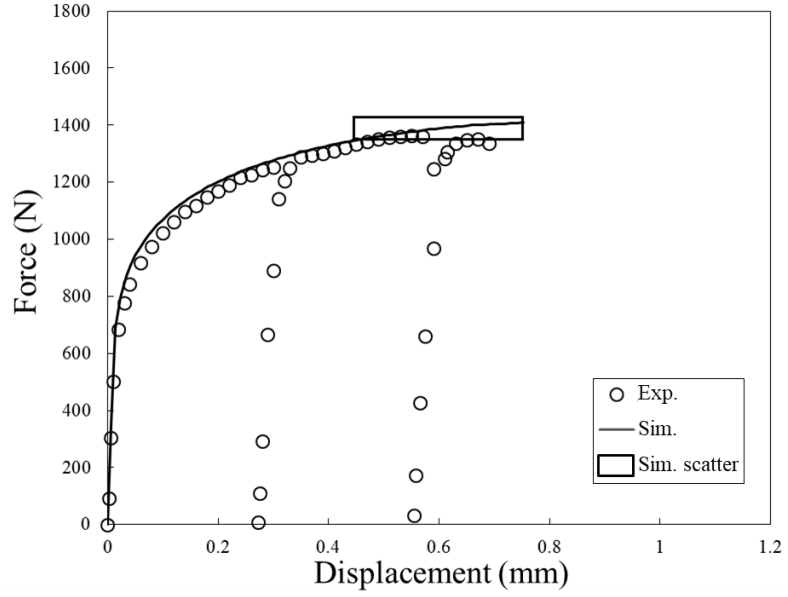
Force (N)
Displacement (mm)
Exp.
Sim.
Sim. scatter

(b)

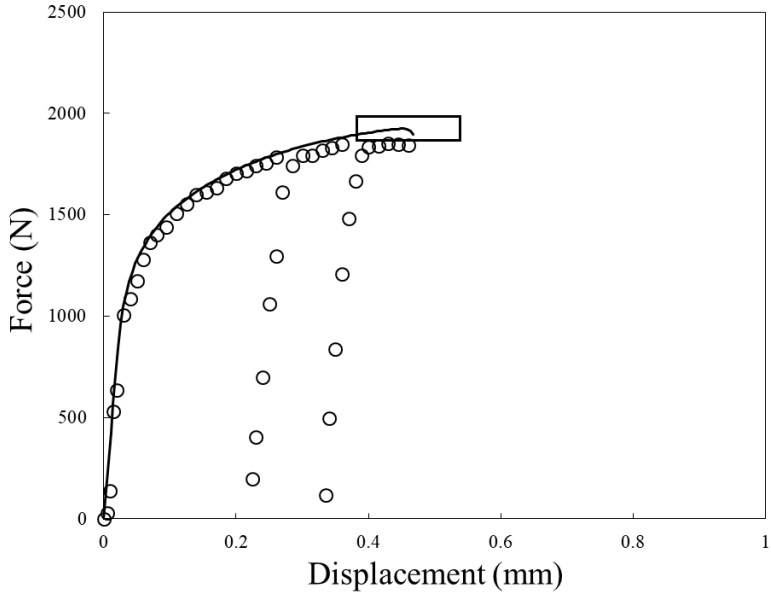

(c)

Figure 5-12. Force–displacement curves of both experiments and simulations from (a) Figures 5-8(a) and 5-10(a), (b) Figures 5-8(c) and 5-10(c), (c) Figures 5-9(a) and 5-11(a).

5.5. Fracture behavior with few voids

In Sections 5.2 and 5.4, the negative effect of macrovoids on fracture displacement was studied. To accurately understand the macrovoid effect, specimens containing few macrovoids were prepared, and a tensile test was performed to obtain a control group. Figure 5-13(a) is a micro-CT analysis image of the specimen obtained during this process. Macrovoids are observed, but their size is < 100 mm, and they are located around the grip part, so it can be said that they do not affect the specimen's mechanical properties.

Figure 5-13(b) shows the test and simulation results of the specimens with few macrovoids. Figure 5-13(b) shows the simulation results from Figure 4-4 in

Section 4.2. As in the previous case, the conditions of the microstructural distribution for the simulation were based on the statistical analysis, and the fraction of macrovoids was 0.01%. The experimental and simulation results shown in Figure 5-13(b) are in good agreement. Precisely, the lowest ductility observed in the experiment was predicted with high accuracy through simulation. The experimental results in Figure 5-13(b) indicate that microstructures, except for macrovoids, also induce fracture scattering, which is consistent with the contents of this study. In summary, macrovoids, microvoids, Si particles, the microstructure of the material all causes scattering of cracks. Among them, macrovoids have the greatest influence, and the role of Si particles is also significant.

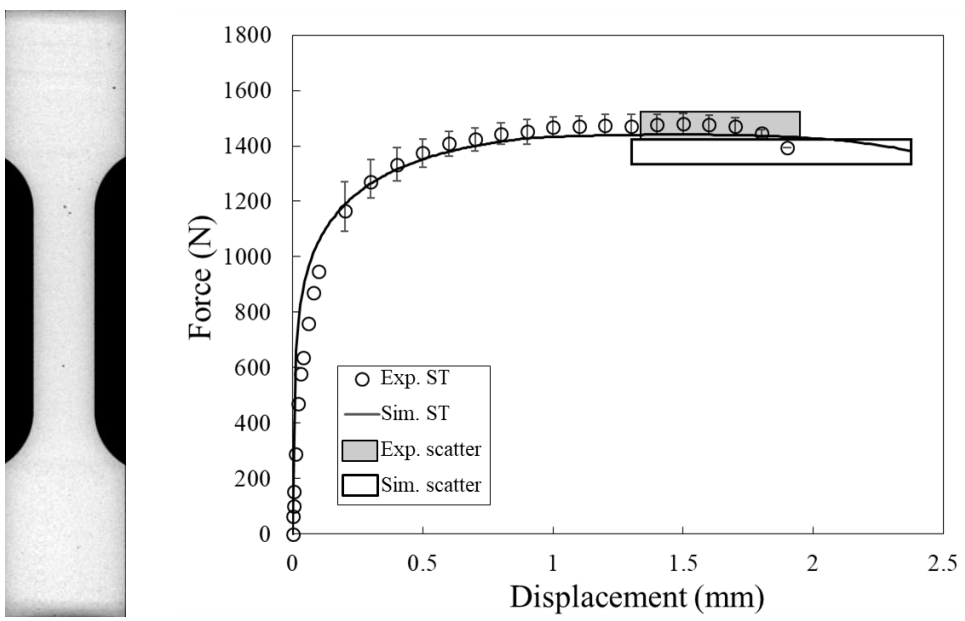

(a) (b)

Figure 5-13. (a) Micro-CT image of specimens with few voids and (b) force–displacement curves of specimens with few voids.

6. Conclusion

The mechanical behavior and fracture behavior of a cast Al alloy were predicted using the model proposed herein. The homogenized response of the Al matrix and Si particles and the stress and strain of each phase were obtained using the Mori–Tanaka mean-field method. The Weibull distribution function was used to determine whether cracks occurred based on the size and stress state of the Si particles. The cracked Si particles were converted into voids, and the Gurson–Tvergaard–Needleman (GTN) model was used to calculate the increase in the void fraction and damage evolution.

The model proposed herein could predict the mechanical behavior of cast Al alloys and the fracture behavior, showing scatter with reasonable accuracy with only one parameter set. The GTN and Weibull parameters obtained through an iterative calculation had values in a range similar to those of previous studies.

- The optical microscopy and SEM analysis confirmed that the major fracture of the A365.0 alloy initiated from the cracking of the Si particles in the eutectic zone of the matrix. Therefore, the basic assumption (of the GTN model) that the cracked Si particles are regarded as the source of newly generated microvoids for ductile fracture was validated experimentally.
- Simulation using the proposed model showed that fractures occur early when the volume fraction of macrovoids and the size of macrovoids located at major deformation sites increase. Precisely, the

size of the macrovoids located in the deformation-concentrated has been shown to have an overwhelming effect on the early fracture of the material. In the simulation, a macrovoid fraction of 100 times or more was required to simulate the early fracture of the material by increasing the macrovoid volume fraction of the entire specimen area. This outcome indicates that the relatively small size of the macrovoid may not have a significant impact on fracture if evenly distributed in the material.

- A typical phenomenological fracture model describes fracture so that damages accumulate based on an equivalent plastic strain increment in the stress state. Therefore, an element has a level of damage similar to that of the surrounding element. However, in the proposed model, the cracks in the Si particles occur from the Weibull distribution-based probabilistic model, and the accumulation of damage starts from there. Therefore, the damage level of an element tends to be significantly different from that of the surrounding elements. This characteristic of the proposed model may cause fractures in noncentral parts of the specimen. Probabilistically, cracks of the Si particles may occur at locations off-center of the specimen, resulting in damage evolution, which causes the loss of the load-carrying capacity of the material points. Besides, the load is distributed around the integration point where it has lost its load-carrying capacity, and the repetition of the same process propagates the fracture.
- When a Si particle was cracked, the relaxed stress in the

neighborhood of the cracked particle could explain the inhomogeneous and sequential crack propagation characteristics through the matrix.

Reference

[1] Davis, J. R. (1993). Aluminum and aluminum alloys. ASM international.

[2] Ogris, E., Wahlen, A., Lüchinger, H., & Uggowitzer, P. J. (2002). On the silicon spheroidization in Al–Si alloys. Journal of Light Metals, 2(4), 263-269.

[3] Mae, H., Teng, X., Bai, Y., & Wierzbicki, T. (2007). Calibration of ductile fracture properties of a cast aluminum alloy. Materials Science and Engineering: A, 459(1-2), 156-166.

[4] Teng, X., Mae, H., Bai, Y., & Wierzbicki, T. (2008). Statistical analysis of ductile fracture properties of an aluminum casting. Engineering fracture mechanics, 75(15), 4610-4625.

[5] Teng, X., Mae, H., Bai, Y., & Wierzbicki, T. (2009). Pore size and fracture ductility of aluminum low pressure die casting. Engineering Fracture Mechanics, 76(8), 983-996.

[6] Bao, Y., & Wierzbicki, T. (2004). On fracture locus in the equivalent strain and stress triaxiality space. International Journal of Mechanical Sciences, 46(1), 81-98.

[7] Francis, J. A., & Cantin, G. D. (2005). The role of defects in the fracture of an Al–Si–Mg cast alloy. Materials Science and Engineering: A, 407(1-2), 322-329.

[8] Lee, C., Shin, K., & Kim, Y. (2017). Dependence of tensile ductility on damage evolution of eutectic Si-particles and pre-existing micro-voids in Al-Si casting alloy. Engineering Fracture Mechanics, 175, 339-356.

[9] Liu, R., Zheng, J., Godlewski, L., Zindel, J., Li, M., Li, W., & Huang, S. (2020). Influence of pore characteristics and eutectic particles on the tensile properties of Al–Si–Mn–Mg high pressure die casting alloy. Materials Science and Engineering: A, 783, 139280.

[10] Lordan, E., Lazaro-Nebreda, J., Zhang, Y., Dou, K., Blake, P., & Fan, Z. (2020). On the relationship between internal porosity and the tensile ductility of aluminium alloy die-castings. Materials Science and Engineering: A, 778, 139107.

[11] Wang, Q. G. (2003). Microstructural effects on the tensile and fracture behavior of aluminum casting alloys A356/357. Metallurgical and materials Transactions A, 34(12), 2887-2899.

[12] Wang, Q. G., Caceres, C. H., & Griffiths, J. R. (2003). Damage by eutectic particle cracking in aluminum casting alloys A356/357. Metallurgical and Materials Transactions A, 34(12), 2901-2912.

[13] Mueller, M. G., Žagar, G., & Mortensen, A. (2018). In-situ strength of individual silicon particles within an aluminium casting alloy. Acta Materialia, 143, 67-76.

[14] Gurson, A. L. (1977). Continuum theory of ductile rupture by void nucleation and growth: Part I—Yield criteria and flow rules for porous ductile media.

[15] Chu, C. C., & Needleman, A. (1980). Void nucleation effects in biaxially stretched sheets.

[16] Tvergaard, V. (1982). On localization in ductile materials containing spherical voids. International Journal of fracture, 18(4), 237-252.

[17] Tvergaard, V., & Needleman, A. (1984). Analysis of the cup-cone fracture in a round tensile bar. Acta metallurgica, 32(1), 157-169.

[18] Horstemeyer, M. F., Lathrop, J., Gokhale, A. M., & Dighe, M. (2000). Modeling stress state dependent damage evolution in a cast Al–Si–Mg aluminum alloy. Theoretical and applied fracture mechanics, 33(1), 31-47.

[19] McClintock, F. A. (1968). A criterion for ductile fracture by the growth of holes.

[20] Bammann, D. J., Chiesa, M. L., & Johnson, G. C. (1996). Modeling large deformation and failure in manufacturing processes. Theoretical and Applied Mechanics, 9, 359-376.

[21] Baral, M., Ha, J., & Korkolis, Y. P. (2019). Plasticity and ductile fracture modeling of an Al–Si–Mg die-cast alloy. International Journal of Fracture, 216(1), 101-121.

[22] Oyane, M., Sato, T., Okimoto, K., & Shima, S. (1980). Criteria for ductile fracture and their applications. Journal of Mechanical Working Technology, 4(1), 65-81.

[23] Johnson, G. R., & Cook, W. H. (1985). Fracture characteristics of three metals subjected to various strains, strain rates, temperatures and pressures. Engineering fracture mechanics, 21(1), 31-48.

[24] Mohr, D., & Marcadet, S. J. (2015). Micromechanically-motivated phenomenological Hosford–Coulomb model for predicting ductile fracture initiation at low stress triaxialities. International Journal of Solids and Structures, 67, 40-55.

[25] Barlat, F., Aretz, H., Yoon, J. W., Karabin, M. E., Brem, J. C., & Dick, R.

E. (2005). Linear transfomation-based anisotropic yield functions. International Journal of Plasticity, 21(5), 1009-1039.

[26] Fagerholt, E., Dørum, C., Børvik, T., Laukli, H. I., & Hopperstad, O. S. (2010). Experimental and numerical investigation of fracture in a cast aluminium alloy. International Journal of Solids and Structures, 47(24), 3352-3365.

[27] Cockcroft, M. G. (1968). Ductility and workability of metals. J. of Metals., 96, 2444.

[28] Agarwal, B. D., & Broutman, L. J. (1974). Three-dimensional finite element analysis of spherical particle composites. Fibre Science and Technology, 7(1), 63-77.

[29] Agarwal, B. D., Panizza, G. A., & Broutman, L. J. (1971). Micromechanics analysis of porous and filled ceramic composites. Journal of the American Ceramic Society, 54(12), 620-624.

[30] Weissenbek, E., Böhm, H. J., & Rammerstorfer, F. G. (1994). Micromechanical investigations of arrangement effects in particle reinforced metal matrix composites. Computational materials science, 3(2), 263-278.

[31] Lee, K., Moorthy, S., & Ghosh, S. (1999). Multiple scale computational model for damage in composite materials. Computer methods in applied mechanics and engineering, 172(1-4), 175-201.

[32] Ghosh, S., Lee, K., & Moorthy, S. (1995). Multiple scale analysis of heterogeneous elastic structures using homogenization theory and Voronoi cell finite element method. International Journal of Solids and

Structures, 32(1), 27-62.

[33] Ghosh, S., Lee, K., & Moorthy, S. (1996). Two scale analysis of heterogeneous elastic-plastic materials with asymptotic homogenization and Voronoi cell finite element model. Computer methods in applied mechanics and engineering, 132(1-2), 63-116.

[34] Ghosh, S., Lee, K., & Raghavan, P. (2001). A multi-level computational model for multi-scale damage analysis in composite and porous materials. International Journal of Solids and Structures, 38(14), 2335-2385.

[35] Ghosh, S., Bai, J., & Paquet, D. (2009). Homogenization-based continuum plasticity-damage model for ductile failure of materials containing heterogeneities. Journal of the Mechanics and Physics of Solids, 57(7), 1017-1044.

[36] Böhm, H. J., Eckschlager, A., & Han, W. (2002). Multi-inclusion unit cell models for metal matrix composites with randomly oriented discontinuous reinforcements. Computational materials science, 25(1-2), 42-53.

[37] Shen, H., & Lissenden, C. J. (2002). 3D finite element analysis of particle-reinforced aluminum. Materials Science and Engineering: A, 338(1-2), 271-281.

[38] Böhm, H. J., Han, W., & Eckschlager, A. (2004). Multi-inclusion unit cell studies of reinforcement stresses and particle failure in discontinuously reinforced ductile matrix composites. na.

[39] Mori, T., & Tanaka, K. (1973). Average stress in matrix and average elastic energy of materials with misfitting inclusions. Acta

metallurgica, 21(5), 571-574.

[40] Tanaka, K., & Mori, T. (1970). The hardening of crystals by non-deforming particles and fibres. Acta Metallurgica, 18(8), 931-941.

[41] Doghri, I., & Ouaar, A. (2003). Homogenization of two-phase elasto-plastic composite materials and structures: Study of tangent operators, cyclic plasticity and numerical algorithms. International Journal of Solids and structures, 40(7), 1681-1712.

[42] Delannay, L., Doghri, I., & Pierard, O. (2007). Prediction of tension–compression cycles in multiphase steel using a modified incremental mean-field model. International Journal of Solids and Structures, 44(22-23), 7291-7306.

[43] Delannay, L., Jacques, P., & Pardoen, T. (2008). Modelling of the plastic flow of trip-aided multiphase steel based on an incremental mean-field approach. International Journal of Solids and Structures, 45(6), 1825-1843.

[44] Simar, A., Mertens, A., Ryelandt, S., Delannay, F., & Brassart, L. (2018). Mean-field model analysis of deformation and damage in friction stir processed Mg-C composites. Materials Science and Engineering: A, 723, 324-333.

[45] Rutecka, A., Kursa, M., Pietrzak, K., Kowalczyk-Gajewska, K., Makowska, K., & Wyszkowski, M. (2020). Damage evolution in AA2124/SiC metal matrix composites under tension with consecutive unloadings. Archives of Civil and Mechanical Engineering, 20(4), 1-18.

[46] Eshelby, J. D. (1957). The determination of the elastic field of an ellipsoidal inclusion, and related problems. Proceedings of the royal

society of London. Series A. Mathematical and physical sciences, 241(1226), 376-396.

[47] Hill, R. (1965). A self-consistent mechanics of composite materials. Journal of the Mechanics and Physics of Solids, 13(4), 213-222.

[48] Gurland, J. (1972). Observations on the fracture of cementite particles in a spheroidized 1.05% C steel deformed at room temperature. Acta Metallurgica, 20(5), 735-741.

[49] Lindley, T. C., Oates, G., & Richards, C. E. (1970). A critical of carbide cracking mechanisms in ferride/carbide aggregates. Acta metallurgica, 18(11), 1127-1136.

[50] Wallin, K., Saario, T., & Törrönen, K. (1986). Fracture of brittle particles in a ductile matrix. International journal of fracture, 32(3), 201-209.

[51] Budiansky, B. (1965). On the elastic moduli of some heterogeneous materials. Journal of the Mechanics and Physics of Solids, 13(4), 223-227.

[52] Bate, P., Roberts, W. T., & Wilson, D. V. (1981). The plastic anisotropy of two-phase aluminium alloys—I. Anisotropy in unidirectional deformation. Acta Metallurgica, 29(11), 1797-1814.

[53] Barlat, F., & Liu, J. (1998). Precipitate-induced anisotropy in binary Al-Cu alloys. Materials Science and Engineering: A, 257(1), 47-61.

[54] Weng, G. J. (1984). Some elastic properties of reinforced solids, with special reference to isotropic ones containing spherical inclusions. International Journal of Engineering Science, 22(7), 845-856.

[55] Benveniste, Y. (1987). A new approach to the application of Mori-Tanaka's theory in composite materials. Mechanics of materials, 6(2), 147-

157.

[56] Lagoudas, D. C., Gavazzi, A. C., & Nigam, H. (1991). Elastoplastic behavior of metal matrix composites based on incremental plasticity and the Mori-Tanaka averaging scheme. Computational Mechanics, 8(3), 193-203.

[57] Perdahcıoğlu, E. S., & Geijselaers, H. J. (2011). Constitutive modeling of two phase materials using the mean field method for homogenization. International journal of material forming, 4(2), 93-102.

[58] Bornert, M., Bretheau, T., & Gilormini, P. (2001). Homogénéisation en mécanique des matériaux, Tome 1: Matériaux aléatoires élastiques et milieux périodiques (pp. 250-pages). Hermes science.

[59] Gavazzi, A. C., & Lagoudas, D. C. (1990). On the numerical evaluation of Eshelby's tensor and its application to elastoplastic fibrous composites. Computational mechanics, 7(1), 13-19.

[60] Mura, T. (2013). Micromechanics of defects in solids. Springer Science & Business Media.

[61] Christensen, R., Schantz, H., & Shapiro, J. (1992). On the range of validity of the Mori-Tanaka method. Journal of the Mechanics and Physics of Solids, 40(1), 69-73.

[62] Rice, J. R., & Tracey, D. M. (1969). On the ductile enlargement of voids in triaxial stress fields*. Journal of the Mechanics and Physics of Solids, 17(3), 201-217.

[63] Tvergaard, V. (1981). Influence of voids on shear band instabilities under plane strain conditions. International Journal of fracture, 17(4), 389-407.

[64] Xue, L. (2008). Constitutive modeling of void shearing effect in ductile fracture of porous materials. Engineering Fracture Mechanics, 75(11), 3343-3366.

[65] Nahshon, K., & Hutchinson, J. W. (2008). Modification of the Gurson model for shear failure. European Journal of Mechanics-A/Solids, 27(1), 1-17.

[66] McClintock, F. A., Kaplan, S. M., & Berg, C. A. (1966). Ductile fracture by hole growth in shear bands. International Journal of Fracture Mechanics, 2(4), 614-627.

[67] Berg, C. A. (1962, June). The motion of cracks in plane viscous deformation. In Proceedings of the fourth US national congress of applied mechanics (Vol. 2, pp. 885-892). American Society of Mechanical Engineers New York.

[68] Aravas, N. (1987). On the numerical integration of a class of pressure-dependent plasticity models. International Journal for numerical methods in engineering, 24(7), 1395-1416.

[69] Bettaieb, M. B., Lemoine, X., Duchêne, L., & Habraken, A. M. (2011). On the numerical integration of an advanced Gurson model. International journal for numerical methods in engineering, 85(8), 1049-1072.

[70] Malcher, L., Pires, F. A., & De Sá, J. C. (2014). An extended GTN model for ductile fracture under high and low stress triaxiality. International Journal of Plasticity, 54, 193-228.

[71] Simo, J. C., & Hughes, T. J. (2006). Computational inelasticity (Vol. 7). Springer Science & Business Media.

[72] Lewis, C. A., & Withers, P. J. (1995). Weibull modelling of particle cracking in metal matrix composites. Acta metallurgica et materialia, 43(10), 3685-3699.

[73] Mochida, T., Taya, M., & Lloyd, D. J. (1991). Fracture of particles in a particle/metal matrix composite under plastic straining and its effect on the Young's modulus of the composite. Materials Transactions, JIM, 32(10), 931-942.

[74] Llorca, J., Martin, A., Ruiz, J., & Elices, M. (1993). Particulate fracture during deformation. Metallurgical Transactions A, 24(7), 1575-1588.

[75] Brechet, Y., Embury, J. D., Tao, S., & Luo, L. (1991). Damage initiation in metal matrix composites. Acta metallurgica et materialia, 39(8), 1781-1786.

[76] Caceres, C. H., & Griffiths, J. R. (1996). Damage by the cracking of silicon particles in an Al-7Si-0.4 Mg casting alloy. Acta materialia, 44(1), 25-33.

[77] Biswas, P., Patra, S., Roy, H., Tiwary, C. S., Paliwal, M., & Mondal, M. K. (2019). Effect of Mn Addition on the Mechanical Properties of Al–12.6 Si Alloy: Role of Al 15 (MnFe) 3 Si 2 Intermetallic and Microstructure Modification. Metals and Materials International, 1-15.

[78] Ferraro, S., Fabrizi, A., & Timelli, G. (2015). Evolution of sludge particles in secondary die-cast aluminum alloys as function of Fe, Mn and Cr contents. Materials Chemistry and Physics, 153, 168-179.

[79] Shabestari, S. G. (2004). The effect of iron and manganese on the formation of intermetallic compounds in aluminum–silicon

alloys. Materials Science and Engineering: A, 383(2), 289-298.

[80] Mondolfo, L. F. (2013). Aluminum alloys: structure and properties. Elsevier.

[81] Brown, L. M. (1973). Back-stresses, image stresses, and work-hardening. Acta Metallurgica, 21(7), 879-885.

[82] Brown, L. M., & Clarke, D. R. (1975). Work hardening due to internal stresses in composite materials. Acta Metallurgica, 23(7), 821-830.

[83] Brown, L. M., & Stobbs, W. (1971). The work-hardening of copper-silica. Philosophical Magazine, 23(185), 1185-1199.

[84] Brown, L. M., & Stobbs, W. (1971). The work-hardening of copper-silica. Philosophical Magazine, 23(185), 1201-1233.

[85] Min, H. E., Fuguo, L. I., & Zhigang, W. A. N. G. (2011). Forming limit stress diagram prediction of aluminum alloy 5052 based on GTN model parameters determined by in situ tensile test. Chinese Journal of Aeronautics, 24(3), 378-386.

[86] Li, G., & Cui, S. (2020). Meso-mechanics and damage evolution of AA5182-O aluminum alloy sheet Based on the GTN model. Engineering Fracture Mechanics, 235, 107162.

[87] Wang, X., Zhan, M., Guo, J., & Zhao, B. (2016). Evaluating the applicability of GTN damage model in forward tube spinning of aluminum alloy. Metals, 6(6), 136.

[88] Yildiz, R. A., & Yilmaz, S. (2020). Experimental Investigation of GTN model parameters of 6061 Al alloy. European Journal of Mechanics-A/Solids, 83, 104040.

[89] Kami, A., Dariani, B. M., Vanini, A. S., Comsa, D. S., & Banabic, D. (2015). Numerical determination of the forming limit curves of anisotropic sheet metals using GTN damage model. Journal of Materials Processing Technology, 216, 472-483.

[90] Yu, H., Tieu, K., Lu, C., Lou, Y., Liu, X., Godbole, A., & Kong, C. (2014). Tensile fracture of ultrafine grained aluminum 6061 sheets by asymmetric cryorolling for microforming. International journal of damage mechanics, 23(8), 1077-1095.

[91] Nguyen, H. H., Nguyen, T. N., & Vu, H. C. (2018). Ductile fracture prediction and forming assessment of AA6061-T6 aluminum alloy sheets. International Journal of Fracture, 209(1), 143-162.

[92] Ying, L., Gao, T., Rong, H., Han, X., Hu, P., & Hou, W. (2019). On the thermal forming limit diagram (TFLD) with GTN mesoscopic damage model for AA7075 aluminum alloy: Numerical and experimental investigation. Journal of Alloys and Compounds, 802, 675-693.

[93] Abbasi, M., Shafaat, M. A., Ketabchi, M., Haghshenas, D. F., & Abbasi, M. (2012). Application of the GTN model to predict the forming limit diagram of IF-Steel. Journal of Mechanical science and Technology, 26(2), 345-352.

[94] Abbassi, F., Mistou, S., & Zghal, A. (2013). Failure analysis based on microvoid growth for sheet metal during uniaxial and biaxial tensile tests. Materials & Design, 49, 638-646.

[95] Cao, T. S., Maire, E., Verdu, C., Bobadilla, C., Lasne, P., Montmitonnet, P., & Bouchard, P. O. (2014). Characterization of ductile damage for a high

carbon steel using 3D X-ray micro-tomography and mechanical tests–Application to the identification of a shear modified GTN model. Computational Materials Science, 84, 175-187.

[96] Zhao, P. J., Chen, Z. H., & Dong, C. F. (2016). Failure analysis based on microvoids damage model for DP600 steel on in-situ tensile tests. Engineering fracture mechanics, 154, 152-168.

[97] Cha, W. G., & Kim, N. (2014). Quantification of micro-cracks on the bending surface of roll formed products using the GTN model. Metals and Materials International, 20(5), 841-850.

[98] Zhang, W. W., & Cong, S. (2016). Failure analysis of SUS304 sheet during hydro-bulging based on GTN ductile damage model. The International Journal of Advanced Manufacturing Technology, 86(1), 427-435.

[99] Yuenyong, J., Suthon, M., Kingklang, S., Thanakijkasem, P., Mahabunphachai, S., & Uthaisangsuk, V. (2018). Formability prediction for tube hydroforming of stainless steel 304 using damage mechanics model. Journal of Manufacturing Science and Engineering, 140(1).

[100] Kumar, P., Dutta, B. K., & Chattopadhyay, J. (2017). Fracture toughness prediction of reactor grade materials using pre-notched small punch test specimens. Journal of Nuclear Materials, 495, 351-362.

[101] Oh, C. K., Kim, Y. J., Baek, J. H., Kim, Y. P., & Kim, W. (2007). A phenomenological model of ductile fracture for API X65 steel. International Journal of Mechanical Sciences, 49(12), 1399-1412.

[102] Hosford, W. F. (1972). A generalized isotropic yield criterion.

[103] Hosford, W. F. (1979, May). On yield loci of anisotropic cubic metals. In Proceedings of the Seventh North American Metal working Conference SME (pp. 191-197).

[104] Hill, R. (1979, January). Theoretical plasticity of textured aggregates. In Mathematical Proceedings of the Cambridge Philosophical Society (Vol. 85, No. 1, pp. 179-191). Cambridge University Press.

[105] Bai, Y., & Wierzbicki, T. (2010). Application of extended Mohr–Coulomb criterion to ductile fracture. International journal of fracture, 161(1), 1.

[106] Bao, Y., & Wierzbicki, T. (2004). A comparative study on various ductile crack formation criteria. J. Eng. Mater. Technol., 126(3), 314-324.

Appendix A. Partial derivatives of GTN variables.

The partial derivatives for implementing the GTN model are summarized as follows, as adopted from previous studies [64,68–70].

$$\frac{\partial \Phi}{\partial p} = -\frac{3q_2 D}{\sigma_Y}\sinh\left(-\frac{3q_2 p}{2\sigma_Y}\right) = \frac{3q_2 D}{\sigma_Y}\sinh\left(\frac{3q_2 p}{2\sigma_Y}\right)$$

$$\frac{\partial \Phi}{\partial q} = \frac{2q}{\sigma_Y^2}$$

$$\frac{\partial \Phi}{\partial H_1} = \frac{\partial \Phi}{\partial e^p} = \frac{\partial \Phi}{\partial \sigma_Y}\frac{\partial \sigma_Y}{\partial e^p}$$

$$\frac{\partial \Phi}{\partial H_2} = \frac{\partial \Phi}{\partial f} = 0$$

$$\frac{\partial \Phi}{\partial H_3} = \frac{\partial \Phi}{\partial D} = 2\cosh\left(-\frac{3q_2 p}{2\sigma_Y}\right) - 2D = 2\cosh\left(\frac{3q_2 p}{2\sigma_Y}\right) - 2D$$

$$\frac{\partial \Phi}{\partial \sigma_Y} = -\frac{2q^2}{\sigma_Y^3} - \frac{3q_2 Dp}{\sigma_Y^2}\sinh\left(\frac{3q_2 p}{2\sigma_Y}\right)$$

$$\frac{\partial^2 \Phi}{\partial p^2} = \frac{9q_2^2 D}{2\sigma_Y^2}\cosh\left(\frac{3q_2 p}{2\sigma_Y}\right)$$

$$\frac{\partial^2 \Phi}{\partial q \partial p} = 0$$

$$\frac{\partial^2 \Phi}{\partial p \partial H_1} = \frac{\partial^2 \Phi}{\partial p \partial e^p} = \frac{\partial^2 \Phi}{\partial p \partial \sigma_Y}\frac{\partial \sigma_Y}{\partial e^p}$$

$$\frac{\partial^2 \Phi}{\partial p \partial H_2} = \frac{\partial^2 \Phi}{\partial p \partial f} = 0$$

$$\frac{\partial^2\Phi}{\partial p\partial H_3}=\frac{\partial^2\Phi}{\partial p\partial D}=\frac{3q_2}{\sigma_Y}\sinh\left(\frac{3q_2p}{2\sigma_Y}\right)$$

$$\frac{\partial^2\Phi}{\partial p\partial\sigma_Y}=-\frac{3q_2D}{\sigma_Y^2}\sinh\left(\frac{3q_2p}{2\sigma_Y}\right)-\frac{9q_2^2Dp}{2\sigma_Y^3}\cosh\left(\frac{3q_2p}{2\sigma_Y}\right)$$

$$\frac{\partial^2\Phi}{\partial q^2}=\frac{2}{\sigma_Y^2}$$

$$\frac{\partial^2\Phi}{\partial q\partial H_1}=\frac{\partial^2\Phi}{\partial q\partial e^p}=\frac{\partial^2\Phi}{\partial q\partial\sigma_Y}\frac{\partial\sigma_Y}{\partial e^p}$$

$$\frac{\partial^2\Phi}{\partial q\partial H_2}=\frac{\partial^2\Phi}{\partial q\partial f}=0$$

$$\frac{\partial^2\Phi}{\partial q\partial H_3}=\frac{\partial^2\Phi}{\partial q\partial D}=0$$

$$\frac{\partial\Phi}{\partial q\partial\sigma_Y}=\frac{-4q}{\sigma_Y^3}$$

The increments of the state variables are

$$h_1=\Delta H_1=\Delta e^p=\frac{-p\Delta\varepsilon_p+q\Delta\varepsilon_q}{(1-f)\sigma_Y}$$

$$h_2=\Delta H_2=\Delta f=(1-f)\Delta\varepsilon_p$$

$$h_3=\Delta H_3=\Delta D=K_D\left\{q_1\Delta f+q_3f^{q_4}g_\theta\varepsilon_q\Delta\varepsilon_q\right\}$$

The partial derivatives of the state variables are presented as follows

$$\frac{\partial H_\alpha}{\partial\Delta\varepsilon_p}=\sum_{\beta=1}^{n}c_{\alpha\beta}\left(\frac{\partial h_\beta}{\partial\Delta\varepsilon_p}+K\frac{\partial h_\beta}{\partial p}\right)$$

$$\frac{\partial H_\alpha}{\partial\Delta\varepsilon_q}=\sum_{\beta=1}^{n}c_{\alpha\beta}\left(\frac{\partial h_\beta}{\partial\Delta\varepsilon_q}-3G\frac{\partial h_\beta}{\partial q}\right)$$

$$c_{\alpha\beta}^{-1}=\begin{bmatrix} 1-\dfrac{\partial h_1}{\partial H_1} & -\dfrac{\partial h_1}{\partial H_2} & -\dfrac{\partial h_1}{\partial H_3} \\ -\dfrac{\partial h_2}{\partial H_1} & 1-\dfrac{\partial h_2}{\partial H_2} & -\dfrac{\partial h_2}{\partial H_3} \\ -\dfrac{\partial h_3}{\partial H_1} & -\dfrac{\partial h_3}{\partial H_2} & 1-\dfrac{\partial h_3}{\partial H_3} \end{bmatrix}$$

$$\frac{\partial h_1}{\partial H_1}=\frac{\partial \Delta\varepsilon^p}{\partial e^p}=-\frac{-p\Delta\varepsilon_p+q\Delta\varepsilon_q}{(1-f)\sigma_Y{}^2}\frac{\partial\sigma_Y}{\partial e^p}=-\frac{h_1}{\sigma_Y}\frac{\partial\sigma_Y}{\partial e^p}$$

$$\frac{\partial h_1}{\partial H_2}=\frac{\partial \Delta\varepsilon^p}{\partial f}=\frac{-p\Delta\varepsilon_p+q\Delta\varepsilon_q}{(1-f)^2\sigma_Y}=\frac{h_1}{(1-f)}$$

$$\frac{\partial h_1}{\partial H_3}=\frac{\partial \Delta\varepsilon^p}{\partial D}=0$$

$$\frac{\partial h_2}{\partial H_1}=\frac{\partial \Delta f}{\partial e^p}=\frac{\partial\{(1-f)\Delta\varepsilon_p\}}{\partial e^p}=0$$

$$\frac{\partial h_2}{\partial H_2}=\frac{\partial \Delta f}{\partial f}=-\Delta\varepsilon_p$$

$$\frac{\partial h_2}{\partial H_3}=\frac{\partial \Delta f}{\partial D}=0$$

$$\frac{\partial h_3}{\partial H_1}=\frac{\partial \Delta D}{\partial \varepsilon^p}=K_D\left[q_1\frac{\partial h_2}{\partial H_1}+q_3 f^{q_4} g_\theta\left(h_1+H_1\frac{\partial h_1}{\partial H_1}\right)\right]$$

$$\frac{\partial h_3}{\partial H_2}=\frac{\partial \Delta D}{\partial f}=K_D\left[q_1\frac{\partial h_2}{\partial H_2}+q_3 q_4 f^{q_4-1} g(\theta) H_1 h_1\right]$$

$$\frac{\partial h_3}{\partial H_3}=\frac{\partial \Delta D}{\partial D}=0$$

$$\frac{\partial h_1}{\partial \Delta \varepsilon_p} = \frac{-p}{(1-f)\sigma_Y}$$

$$\frac{\partial h_1}{\partial \Delta \varepsilon_q} = \frac{q}{(1-f)\sigma_Y}$$

$$\frac{\partial h_1}{\partial p} = \frac{-\Delta \varepsilon_p}{(1-f)\sigma_Y}$$

$$\frac{\partial h_1}{\partial q} = \frac{\Delta \varepsilon_q}{(1-f)\sigma_Y}$$

$$\frac{\partial h_2}{\partial \Delta \varepsilon_p} = 1-f$$

$$\frac{\partial h_2}{\partial \Delta \varepsilon_q} = 0$$

$$\frac{\partial h_2}{\partial p} = 0$$

$$\frac{\partial h_2}{\partial q} = 0$$

$$\frac{\partial h_3}{\partial \Delta \varepsilon_p} = 0$$

$$\frac{\partial h_3}{\partial \Delta \varepsilon_q} = 0$$

$$\frac{\partial h_3}{\partial p} = 0$$

$$\frac{\partial h_3}{\partial q} = 0$$

Appendix B. Correction factor for true size of buried particle.

The particle sizes obtained from the optical microscope image are the exposed sizes, as shown in the Figure B1; thus, it needs to be corrected. Lewis and Withers estimated the actual size of the buried particles as follows [72].

The average measured radius of a particle is

$$w = \frac{1}{R}\int_0^R r dy \tag{B.1}$$

where R and r are the true and exposed radius of the particle, respectively, and y is the distance from the center to the exposed surface. The relationship between R, r, and y can be expressed in a simple formula as follows.

$$r^2 = R^2 - y^2 \tag{B.2}$$

$$y = R\sin\theta \tag{B.3}$$

Then Equation (B.1) becomes

$$w = \frac{1}{R}\int_0^{\pi/2} R^2\cos^2\theta d\theta \tag{B.4}$$

The result is then given as

$$w = \frac{\pi}{4}R \tag{B.5}$$

The correction factor between the true and exposed radius is $4/\pi$, ~1.27.

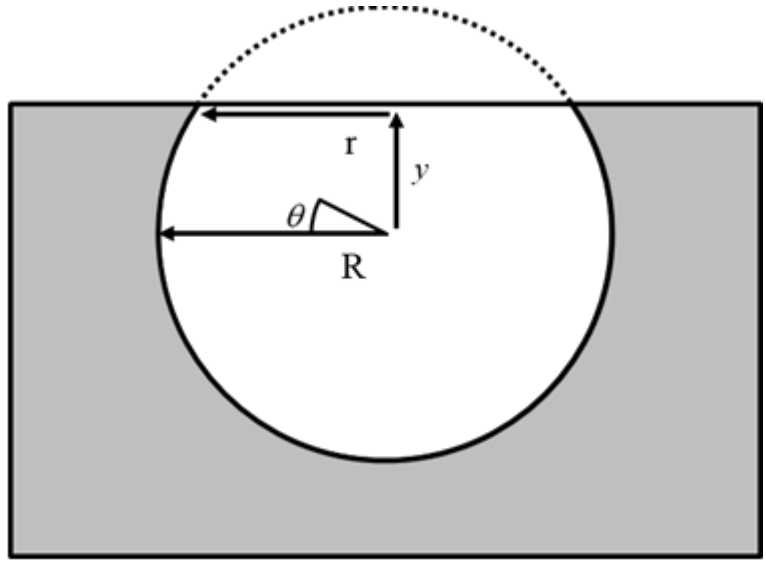

Figure B-1. Schematics of buried particle in matrix.

Abstract in Korean

알루미늄 주조 합금은 용접성, 부식 저항성 마모 저항성 등의 특성이 우수하고, 가벼워서 항공우주분야 및 자동차 산업에서 널리 사용된다. 본 논문에서 다루는 알루미늄 주조 합금은 A365.0-T6로 주조성을 높이기 위하여 규소(Si)를 첨가한 것이 특징이며, 마그네슘 및 망간이 주요 첨가 원소이다. 용체화 처리 후 인공 시효를 거치는 T6 열처리과정을 통하여 재료의 미세조직과 기계적 물성이 정해진다. 알루미늄 주조 합금은 알루미늄 기지(Matrix)와 규소 입자(Si particle), 금속간 화합물, Mg_2Si 석출물로 구성되어 있으며, 주조 공정 중 혼입된 공기로 인한 기공(Void) 결함이 관찰된다.

알루미늄 주조 합금은 큰 산포의 파단 변형률을 갖는다. 이는 재료 내에 존재하는 커다란 기공에 의한 것으로 알려져 있다. 기공이 없는 경우에는 개재물인 규소 입자의 균열로 인해 기공이 형성되고, 균열된 규소 입자 사이에 변형이 집중되어 재료의 손상을 유발하는 것으로 알려져 있다. 또한 일반적으로 연성 금속재료의 경우 기공의 형성, 성장, 합체로 파단을 설명하곤 하므로, 미소 기공도 재료의 기계적 물성에 영향을 미친다고 할 수 있다. 그러므로, 알루미늄 주조 합금의 미세조직 중 알루미늄 기지, 규소 입자, 기공이 재료의 기계적 거동과 파단 거동에 영향을 주는 주요 요소라 할 수 있다. 본 연구에서는 이러한 미세조직들의 물성에 기반한 멀티스케일 모델링을 통하여 알루미늄 주조 합금의 기계적 거동 및 산포를 보이는 파단 거동을 모사하고자 하였다.

미세조직의 분포를 실제 재료와 똑같이 유한요소 해석 상에서 구현하는 것은 효율적이지 않으므로, 이를 대체할 방법으로 모리-다나카 평균장

이론(Mori-Tanaka mean-field method, MT)을 도입했다. MT는 두 상(phase)으로 구성된 재료의 균질화된 기계적 거동을 몇 가지 가정과 Eshelby의 식을 바탕으로 도출할 수 있는 방법이다. RVE를 활용하여 다상의 평균 거동을 계산하는 방법에 비하여 계산의 효율이 좋고, 다양한 분포의 미세조직을 보다 용이하게 적용할 수 있는 장점이 있다. 미소기공이 알루미늄 기지에 속한다 가정하면, 알루미늄 주조합금은 알루미늄 기지와 규소 입자 두 상으로 이루어진 재료로 간주할 수 있으므로 MT의 적용이 가능해진다. MT로 균질화된 기계적 반응을 계산하는 과정에서 알루미늄 기지와 규소 입자의 응력 및 변형율도 함께 산출된다.

알루미늄 기지는 기공을 포함한다고 가정하였으므로, 기공의 성장 및 결합 (Coalescence)으로 인한 손상을 모사하는 damage coupling 모델인 Gurson-Tvergaard-Needleman (GTN) 모델을 적용하여 기계적 거동을 나타냈다. 규소 입자는 탄성 변형만 하므로 일반화된 훅의 법칙으로 응력을 산출했다. 바이불 분포 함수(Weibull distribution function)를 활용하여 규소 입자의 균열 여부를 판단했다. 규소 입자의 균열로 인해 생성되는 기공은 알루미늄 기지에 추가하여 GTN 모델로 재료의 손상을 계산할 때 적용되도록 모델링했다.

알루미늄 주조 합금이 다양한 응력 상태 아래에서 보이는 기계적 거동 및 파단 거동을 측정하기 위해 여러 형상의 시편을 활용하여 인장 실험을 진행했다. 미세조직 기반의 모델에 필요한 재료의 미세조직 분포 정보 획득을 위해 재료의 변형 전 미세조직을 관찰했다. Micro-CT, 광학현미경, 주사전자 현미경을 활용하여 미세조직을 통계적으로 분석했고, 이를 바탕으로 전산모사에 확률에 기반하여 적용했다. 변형 후의 미세조직

변화도 관찰하여 이 논문에서 제안한 방법의 타당성을 검증했다.

제안한 미세조직 기반 파단 예측 모델이 알루미늄 주조 합금의 기계적 거동 및 파단 거동을 잘 모사하는 것을 확인했으며, 기공의 분포와 크기가 재료의 파단에 미치는 영향을 분석했다. 특히 거대한 기공이 재료의 파단에 큰 영향을 주는 것을 확인했다. 규소 입자의 균열로부터 시작되는 재료의 손상 진화 과정, 삼축 응력도가 클수록 파단에 빨리 이르는 현상, 시편의 파단이 중앙이 아닌 곳에서 나타나는 현상을 제안된 모델로 모사할 수 있었다.

핵심어 : 알루미늄 주조 합금, 미세조직 기반 파단 모델, 모리-다나카 평균장 이론, Gurson-Tvergaard-Needleman model

학번 : 2019-38965

감사의 글

글 재주가 없어 간결하게 적습니다.

부모님께 가장 먼저 감사하다는 말씀을 드립니다. 어리지 않은 나이에 다시 공부를 하겠다고 했을 때 흔쾌히 응원하고 지지해 주셔서 감사합니다. 사랑합니다.

이명규 교수님께도 진심을 담아 감사의 마음을 전합니다. 운이 좋아서 교수님을 지도교수로 모실 수 있었습니다. 연구 과정에서 부족함이 없게 지원해 주신 것에 대해, 무사히 박사학위를 받을 수 있도록 지도해 주신 것에 대해 감사드립니다. 종종 안부인사 드리도록 하겠습니다.

연구실의 동료들 (김찬양, 최홍진, 민경문, 이기정, 명동준, 최유미, 박진흥, 김재승, 문찬미, 최성환, 홍서준, 원정윤, 신건진, 이형림, 방준호, 조서연, 김혜진, 김지영) 께도 감사드립니다. 여러분 덕에 학위 과정동안 즐거울 수 있었습니다. 코로나가 잠잠해지면 모두 모여 이야기 나눌 수 있으면 좋겠습니다.

산학과제를 통해 박사학위 과정간 연구 지원을 해 주신 현대자동차의 연구원 분들에게도 감사의 인사를 드립니다. 홍승현 연구위원님, 권순우, 강민우, 김현기, 이충안 책임연구원님 감사드립니다.

정영웅 교수님, 봉혁종 박사님 두 분의 영향으로 Python을 배우고 사용할 수 있었습니다. 두 분의 도움에 감사드립니다.